REPORT DOCUMENTATION PAGE

Form Approved
OMB No. 0704-0188

AD-A250 566

2. REPORT DATE	3. REPORT TYPE AND DATES COVERED
April, 1992	Final 1/15/87-1/15/92

(U) Soot Particle Inception and Growth Processes in Combustion

5. FUNDING NUMBERS

PE - 61102F
PR - 2308
SA - BS
AFOSR - 87 - 0145

6. AUTHOR(S)

Robert J. Santoro

7. PERFORMING ORGANIZATION NAME(S) AND ADDRESS(ES)

The Pennsylvania State University
240 Research Building E, Bigler Road
University Park, PA 16802

8. PERFORMING ORGANIZATION REPORT NUMBER

AFOSR-TR- 92 0396

9. SPONSORING/MONITORING AGENCY NAME(S) AND ADDRESS(ES)

AFOSR/NA
Building 410
Bolling AFB DC 20332-6448

10. SPONSORING/MONITORING AGENCY REPORT NUMBER

11. SUPPLEMENTARY NOTES

12a. DISTRIBUTION/AVAILABILITY STATEMENT

Approved for public release; distribution is unlimited

12b. DISTRIBUTION CODE

13. ABSTRACT (Maximum 200 words)

A study of soot particle inception and growth has been completed which considered fuel molecular structure, fuel concentration, temperature and operating pressure effects. These studies indicated that fuel species most strongly affected the particle inception process, as opposed to the surface growth process, and support an interpretation that inception controls the maximum amount of soot formed. Studies of concentration and temperature variations indicated that temperature effects dominate. The analysis yielded an apparent activation energy of 94.5 kcal/mole for the temperature dependence, while the fuel concentration dependence, represented as $[X_o]^n$, was given by n = 0.3. Studies of soot aggregates found in these flames yielded higher values of volume-mean diameter, a larger surface area per unit volume, and lower values of the aggregate number concentration as compared to spherical particle assumptions. Operating pressure studies indicated that a power law representation of the form P^n, represented soot volume fraction dependence on the pressure, P, and confirmed the strong sensitivity of soot formation to pressure. Finally, high pressure diffusion flame studies revealed the onset of buoyant instabilities induced by changes in the pressure. A joint series of experiments and computations provided strong evidence to support that these studies isolate Richardson number as the only variable parameter.

14. SUBJECT TERMS

Soot Formation, Soot Particles, Diffusion Flames

15. NUMBER OF PAGES
132

16. PRICE CODE

17. SECURITY CLASSIFICATION OF REPORT	18. SECURITY CLASSIFICATION OF THIS PAGE	19. SECURITY CLASSIFICATION OF ABSTRACT	20. LIMITATION OF ABSTRACT
Unclassified	Unclassified	Unclassified	UL

Final Report

on

Soot Particle Inception and Growth Processes in Combustion

(AFOSR Grant AFOSR-87-0145)

Prepared by:

Robert J. Santoro
Department of Mechanical Engineering
The Pennsylvania State University
University Park, PA 16802

Submitted to:

Air Force Office of Scientific Research
Bolling Air Force Base
Washington, DC

April 1992

Table of Contents

Table of Contents (cont'd.)

SUMMARY

A fundamental study of soot particle inception and growth processes has been completed which specifically considered the effects of fuel molecular structure, fuel concentration, temperature and operating pressure on the formation of soot particles. Coannular laminar diffusion flames burning in air were studied for pure fuels (methane and ethene) as well as fuel mixtures involving ethene propene, butane, 1-butene and 1,3 butadiene individually mixed with methane or ethene. The fuel structure studies indicated that the fuel species most strongly affected the particle inception process for the fuels studied, as opposed to the surface growth process. Surface growth rate constants, when normalized by the available surface area, were typically within a factor of two for the fuels studied. These findings support an interpretation in which inception controls the maximum amount of soot formed in the flame. Studies in which fuel concentration and flame temperature were varied through dilution of fuel with an inert species indicated that temperature effects dominate changes due to variations in the concentration under most conditions. Local temperature and concentration measurements were shown to be absolutely necessary to properly interpret the effects of inert dilution. The analysis yielded an apparent activation energy of 94.5 kcal/mole for the temperature dependence. The fuel concentration dependence, represented as $[X_o]^n$, where X_o is the fuel concentration at the exit of the fuel tube, was best represented by $n = 0.3$. Studies of the evolution of the soot particles in laminar diffusion flames indicated that clusters or aggregates are found in the higher parts of the flame. These clusters, which are composed of nearly spherical primary particles, possess different optical properties from their spherical equivalents. As compared to the Rayleigh data reduction for spherical particles, the aggregate analysis yielded higher values of volume-mean diameter, a larger surface area per unit volume, and lower values of the aggregate number concentration. The present results indicate that a self-consistent interpretation of the light scattering properties of the soot aerosol is afforded by recognizing its aggregate structure. Operating pressure effects on soot formation were also studied and indicated that a power law representation of the form of P^n, where P is the operating pressure, accurately represented the behavior of the soot volume fraction as the pressure was varied. For studies involving the alkene species, ethene and propene, the value of n was found to be close to first order (1.05 ± 0.06 and 1.16 ± 0.01, respectively). Studies of an alkane fuel, ethane, resulted in a significantly larger value for the power dependence closer to second order in n (1.62 - 1.88, depending on the flow rate). These results confirm the strong dependence of soot formation on the operating pressure and furthermore point to potential fuel structure effects. Finally, studies of these high pressure diffusion flames have resulted in the observation of the onset of buoyant instabilities induced by changes in the pressure. A simple procedure has been described for isolating these buoyancy effects in jet diffusion flame experiments. All that is necessary is that background pressure be varied while maintaining constant mass flows of fuel and oxidizer into the burner. A theoretical model for these flames indicates that this procedure isolates Richardson number (or relative buoyancy force) as the only variable parameter, which is equivalent to varying the gravitational acceleration. A joint series of experiments and computations involving a pressurized low speed methane/air diffusion flame has provided strong evidence to support the theory.

1.0 RESEARCH OBJECTIVES

The primary objective of this research program was to provide additional fundamental understanding of the processes which control soot formation under conditions applicable to future gas turbine engine operation. The emphasis of the studies was to examine the physical and chemical mechanisms which control soot particle inception and surface growth. The inception region is of particular interest because it has been argued to control the amount of soot formed during the combustion process. In the present studies, detailed measurements of both the inception and surface growth phases were undertaken to provide the necessary basis for evaluating the relative importance of these fundamental mechanisms on the formation of soot particles.

One particular challenge for the present studies was to acquire data over a wide range of flame conditions. In this respect, fuel species, concentration, temperature and operating pressures were selected as parameters for study. The results and conclusions regarding the effects of each of these parameters will be presented in the following sections. These parameters were selected because they are viewed as being critical to controlling soot formation in future gas turbine engines which will burn broader specification fuels at higher pressures than currently employed in such engines. Through the understanding gained in these studies, improved prediction capabilities are resulting which will impact the design methodology for future gas turbine combustors.

2.0 RESEARCH APPROACH

The basic nature of the objective of the present research program required that fundamental studies be conducted under well controlled conditions. Additionally, a capability to provide extensive measurements of the soot particle, velocity, temperature and gas concentration fields was also desirable. For these reasons, the studies were conducted in a laminar diffusion flame environment burning in air to which a variety of diagnostic techniques were applied.

Fuel mixture studies employing a fuel addition approach have proven useful for the study of fuel molecular structure and pressure effects. In these studies, well characterized methane and ethene baseline diffusion flames have been used. To these baseline flames, controlled amounts of an additional fuel species are added under conditions in which the total carbon atom flow rate is held constant. In this manner, the effects of a particular fuel molecular structure can be investigated under similar flame conditions. These studies were carried out in a coannular diffusion flame configuration under both atmospheric and elevated pressure conditions. A high pressure diffusion flame facility capable of operating at pressures up to twenty atmospheres was assembled for these high pressure studies, and investigations have been conducted for a pressure range of one to ten atmospheres.

Laser-based diagnostics have been emphasized for the soot particle and velocity field measurements in these studies. An extensive laser light scattering/extinction apparatus was utilized for the soot particle measurements. This apparatus has the capability to provide information on the volume fraction, particle diameter and number concentration of soot particles present in the flame. Using light extinction and scattering measurements, additional extensive scattering measurements obtained as a function of scattering angle and laser polarization provided a redundant measurement capability to the extinction/scattering ratio technique. These capabilities were useful in studies attempting to account for the aggregate nature of the mature soot particles. Velocity measurements using a laser velocimetry technique were obtained to determine the particle paths and temporal history of the soot formation process. From the combined laser velocimetry and light scattering measurements, information on soot particle inception, surface growth and oxidation were obtained.

These particle and velocity measurements were complemented by thermocouple measurements for temperature. Additionally, a quadrapole mass spectrometer, wavelength selective optical absorption system and laser-induced fluorescence apparatus have been employed to provide information on gas phase species present in these flames. A related activity involved the development of a sonic quartz microprobe for sampling in particle laden flows. This technique provides new capabilities needed to

measure gas phase species in both the precursor and surface growth regions. In the particle diagnostic area, scanning and transmission electron microscopy have been developed to allow complementary measurements of primary particle size in soot aggregates. Thus, an approach, involving carefully controlled experiments to which extensive diagnostic measurement techniques were applied, was used to investigate basic mechanisms important in soot formation. Through this process, effects controlling the production and destruction of soot particles in combustion systems could be examined in a quantitative manner.

3.0 RESEARCH ACCOMPLISHMENTS

3.1 Introduction

In the following sections, the accomplishments and results obtained during the current research program are reviewed. These include results of the effects of fuel molecular structure, concentration and temperature variations, soot aggregate processes and operating pressure. An additional section dealing with buoyancy effects in jet diffusion flames, which arose out of the high pressure studies, will also be reviewed. For those results for which journal articles have been prepared, a summary of the results will be presented with the complete article included as an appendix. For the readers' convenience, a section describing the diagnostics employed in these studies will be presented first. This section will serve to provide the details of the individual diagnostic approaches for those interested while allowing others to proceed directly to the results of interest.

3.2 Experimental Apparatus and Techniques

3.2.1. Burner and Flow Apparatus

Two diffusion flame facilities were used in the present studies. The first involves an atmospheric pressure diffusion flame facility and the second is a high pressure diffusion flame apparatus.

3.2.1.1. Atmospheric Diffusion Flame Facility

The atmospheric diffusion flame facility consists of coannular diffusion flame burner, burner chimney, positioning system and gas metering system. The burner has a coannular configuration consisting of a 1.1 cm fuel tube surrounded by a 10 cm air annulus. The air passage is partially filled with glass beads followed by a series of fine screens to provide flow conditioning. A ceramic honeycomb 2.54 cm in thickness is used at the exit to provide a uniform flow field. The fuel tube which extends 4.8 mm above the ceramic honeycomb also is partly filled with glass beads to condition the flow. The fuel flow can consist of up to three gases, each metered with a separate rotameter. This allows for mixtures of fuels as well a nitrogen dilution of the fuel for temperature and concentration variations. These rotameters have been calibrated for various gases using a soap bubble meter technique. The air flow is metered using a mass flowmeter which can monitor flows up to 5 SCFM of air. To protect the flame from room disturbances, a metal chimney has been incorporated into the burner facility. The chimney translates horizontally with the burner while sliding vertically within the chimney. Slots machined in the chimney provide for optical access.

The burner is mounted on a pair of motorized translating stages which provide for vertical and horizontal motion. A manual translation stage is also included to allow for adjustment in the second horizontal direction and is used to align the burner with the laser scattering system. The motorized stages are used to traverse the burner through the laser beam to obtain measurements over the cross section of the flame at a particular height in the flame. The motorized translation stages have a position resolution of 0.0127 mm which is sufficient for the present experiments. Both motorized stages are interfaced to and controlled by an IBM-XT computer using the general purpose interface bus (GPIB-IEEE 488). The software to control the translation stages is incorporated into the data acquisition program for the laser scattering measurements.

3.2.1.2. High Pressure Diffusion Flame Facility

In order to provide for studies at elevated pressure, a high pressure diffusion flame facility was constructed. This facility is composed of a coannular burner, pressure vessel, positioning system and gas metering apparatus. The design chosen provides for a significant degree of similarity between the atmospheric and high pressure diffusion flame burners. A burner identical to that previously described above was constructed. This burner is mounted inside a high pressure vessel capable of withstanding the required operating pressures. The high pressure diffusion flame burner is shown in figure 1.

Because of the mass of the pressure vessel, the approach chosen for the atmospheric system of vertically translating the entire burner and pressure vessel is not feasible. Rather, the burner is mounted on a motorized translation stage located internal to the pressure vessel. Electrical connections are made through the base of the pressure vessel allowing external control of the vertical position of the burner. To provide horizontal movement, the base of the pressure vessel is attached to a precision ball bearing stage which requires only a few pounds of force to move horizontally with weights as large as 1500 pounds attached. Thus, a relatively small motorized translation stage can be used to provide horizontal movement. As with the atmospheric burner, these motorized stages are capable of computer control using the laboratory IBM-XT personal computer. The only disadvantage with its approach is that sufficient space must be provided within the pressure vessel to house the vertical motion assembly and the flexible gas supply lines for the burner.

To accommodate this limitation, the pressure vessel has been constructed as two separate sections. The lower section is constructed of 8 inch diameter carbon steel seamless pipe which is 24 inches in length. The vertical translating mechanism is mounted to the base of this lower section. In addition to the electrical connection for the motorized translation stage, provisions for connection of fuel and air lines are also made through this base. Internal connections to the diffusion flame burner

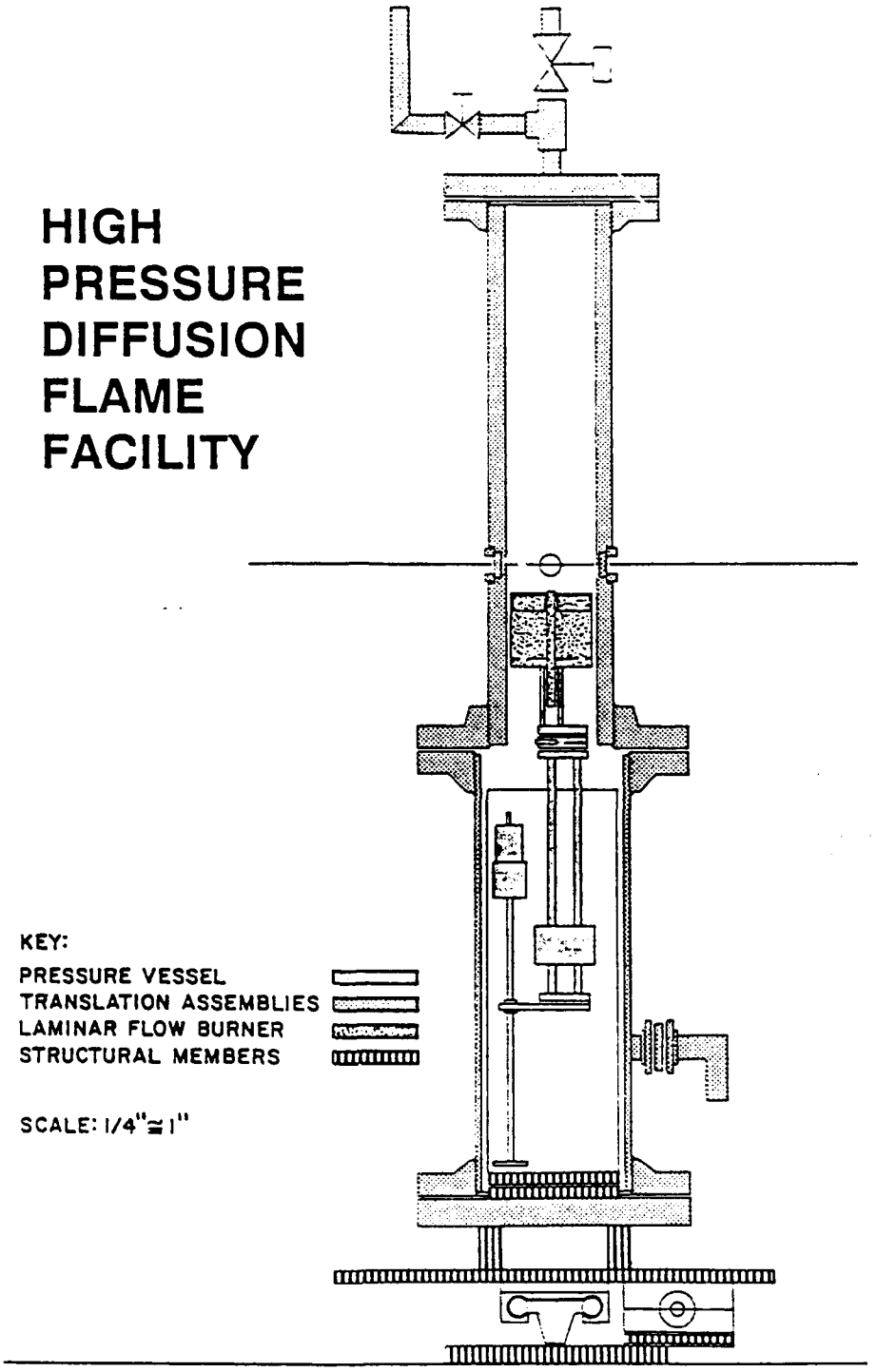

Figure 1. High pressure diffusion flame apparatus

can be made with low pressure tygon tubing since no pressure difference exists across the tubing wall inside the pressure vessel.

The upper section of the pressure vessel, which provides for optical access to the flame region, is 30 inches in length and constructed from 6 inch diameter carbon steel pipe. This section includes four windows which are two inches in diameter and 1/2 inch thick. These windows allow sufficient optical access for both the laser light scattering and the laser velocimetry measurements. The operating pressure in the burner is adjusted using manual valves located in the exhaust line of the burner. Connection to this exhaust system is made through a second flange to which a 2 inch diameter exhaust line has been connected. At this time, no cooling is required for the burner or exhaust section. Temperature measurements indicated that for conditions typical for the present experiments, the burner does not heat up significantly.

Control and measurement of the fuel and air flow rates are accomplished using mass flow meters and controllers. These meters are insensitive to the operating pressure and thus can be calibrated at atmospheric pressure while providing accurate metering at elevated pressure. The fuel metering system allows up to three gases to be mixed using the independent mass flow controllers. These controllers maintain a constant mass flow independent of the pressure drop across the meter. This assures a constant mass flow rate of fuel as well as a convenient start-up capability. Otherwise, the fuel flow rate would decrease as the operating pressure was increased, requiring continual readjustment. Because of the relatively large air flow rate required, a mass controller approach is not feasible for the air flow metering. The air flow rate is monitored by a mass flowmeter which requires adjustment as the operating pressure is varied. This present burner has been designed to operate at pressures as high as twenty atmospheres. Stable flames at pressures up to ten atmospheres have been studied to date.

3.2.2. Non-Intrusive Optical Diagnostics

A more complete understanding of soot formation and destruction processes requires the measurement of the key properties characterizing the combusting flow. These property measurements include soot particle size and concentration, temperature, gas phase species concentration and velocity. Once determined, this set of measurements provides the basis from which to develop an understanding of the temporal evolution of soot particle formation in combustion environments. To address some of these needs, non-intrusive optical techniques have been employed. Laser light scattering has been used to characterize the soot particle field while laser velocimetry has been utilized for velocity measurements. An optical absorption apparatus has been assembled to allow wavelength selective absorption measurements to be obtained. These techniques were complemented by intrusive probe sampling techniques to be described in a later section.

3.2.2.1. Laser Light Scattering Apparatus

The laser light scattering apparatus, utilizing a 4W argon ion laser as the light source, provided for particle extinction and scattering measurements. Scattering measurements were made primarily at 90° although the system can be used to obtain measurements at 45° and 135° (see figure 2). The laser source was modulated using a mechanical chopper operating at 1 kHz to allow for synchronous detection of the transmitted and scattered light signals. A polarization rotator was also incorporated in the system to allow adjustment of the polarization of the incident light beam. The laser beam was focused in the burner using a 30 cm focal length lens which results in a probe beam diameter of 0.02 cm. Typically the laser was operated at the 514.5 nm laser line with an output power of about 0.5W.

The transmitted light signal was detected using a silicon photodiode. The laser light intensity was reduced by a neutral density filter (N.D. 2.0) to a level suitable for linear photodiode response. The scattered light was detected using a photomultiplier detector (PMT). The PMT had a narrowband filter center at 514.5 nm with a 1 nm bandwidth incorporated in the PMT housing to help reject light other than that generated from the particle scattering event. A pinhole with a diameter of 1 mm,

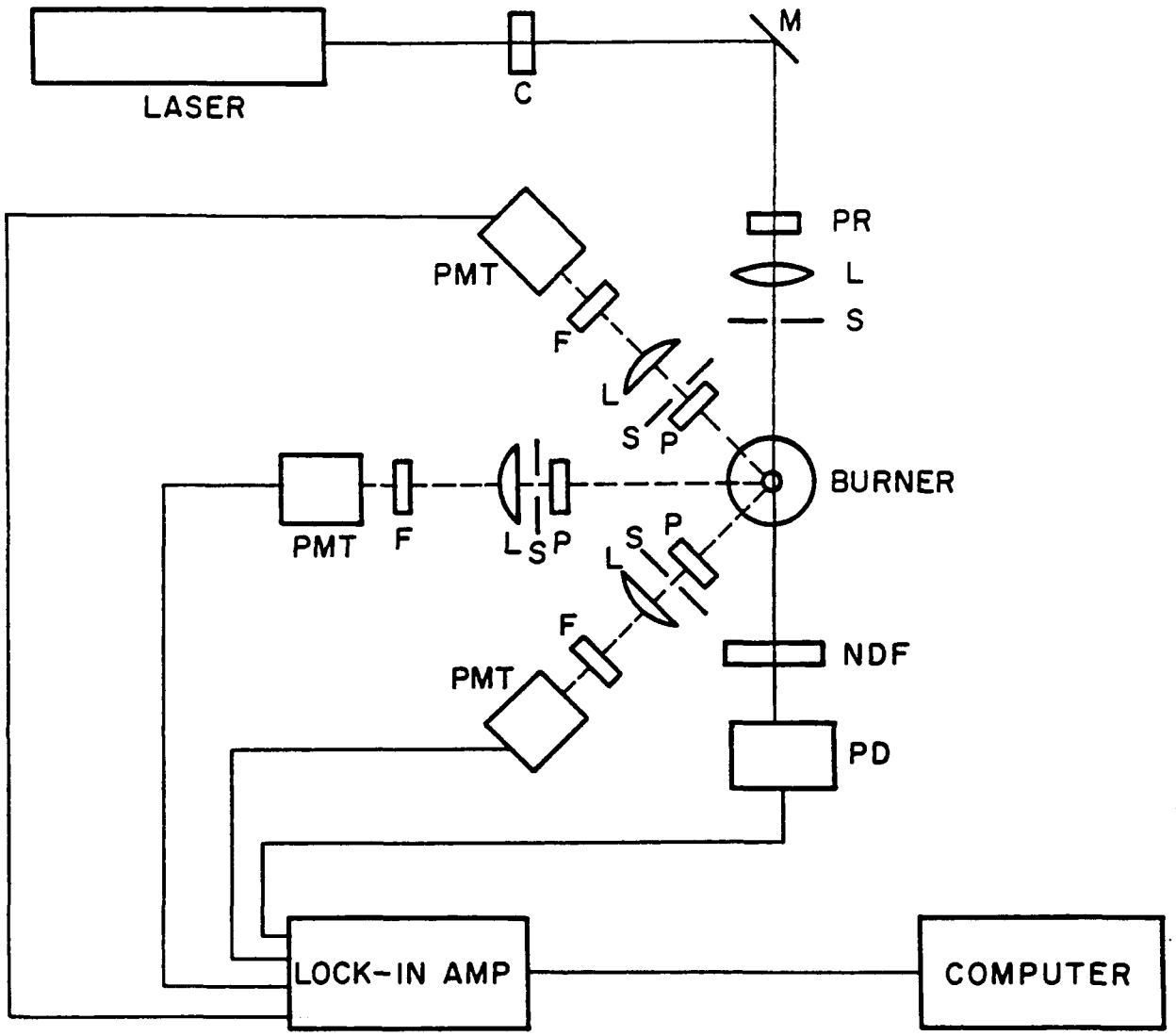

Figure 2. Schematic of laser scattering/extinction system: C = chopper, M = mirror, PR = polarization rotator, L = lens, S = spatial filter (circular aperture), NDF = neutral density filter, PD = photodiode, P = polarization, F = narrowband filter, PMT = photomultiplier

located in front on this filter, limited the measurement volume length along the beam to 0.1 cm. The 15 cm focal length collection lens used to focus the scattered light onto the PMT was arranged to provide unity magnification. Thus, the collection volume was a cylinder approximately 0.02 cm in diameter and .1 cm in length resulting in a volume of 3.1×10^{-3} cm^3. The collection lens was preceded by a polarization filter to allow polarization discrimination for the scattered light detected. The collection solid angle was determined by a 1.27 cm aperture which is located between the polarization filter and the collection lens. This aperture limited the collection angle to approximately 2°.

The output from each of the detectors was input into separate lock-in amplifiers which were interfaced to the IBM-XT computer over the GPIB bus. These units are capable of full computer control which allows for autoranging of the lock-in amplifiers. Computer software to control the lock-in amplifiers has been integrated with the stepper motor control programs to provide a complete data acquisition routine. These procedures provide a high degree of user independent data acquisition.

Data taken from the lock-in amplifiers was stored on the IBM-XT internal disk. The light scattering measurements required extensive data reduction to yield particle size information. Such calculations were performed on computers more capable than the laboratory computer used for the data acquisition. Thus, the IBM-XT was linked over the Mechanical Engineering Department's network to the University's VAX computer facilities. This allowed for rapid data analysis and graphical output. The necessary data reduction and plotting software have been developed for this facility.

The scattered light detection system was calibrated to account for effects of the incident laser power, sample volume, light collection efficiency, photomultiplier sensitivity and electronic gain of the system. The calibration was accomplished by passing ethene, a gas with a known Rayleigh scattering cross section, through the fuel passage of the burner and measuring the resulting scattered

light. This procedure allowed for an absolute determination of the differential scattering cross section per unit volume, $Q(\theta)$, which is the power scattered in the direction θ per unit incident flux.

Several approaches can be taken to determine the particle size from the above defined cross sections. Three are of interest with respect to the instrumental set up discussed previously. These are the ratio of scattering to extinction, Q_{vv} (90°)/K_{ext}, the ratios of the scattering signal at two angles (dissymmetry ratio) $Q_{vv}(45°)/Q_{vv}(90°)$ and $Q_{vv}(45°)/Q_{vv}(135°)$, and the polarization ratio, $Q_{hh}(90°)/Q_{vv}(90°)$; the scattering measurement angle is specified for each quantity. Each of these ratios has a strong dependence on particle size and represents a redundant set of data in terms of the particle properties for particles in the Mie size region ($D > \lambda$). For particles in the Rayleigh size region ($D << \lambda$), scattering is isotropic so the dissymmetry ratio has a value of unity and the defined polarization ration approaches zero. Thus, in this small particle limit, only the scattering/extinction ratio yields size information. However, for soot formation processes, the rapid coagulation and surface growth processes lead quickly to particle sizes characteristic of the Mie size region. Because of its applicability throughout the Rayleigh and Mie size regimes, scattering/extinction measurements have proved most useful in prior studies in this laboratory. Recently, efforts involving dissymmetry and polarization ratio have been undertaken to consider the effects of particle agglomeration on light scattering measurement [1].

The laser light scattering apparatus described above provides a versatile instrument for characterizing the volume fraction, particle size and number concentration of soot particles formed in flames. Thus, processes starting from particle inception through surface growth and eventually oxidation can be measured. Application of these techniques in the present studies has allowed an extensive examination of soot formation in diffusion flames [2-8].

3.2.2.2 Laser Velocimetry Apparatus

Laser velocimetry (LV) has been used to measure the velocity field to investigate the transport processes in the laminar diffusion flame. The laser velocimeter is a conventional dual beam system utilizing an argon ion laser operated at the 514.5 nm laser line to provide the incident laser beam. This laser beam is then split into two parallel beams of equal intensity which are separated by a 50 mm spacing. These beams are then focused to form the LV probe volume using a lens. The resulting ellipsoidal probe volume will vary in size as a function of the focal length of the focusing lens. Typically, a lens with a 250 mm focal length is used resulting in a calculated probe diameter of 0.16 mm and a length of 1.7 mm. Scattered light is then collected with a second lens and focused onto a photomultiplier tube.

Velocity measurements are obtained from the modulation frequency of the intensity of light scattered from particles traversing the probe volume formed by the two laser beams. This scattered light can be viewed as a signature of the interference pattern resulting from the constructive and destructive interference of the laser beams. The period between the intensity maxima in the scattered light signal is thus proportional to the velocity of the particles in the probe volume. Since the signals occur randomly, digital counting techniques (burst processing) are used to obtain the frequency and thus the velocity. The digital output of the processor is stored on an IBM-XT computer.

In order to obtain measurements in situations in which the direction of the flow reverses, a Bragg cell is placed between the beam splitter and the focusing lens. This cell imparts a frequency offset to one of the two beams used in forming the LV probe volume. This frequency shift allows determination of the direction as well as the magnitude of the velocity component by providing a frequency offset for zero velocity. The introduction of this frequency offset is also useful for measurements in low velocity flows.

Measurements of the axial and radial components of the velocity field have been used previously to construct the streak lines which soot particles follow in the laminar diffusion flame studies [3].

This information has been critical in gaining information on the temporal evolution of the soot particle field.

3.2.2.3 Optical Absorption System

An optical absorption apparatus was assembled to provide for wavelength selective measurements of absorbing species in the flame studies. This system consisted of a tungsten filament lamp driven with a highly stable D.C. power supply. The light emitted from the lamp was focused on the axis of the burner and then passed into a spectrometer for detection. Both photomultiplier and photodiode detectors were used for signal detection with the choice of detector subject to the wavelength range of interest. The spatial resolution of measurements was adjusted by the use of suitable apertures placed before and after the flame.

In order to provide for rejection of background radiation and noise, the incident light was modulated with a mechanical chopper. Signals were then measured using a lock-in detection technique. For cases where extremely small signals are encountered, a differential reference channel technique was assembled as well. In this approach, a portion of the incident light was directed around the flame region. This beam was modulated using a separated mechanical chopper operating at a different frequency from that used for the beam passing through the flame. This beam was then recombined with the main beam and input into the spectrometer. Two lock-in amplifiers, each operating at the separate frequencies of the mechanical choppers, were used to measure the absorption signal as well as the incident light signal. This approach eliminates signal variations resulting from changes in the lamp source and provided sensitivity of three parts in a thousand. Wavelength dependent measurements of the absorption process were then obtained by scanning the spectrometer over a desired wavelength region and recording the resulting signal. Data acquisition and control of the spectrometer were provided by an IBM XT laboratory computer.

Analysis of the measurements was intended to provide information on both gas phase and soot particle concentration. The measurement of gas phase species can be based on the observation that,

as molecular weight increases, absorption shifts to long wavelengths. Thus, by a systematic evaluation of the wavelength dependence of the absorption signals as a function of location in the flame, the evolution of large molecular weight species can be followed.

3.2.3 Intrusive Probe Sampling for Species Concentration Measurements

3.2.3.1 Quadrapole Mass Spectrometer and Conventional Quartz Microprobe

In order to provide more quantitative information on the species concentration, a mass spectrometer system was assembled for these studies. This facility was obtained under support through a DoD University Research Instrumentation Award by AFOSR.

Gas samples from the flames under study were sampled using a conventional quartz microprobe technique similar to the approach taken by Smyth *et al.* [9]. The mass spectrometer selected for these studies utilizes a quadrapole mass filter with a mass range of 1 to 500 amu. This unit (an Extrel Model C-50) has excellent mass resolution (0.1 amu) and high sensitivity. The probe and mass spectrometer assembly were differentially pumped. A pressure of between 1 and 10 torrs using a vacuum roughing pump was achieved directly behind the quartz orifice which is nominally 100 μm in diameter. Sampling from this low pressure region was provided by a second probe of identical construction. This second probe was used to introduce gases into the mass spectrometer which was maintained at a pressure near 10^{-6} torr using a turbomolecular pumping system.

Radial profiles of the species concentration as a function of axial position were obtained by transversing the flame in the radial direction. Similar to the optical diagnostic approaches, data acquisition and the control of the mass spectrometer have been implemented using a laboratory personnel computer system. This capability allowed for rapid and convenient data acquisition, while also affording opportunities for other probing approaches, such as rapid insertion sampling. For situations where more species specific information is required, gas chromatography techniques were also available within the laboratory. These techniques, which were of limited use in terms of the

flame sampling, do provide capabilities useful in unambiguously identifying the specific nature of an observed mass peak, as well as for comparing calibration of particular species.

This system was used extensively to obtain concentration information in diluted methane flames. These results will be described below in detail. Because the quartz microprobe could not be employed in particle laden regions of the flame due to probe clogging, a separate sonic probe for sampling in these regions was developed and is described next.

3.2.3.2 Electromechanical Sonic Probe

As mentioned above, the need to determine gas species concentrations in regions containing soot particles presents serious diagnostic challenges. In general, optical diagnostic techniques can measure only a limited number of species and in some cases can not be reliably applied in the presence of soot particles. Sampling probe techniques usually are limited by orifice clogging problems which can only be overcome by increasing the orifice dimensions at the sacrifice of spatial resolution of the measurements. To overcome the aforementioned orifice clogging problem, a novel sonic sampling probe has been developed and applied to a series of laminar diffusion flames containing various amounts of soot. A patent disclosure for this probe was submitted; and subsequently, patent rights have been transferred to the U.S. government. The details of the design and operation of this probe were presented at the Eastern Section Meeting of The Combustion Institute [10]. A summary of the operation of the sonic probe along with the results of a set of comparisons obtained to validate its operation is given below.

The approach employed to prevent clogging of the probe orifice involves mechanically oscillating a wire through the orifice region using a spring loaded solenoid plunger whose driving circuit is electronically interrupted periodically (see figure 3). The constant motion of the wire relative to the quartz tube is responsible for keeping the orifice open. For the present probe, the effective orifice is the annulus formed by an oscillating 380 μm diameter Nichrome wire of uniform cross section and the 400 μm diameter orifice in the quartz tube. Therefore, the effective orifice is equivalent to a 125

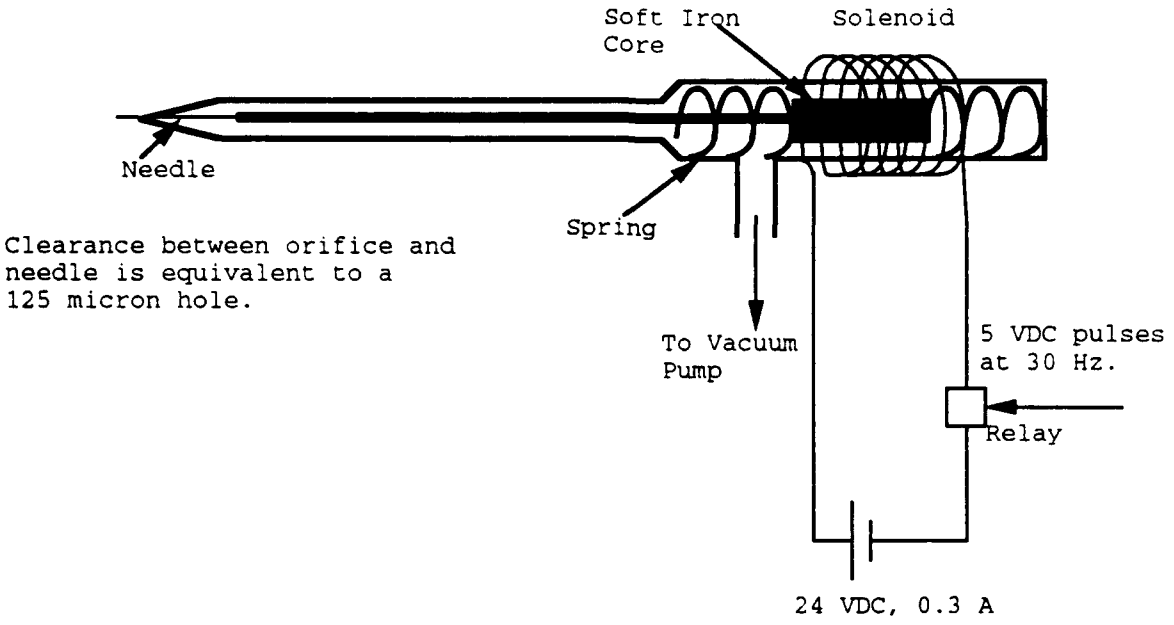

Figure 3. Schematic of Electromechanical Sonic Probe.

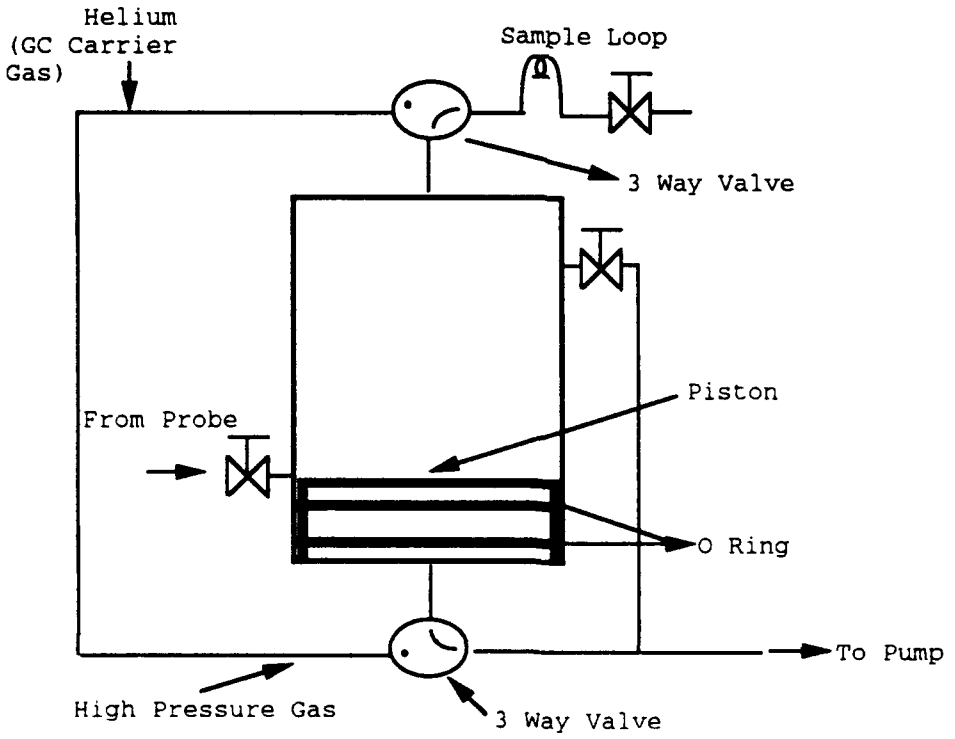

Figure 4. Schematic Of Sample Collection Apparatus.

μm circular hole. The wire is soldered into a 1.59 mm (1/16 inch) tube which is attached to a spring loaded soft iron solenoid plunger. The solenoid is activated with a 24 volt power supply providing 0.3 amperes current. The solenoid circuit is interrupted with the aid of a mini relay which is activated by a regular series of 5 volt pulses from a function generator. When the solenoid circuit is complete, the solenoid retracts the soft iron plunger and consequently the wire is partially withdrawn. A small portion of the wire still extends beyond the orifice because a constant effective orifice size is desired. The inward motion of the plunger compresses the spring behind the plunger. When the mini relay interrupts the solenoid circuit, the compressed spring expands and returns the plunger and the wire to its original position. Thus, the wire can be made to oscillate through the orifice region at the desired frequency. For the present system, an oscillation frequency of 30 Hz has been selected.

The operation of the probe was tested by sampling from a flame burning a mixture of methane (5.6 cm^3/s) and 1-butene (1.05 cm^3/s) in air (2.75 scfm) where the local soot volume fraction was 4.0×10^{-6}. Previous studies of this flame using a probe with a 1 mm diameter orifice resulted in clogging within 15 seconds under isokinetic sampling conditions. During initial testing, the pressure downstream of the probe was monitored as an indicator of clogging problems. The pressure remained constant at 5 torr for a period of 5 minutes indicating the probe did not clog during this time period. By manually blocking the probe orifice, it was established that should the probe clog, the pressure inside the probe would fall below 1 torr. To further validate operation of the probe, species measurements with gas chromatography were carried out in the flame described above. In order to use this low pressure sampling probe in conjunction with gas chromatography, a cylinder piston device (figure 4) was designed and fabricated to compress the sample from 5 torr to 15 psi. The measurements from this probe were compared with results obtained from a water cooled stainless steel probe having a 2 mm orifice (which clogs within 5 minutes under isokinetic sampling conditions). Good agreement ($\approx 10\%$) is observed between the two probes for measurements obtained along the centerline from the upper regions of this flame. Figure 5 presents this comparison in a plot of CO

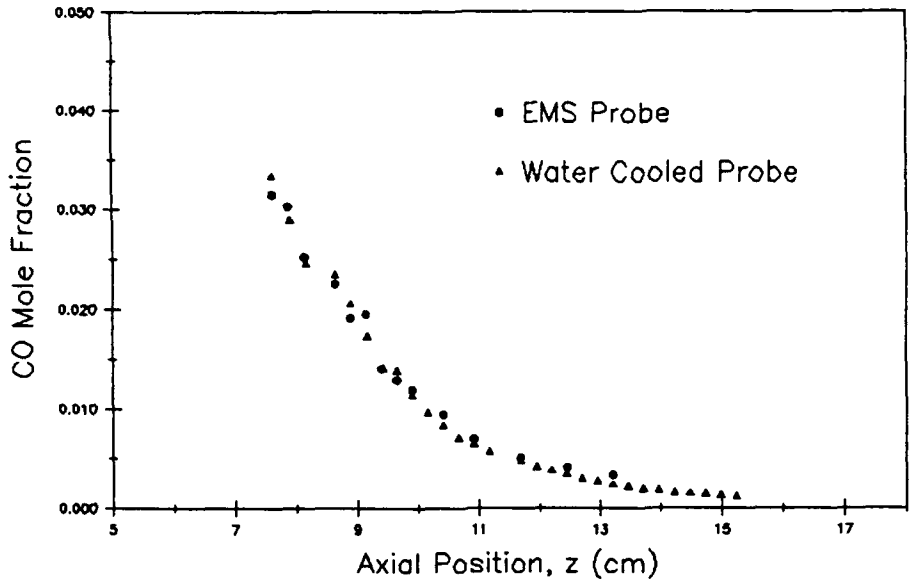

Figure 5. Comparison of CO measurements from the Electromechanical Sonic Probe with similar measurements from a water cooled stainless steel probe.

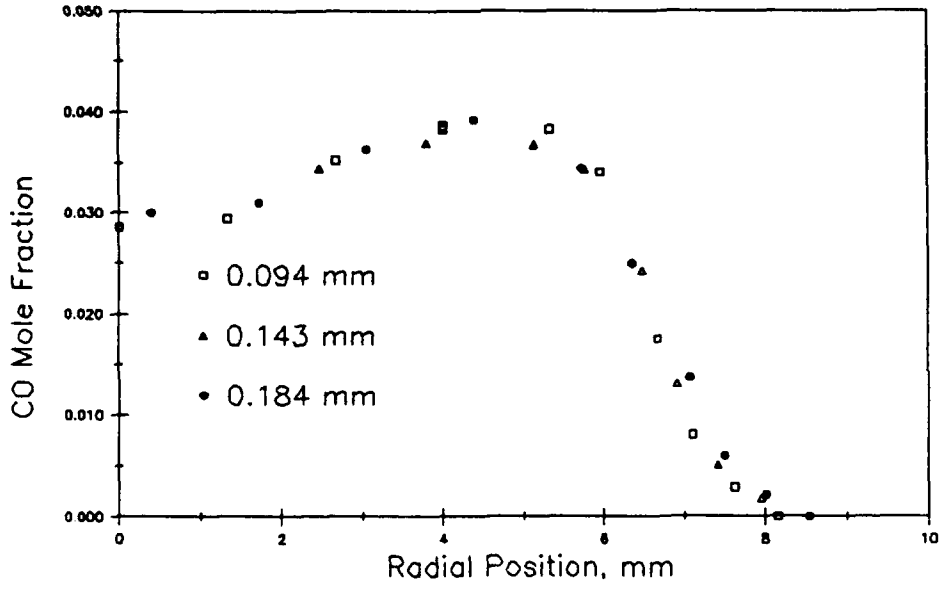

Figure 6. Radial profiles of CO mole fraction from probes with three different orifice sizes demonstrate gradient broadening. The symbols identified on the plot refer to the orifice diameters.

mole fraction versus axial position in the flame. Other species also compare as well (data not shown). This probe was also compared with a conventional sonic probe (orifice 85 μm) in a relatively soot free methane flame and again the measurements compared well for the upper regions of the flame. However, some differences have been observed in the lower parts of the flame where steep concentration gradients are present.

In order to more closely examine these differences, a pure methane flame (CH_4: 5.7 cc/s, Air: 795 cc/s), that was previously studied by Mitchell [11], was selected . Radial particle measurements of the CO mole fraction at a height of 12 mm were made with three different probes - two conventional sonic probes and the electromechanical sonic probe (EMS). The probe orifice sizes were estimated by measuring the flow rate of room air through the probes under choked flow conditions. The EMS probe has the largest orifice with an equivalent circular diameter of 0.184 mm. The differences between various probe measurements that were observed in the lower part of the flame are related to the positioning uncertainty of the probe and differences in the spatial resolutions of each probe. In the lower region of diffusion flames, the species concentration gradients are steep on the air side of the flame front. Therefore, in this region uncertainties in probe positioning and differences in spatial resolutions have to be kept in mind when making comparisons. The effect of the finite probe orifice diameter results in "broadening" or decreasing the steepness of the species gradient and will be referred to as "gradient broadening".

Figure 6 compares the radial measurements of CO mole fraction with the three different probes. Since complete radial profiles across the entire flame were not obtained, some uncertainty in the location of the centerline of the flame exists. In order to examine the probe orifice effects on gradient broadening, the data in figure 6 are shifted slightly to provide an overlap of the region of steepest gradient for each data set. For the region between the centerline and the peak CO mole fraction location, there is no significant difference between the measurements from the three probes. On the air side of the peak CO mole fraction, the probe with the smaller orifice gave CO values displaying

steeper radial gradients. This is understandable since a smaller orifice results in better spatial resolution and less gradient broadening.

For the present EMS probe, a nichrome wire is used to keep the orifice of the probe open. Attempts at using a quartz fiber have not been successful, since this fiber becomes brittle once it is exposed to the flame and breaks easily. Since the measurements from the probe with the nichrome wire compare well with measurements using the other probes, this probe has been used to obtain radial profiles of gas phase species in the sooty regions of the flames currently under study. Some concerns remain about potential catalytic effects due to the nichrome wire and must be considered as the EMS probe is used in other environments.

Table 1 indicates the fuel and air flow rates for the profiles studied with the various probes, while figures 7 and 8 show typical radial profile measurements of N_2, CO_2, O_2 and CO in these flames. The symbols represent actual measurements and the lines through the symbols are extended across the flame centerline by symmetry. Fuel species measurements and moisture estimates are not plotted.

Table 1: Fuel and air flow rates (cm^3/s) for the overventilated flame studies

FLAME	CH_4	C_4H_{10}	C_4H_8	AIR
Pure Methane	9.8	--	--	1298
Methane/Butane	5.6	1.05	--	1298
Methane/1-Butene	5.6	--	1.05	1298
Mitchell	5.7	--	--	795

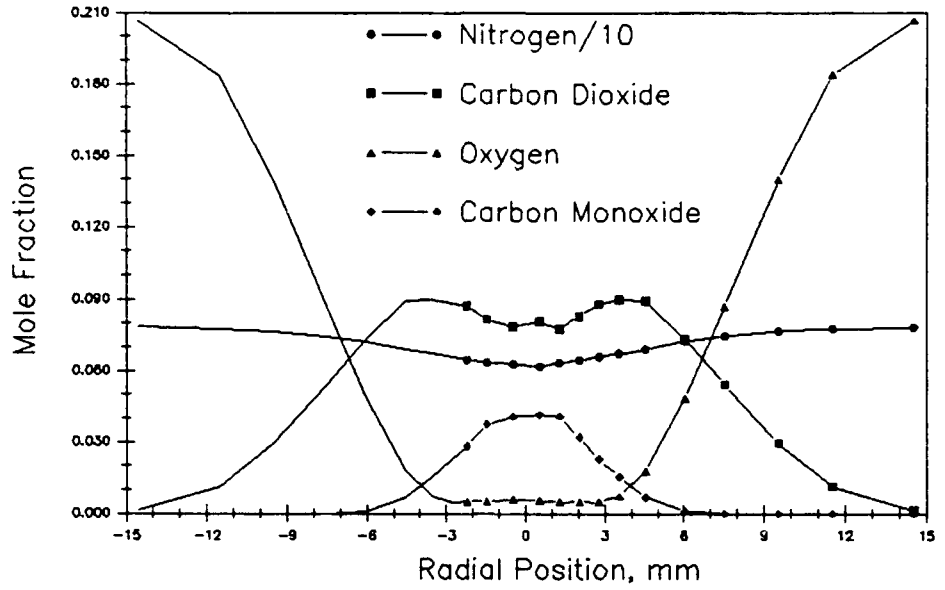

Figure 7. Radial profiles of N_2, CO_2, O_2 and CO in the pure methane flame at a height of 7.874 cm.

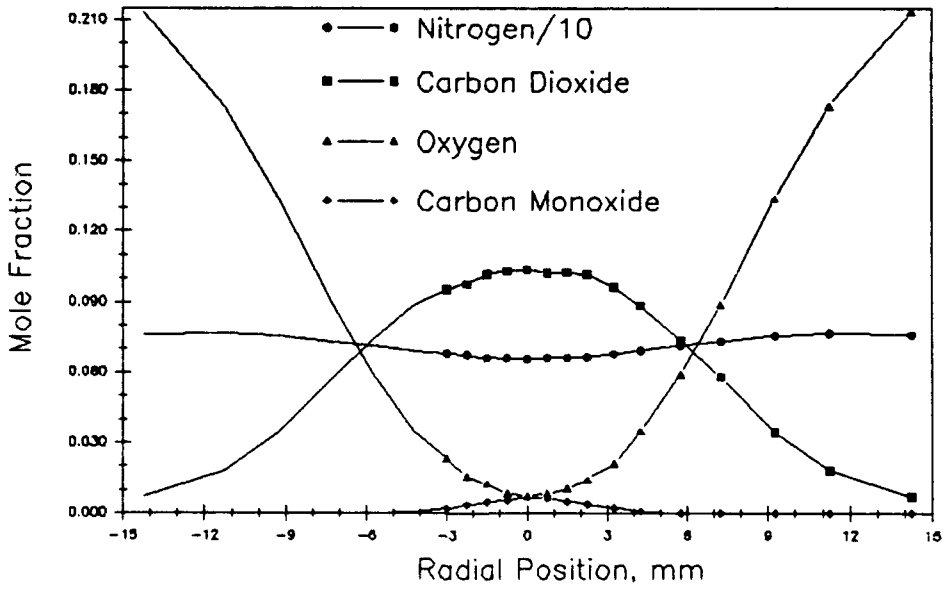

Figure 8. Radial profiles of N_2, CO_2, O_2 and CO in the pure methane flame at a height of 9.906 cm.

3.2.4 Diagnostics for Temperature Measurements

Besides the particle, velocity and species concentration measurements, temperature measurements were required to complete the data base needed to analyze the soot formation and destruction processes. For these measurements, an intrusive measurement approach using fine wire thermocouples was utilized.

Temperature profiles were obtained using Pt/Pt - 10% Rh fine wire thermocouples. A rapid insertion technique similar to that described by Kent and Wagner [12] was employed to reduce the effects of soot particle disposition. A motorized translation stage, which is controlled by a computer, allowed rapid positioning of the thermocouple in the flame. After inserting the thermocouple and obtaining the reading, the thermocouple was retracted to a position on the lean (air) side of the flame where soot particles deposited on the thermocouple can be oxidized. By repeating the same sequence for each measurement position, a complete radial profile of the temperature field was obtained. Recent measurements have shown that this rapid insertion technique significantly reduces the effects of soot particle deposition and improves agreement with other techniques [3,12]. The difficulties of using thermocouples, particularly in sooting flames, are well documented. Nonetheless, these thermocouple measurements provided a suitable basis from which to investigate the evolution of the temperature field.

3.2.5 Particle Size Analysis

The laser light scattering and extinction apparatus provides the particle measurement capability for the present studies. Analysis of the scattering measurements is based on a MIE theory approach for spherical particles. For completeness, a brief review of the theoretical basis for this analysis is presented.

In general, the interaction of a particle and light wave is dependent on:

1. index of refraction of the particle, m
2. particle size, D

3. particle number density, N
4. particle size distribution, P(D)
5. particle shape
6. wavelength of the scattered light
7. scattering geometry

Obviously, measurement of any one of the above requires knowledge of all of the other variables. In a typical combustion environment containing soot particles, only the scattering geometry and the wavelength of the light can be specified beforehand. The remaining unknowns are determined by an appropriate combination of measurements to reduce the number of free parameters along with some reasonable assumptions. It is these assumptions which can result in inaccuracies and therefore must be considered carefully.

Combinations of scattering measurements utilizing the angular and polarization dependencies of the scattering process, or scattering and absorption measurements, have been used to determine particle number density and size [2-4]. In such an approach, the index of refraction is taken to be known, the particles are assumed to be spherical and a size distribution is assumed (e.g., log-normal).

The determination of particle size and number concentration from light scattering data depends primarily on our capability to relate the measurement of scattered and absorbed light intensity to the particle properties. Appropriate theories have been developed for spherical particles and have been widely applied for aerosol measurements. The particle properties of interest are the differential scattering cross section, $C_{ij}(\theta)$, for production of scattered light at a specified direction and total cross section for a specified particle size, C_{ext}. The subscripts i and j for the scattering cross section assume letters v or h according to whether the state of polarization of the scattered (i) and incident (j) radiation is perpendicular or parallel, respectively, to the plane of observation. For spherical particles of isotropic material, only the case of $i = j$ is of interest because cross polarization effects are absent.

The relationship between these cross sections and the experimentally measured quantities are expressed as

$$I_s = I_o N C_{ii} \left(\theta, \frac{\pi D}{\lambda}, m\right) G \tag{1}$$

and

$$\frac{I}{I_o} = \exp - \int_O^L N\, C_{ext} \left(\frac{\pi D}{\lambda}, m\right) ds \tag{2}$$

where I_s, I and I_o are the scattered, transmitted and incident intensities respectively, N is number concentration of particles, D is diameter, m is the refractive index, and G is a constant which involves factors related to the sample volume and detection instrumentation. It should be noted that the scattering cross section measurements given by equation (1) are point measurements, while the extinction cross section is an integrated quantity over the path length L. Thus, to obtain local particle extinction values, a data inversion technique must be utilized [19].

In an experiment, the quantities which are determined, once appropriate calibration factors have been introduced, are

$$Q_{ii} = N\, C_{ii} \tag{3}$$

and

$$K_{ext} = N\, C_{ext} \tag{4}$$

where Q_{ii} is the volumetric scattering cross section and K_{ext} is the extinction coefficient.

Several approaches can be taken to determine the particle size from the above defined cross sections. Three are of interest with respect to the instrumental set up discussed previously. These are the ratio of scattering to extinction, $Q_{vv}(90°))/K_{ext}$, the ratios of the scattering signal at two angles (dissymmetry ratio) $Q_{vv}(45°)/Q_{vv}(90°)$ and $Q_{vv}(45°)/Q_{vv}(135°)$, and the polarization ratio $Q_{hh}(90°)/Q_{vv}(90°)$; the scattering measurement angle is specified for each quantity. Each of these

ratios has a strong dependence on particle size and represents a redundant set of data in terms of the particle properties for particles in the Mie size region ($D > \lambda$). For particles in the Rayleigh size region ($D << \lambda$), scattering is isotropic so the dissymmetry ratio has a value of unity and the defined polarization ratio approaches zero. Thus, in this small particle limit, only the scattering/extinction ratio yields size information. However, for soot formation processes, the rapid coagulation and surface growth processes lead quickly to particles in the Mie size region.

With the particle size established, any one of the scattering cross sections can be used to find N or f_v, the soot volume fraction. The soot volume fraction, particle size and number density are related by

$$f_v = \frac{N\pi D^3}{6} \tag{5}$$

For a system in which simultaneous nucleation, particle growth and coagulation are present, a particle size distribution can be assumed to exist. In this case, the previously defined particle scattering cross sections must be averaged over the size distribution function, P(D), to yield mean values,

$$C_{ii}(\theta) = \int_0^\infty C_{ii}(\theta, \frac{\pi D}{\lambda}, m)\, P(D)\, dD \tag{6}$$

$$C_{ext}(\theta) = \int_0^\infty C_{ext}(\theta, \frac{\pi D}{\lambda}, m)\, P(D)\, dD \tag{7}$$

A widely used expression for P(D) is the logarithmic normal distribution that is given by

$$P(D) = \frac{\exp[-(\ln D/D_g)^2/2\sigma_g^2]}{\sqrt{2}\pi\sigma_g D} \tag{8}$$

where D_g and σ_g are the geometric mean diameter and geometric mean standard deviation, respectively.

3.3 Fuel Molecular Structure Effects

3.3.1 Introduction

Fuel molecular structure has long been recognized to have important effects on the production of soot particles in combustion systems [13,14]. In particular for gas turbine engines, the advent of broad specification and alternative fuels has heightened the interest in the importance of fuel structure effects [15-18]. General correlations involving the carbon-to-hydrogen (C/H) ratio have been shown to grossly represent the increasing tendency to form soot as the fuel hydrogen content decreases [18]. Sooting height measurements have also been shown to strongly depend on the fuel molecular structure [14]. However, the direct investigations of the specific processes affected by changes in the fuel structure have been much less numerous, particularly for mixing dominated conditions. The present study has focused on this aspect of the soot formation process for diffusion flame conditions.

A series of laminar diffusion flame studies was conducted to examine the effects of fuel molecular structure on the formation of soot particles. In order to maintain similar flame conditions, a fuel mixture approach was employed. This fuel mixture approach, which involves introducing a known amount of hydrocarbon fuel into a well characterized baseline flame, allows the soot production in the flame to be significantly varied while maintaining similar flame size and shape. In order to provide a basis for comparison, the total carbon flow rate in each flame is kept constant. This means that an appropriate fraction of the baseline fuel is replaced by the added fuel species. With the soot contribution from the baseline fuel known, the effect of the added fuel on soot formation can be examined. Methane (CH_4) was employed as the baseline fuel because it displays relatively low soot particle formation and, thus, provides greater sensitivity for measuring changes introduced by varying the fuel molecular structure. A few experiments were also conducted with ethene (C_2H_4) as the baseline fuel to compare the effects between two different baseline fuels.

The experiments have emphasized the methane baseline flames. Table 2 summarizes the flame conditions which have been studied. The experiments involving the fuel addition to methane and

ethene flames were selected to examine three effects. Specifically, the experiments were intended:

(1) To systematically examine the conversion of fuel carbon to soot as function of fuel flow rate. The experiments in which ethene or butene are added to the methane flame addressed this point.

(2) To investigate the relative effects of changing the fuel structure in a series of fuels which involved an alkane, alkene, and alkyne species. The experiments in which butane, 1-butene and 1,3-butadiene were added to the flame addressed this point.

(3) To compare the effects of the baseline fuel on the conversion of fuel carbon to soot for the fuel addition approach. Experiments in which ethene and 1-butene have been added to both baseline flames have been utilized for this comparison.

Table 2. Flow conditions for the fuel addition studies

Baseline Fuel	Flow Rate (cm^3/s)	Fuel Added	Flow Rate (cm^3/s)	Air Flow Rate SCFM
CH_4	8.75	C_2H_4	0.525	2.75
CH_4	7.7	C_2H_4	1.05	2.75
CH_4	5.6	C_2H_4	2.10	2.75
CH_4	5.6	C_4H_8	1.05	2.75
CH_4	5.6	C_4H_8	0.872	2.75
CH_4	7.7	C_4H_8	0.525	2.75
CH_4	5.6	C_4H_{10}	1.05	2.75
CH_4	5.6	C_4H_6	1.05	2.75

The analysis which is presented below focuses on the carbon conversion percentage for each of the flames based on the amount of fuel added to the baseline flame. The contribution of the baseline flame is subtracted from the soot present in the flame based on the studies of the atmospheric ethene

and methane baseline flames. The carbon conversion percentage is calculated for the axial location displaying the maximum value of F_v, the integrated soot volume fraction,

$$F_v = 2\pi \int_0^R f_v \, r \, dr \tag{9}$$

where R is the radius of soot particle field. The carbon conversion percentage can then be expressed as

$$\%\text{conversion} = \frac{\dot{m}_s - \dot{m}_{sB}}{\dot{m}_c - \dot{m}_B} \times 100 = \frac{\dot{m}_s - \dot{m}_{sB}}{\dot{m}_{add}} \times 100 \tag{10}$$

where $\dot{m}_s$ is the soot mass flow rate at the location of maximum F_v for the flame containing the fuel addition, $\dot{m}_{SB}$ is the corresponding soot mass flow rate for the pure baseline flame, $\dot{m}_c$ is the mass flow rate of carbon entering the burner, $\dot{m}_B$ is the mass flow rate of carbon contained as baseline fuel and $\dot{m}_{add}$ is the mass flow rate of carbon corresponding to the fuel species added to the flame. The determination of the soot mass flow rate at a particular height in the flame can be calculated from:

$$\dot{m}_s(z_m) = 2\pi\rho \int_0^R v(r, z_m) \, f_v(r, z_m) \, r \, dr \tag{11}$$

where z_m is the axial location where F_v is a maximum, ρ is the density of soot and v is the velocity. Thus, the velocity profile must be known to precisely calculate the value of $\dot{m}_s$. For the present analysis, the velocity has been assumed to be independent of r with a value for axial location z_m taken from Ref. 3. This is a reasonable assumption for the locations for which F_v is observed to be a maximum [3]. With this assumption $\dot{m}_s$ can be expressed as

$$\dot{m}_s(z_m) = \rho \, v(z_m) \, F_v(z_m) \tag{12}$$

8

where ρ is taken to be 1.8 g/cm^3. Tables 3-5 tabulate the results of this analysis for several of the

flames studied. Included along with the percent conversion result is the calculated adiabatic flame temperature for each flame.

Table 3. Flow conditions for the studies of the fuel flow rate effects

Baseline Fuel	Flow Rate (cm^3/s)	Fuel Added	Flow Rate (cm^3/s)	% Conversion*	T_{ad} (K)
CH_4	8.75	C_2H_4	0.525	21.5	2239
CH_4	7.70	C_2H_4	1.05	19.0	2252
CH_4	5.60	C_2H_4	2.10	16.2	2280
CH_4	7.70	C_4H_8	0.525	36.6	2242
CH_4	5.60	C_4H_8	0.872	33.3	2256
CH_4	5.60	C_4H_8	1.05	35.1	2260

* ρ = 1.8 gm/cm^3

As stated earlier, in the fuel addition approach, a fraction of the baseline is replaced with the fuel species of interest subject to the constraint that the total flow rate of carbon into the flame is maintained constant. It is of interest to ascertain if the percentage of fuel carbon converted to soot is dependent on the amount of the baseline fuel replaced. The results tabulated in Table 3, for a methane baseline flame in which ethene or butene was introduced, provided information on this point. For the ethene fuel addition case, the ethene flow rate was varied by a factor 4, whereas for the 1-butene case the flow rate was changed by a factor of 2. In the case of the 1-butene studies, the percent conversion remained relatively constant. For the ethene case, a small systematic decrease in the conversion percentage of fuel carbon to soot is observed with increasing ethene flow rate. Consideration of the variation in the calculated adiabatic flame temperature (T_{ad}) does not explain the observed results since a decrease in the conversion percentage is opposite to the current view of the effect of temperature on soot production. It is conceivable that the observed variation in the

conversion percentage is within the experimental error. At present, the date supports the conclusion that the conversion percentage is only weakly dependent on the fuel addition flow rate. The differences observed between species with different fuel molecular structure are significantly greater than the observed variations with respect to flow rate. This provides an experimental justification to extend the results of these studies to more general fuel mixture conditions.

Table 4. Flow conditions for the butane, butene, and butadiene addition studies

Baseline Fuel	Flow Rate (cm^3/s)	Fuel Added (cm^3/s)	Flow Rate	% Conversion*	T_{ad} (K)
CH_4	5.6	C_4H_{10}	1.05	12.2	2243
CH_4	5.6	C_4H_8	1.05	35.1	2260
CH_4	5.6	C_4H_6	1.05	44.4	2285

*ρ = 1.8 gm/cm^3

To specifically examine the effect of fuel molecular structure on the soot formation process, a series of flames were examined involving C_4 species. The flames studied involved additions of butane, 1-butene and 1,3-butadiene to a methane baseline flame. In this series, the fuel structure is varied in terms of the arrangement of carbon bonds (single bonds and double bonds) resulting, of course, in a variation of the carbon to hydrogen ratio. Table 4 tabulates the results of these experiments in terms of conversion percentage of fuel carbon to soot. Figure 9 shows the integrated soot volume fraction, F_v, as a function of the axial coordinate, z.

Clearly, the results in Table 4 and figure 9 indicate a strong fuel structure effect with the conversion percentage more than tripling. In addition, there is a systematic decrease in the axial position where soot is first observed as the more sooty fuels are considered. This indicates that the reactions leading to the first soot particles occur more rapidly in these flames.

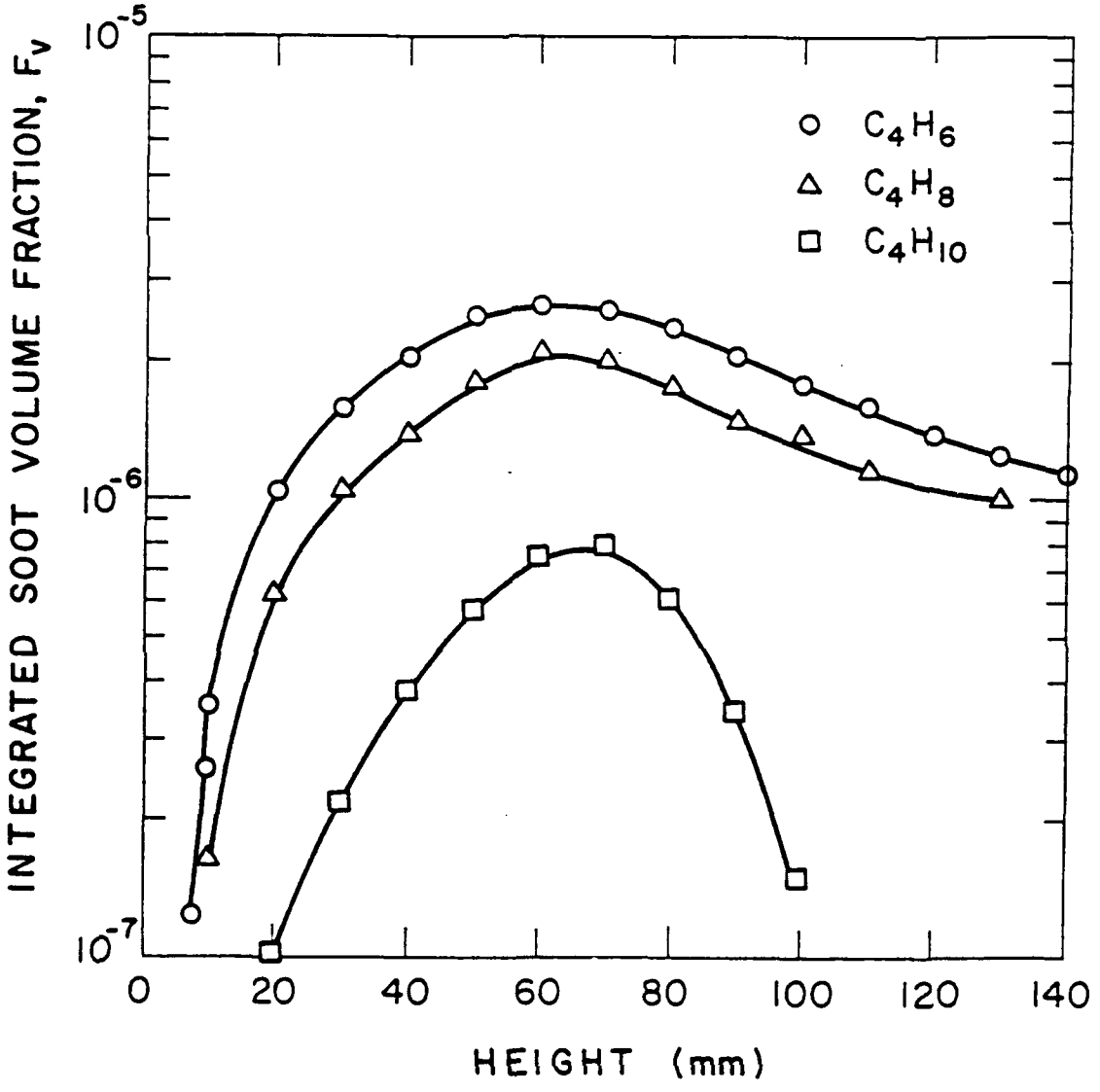

Figure 9. Soot volume fraction integrated over the flame diameter

The discussion above has focused on the effects of fuel molecular structure and flow rate. An additional important consideration is the importance of the baseline fuel which is used. To examine this point, two fuel addition studies involving ethene and butene were compared in which the baseline fuels were varied using methane and ethene. The results of these studies in terms of conversion percentage are tabulated in Table 5.

Table 5. Flow conditions for flame studies of baseline fuel synergism

Baseline Fuel	Flow Rate (cm^3/s)	Fuel Added	Flow Rate (cm^3/s)	% Conversion*	T_{ad} (K)
CH_4	7.7	C_2H_4	1.05	19.0	2252
CH_4	7.7	C_4H_8	0.525	36.6	2242
C_2H_4	3.85	C_2H_4	1.05	16.2	2369
C_2H_4	3.85	C_4H_8	0.525	46.8	2359

*ρ = 1.8 gm/cm^3

These results, as with the flow rate results previously discussed (see Table 3), do show some sensitivity to a variation in the flame conditions. However, again, the differences are significantly smaller than the variation resulting from the fuel structure variation. For the experiments shown in Table 5, the soot conversion percentage approximately doubles for the change in fuel species. However, differences in the results for the various baseline flames for a particular fuel (ethene or butene) is typically 20-25%. It is also worth mentioning that the calculated flame temperatures vary by about 100K for the fuels studied. Thus, some of the variation may be a result of the temperature difference. The comparison between the ethene and butene results may indicate different temperature sensitivities since the observed effects of the baseline flame are reversed.

The above discussion has emphasized the conversion percentage of fuel carbon to soot particles. This quantity is very useful in illustrating the impact of the effect of fuel molecular structure on soot formation. However, it represents a global measurement of the soot formation process. More fundamentally significant results are realized when the detailed temperature time history characterizing these chemically reacting systems are analyzed.

3.3.2 Soot Particle Precursor and Inception Studies

In order to examine the details of the soot formation process, it is useful to follow the temporal evolution of the soot particle field. Thus, measurements resolved along specific particle paths are of more use in developing quantitative results. From measurements of the axial and radial velocity components, the necessary data to provide this information can be obtained [3].

Laser light scattering measurements for soot particle characterization and fluorescence measurements to characterize the soot precursor field prior to particle inception were obtained in butane, 1-butene and 1,3 butadiene mixture studies described above. The fluorescence measurements were obtained by tuning the laser to the 488 nm laser line and observing the fluorescence a 514.5 nm. Previous workers have shown that this fluorescence likely results from large hydrocarbon species, probably aromatic in nature, which are present in the flame [20-23]. Comparisons of the observed fluorescence intensity as the fuel is varied provide a semi-quantitative indication of the effects on the gas phase soot precursors. Unfortunately, such measurements are not species specific and, thus, can not add direct insight into the chemical mechanism leading to soot particle inception.

The results of these fluorescence and soot volume fraction measurements are shown in figure 10. Figure 10 displays the results along the particle path exhibiting the maximum soot formation. The fluorescence measurements are observed to precede the formation of soot particles and then to increase rapidly in the early formation period. The magnitude of the fluorescence signals is observed to be strongly dependent on the fuel molecular structure and vary in a manner very similar to the soot volume fraction as the added fuel is varied. Comparisons along individual particle paths indicate that

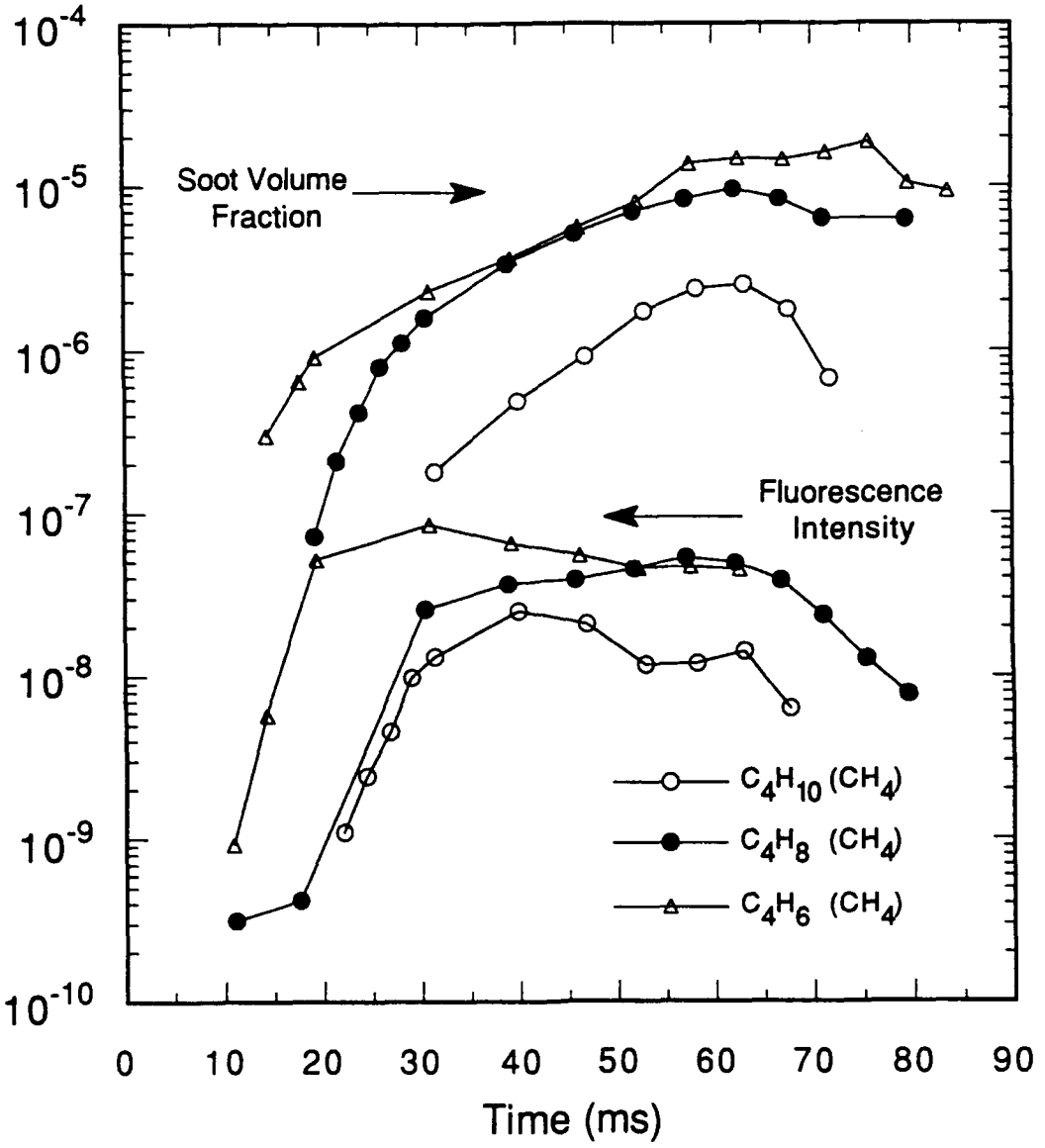

Figure 10. The soot volume fraction and fluorescence measurements along the particle paths containing the maximum soot concentration in the annular region of the flame.

between 20% and 70% of the soot growth occurs prior to the fluorescence achieving a maximum value depending on the particle path location in the flame. This point raises the question as to the participation of large hydrocarbon species in the surface growth process since such species are responsible for the observed fluorescence. This point will be addressed again later in this report.

The results described above lead to the following observations:

1. The species responsible for the observed fluorescence increase in proportion to the sooting tendency of the fuels studied. In this respect, such species satisfy one criteria for representing the soot precursors.
2. These fluorescing species precede the particle inception region throughout the flame zone. This is, of course, a minimal condition for a precursor species.
3. Following particle inception, these species increase rapidly during a significant fraction of the particle surface growth process. This leads to the possibility that such species contribute to the early surface growth process as well as the inception process.

The results described above are quite consistent with results obtained recently in premixed flames with respect to the likely importance of PAH species on soot particle inception [32,33]. Although some work has been obtained under diffusion flame conditions, present results lack the temporal and spatial detail necessary to compare to models of diffusion flames [2,20,23,24]. As the models successfully developed for premixed flames are extended to mixing dominated combustion conditions, there will be a need for a more exhaustive measurement base to provide appropriate comparisons with model prediction. Recent experiences with modeling of soot particle surface growth and oxidation has shown the value of detailed laminar diffusion flame measurements for model validation [1,25-29,30]. A similar effort in the area of soot precursor and particle inception phenomena is certainly warranted. Results similar to those described above in figure 10 can be used presently for comparisons with models for total PAH evolution. However, such comparisons would benefit greatly

from additional measurements of stable as well as radical species in the flame. This should be a priority area for research involving soot formation in diffusion flames.

3.3.3 Surface Growth

Although particle inception is one of the key processes in the formation of soot, it actually accounts only for a small fraction of the mass addition. The major mass addition process involves the surface growth stage which follows inception. A great deal of attention has been given to this process in both premixed and diffusion flames [5,31,32]. Major contributions to the present understanding of surface growth have been made by Wagner [48] and Harris [31]. The mechanisms developed in these studies differ significantly in concept and work is continuing to further understand the surface growth process [37-43].

Most approaches to soot surface growth phenomena argue that acetylene, or a species closely associated with acetylene, provides the major surface reactant. Simple mass balance considerations provide the basis for this observation, since only acetylene appears to be present in sufficient concentration to account for the amount of mass added to the soot particles [31]. However, other workers have pointed out that under suitable conditions large PAH species may directly add to the growing soot particles [32-34]. Since measurements made in diffusion flame are limited to a small number of fuels, it is difficult to presently assess the importance of these PAH species to surface growth processes in soot formation.

Before proceeding further it is worthwhile to review the current understanding of soot particle surface growth process in laminar diffusion flames. In particular, the effect of fuel structure on the amount of soot formed in the flame is useful in this discussion.

The present work at Penn State investigating laminar diffusion flames has shown that the fuel structure effects can be taken into account if variations in the available surface area are considered [4,5,35]. This analysis implies that the initial surface area formed during the particle inception process controls subsequent growth. Returning to the results shown in figure 10, the analysis can be

extended to consideration of the surface growth and oxidation regions of the flame. The discussion above focused on fuel structure effects on particle inception where clearly a strong sensitivity to the fuel is observed. It is equally interesting to determine the effect of fuel molecular structure on the surface growth process for soot particles formed in diffusion flames. An additional point of interest lies in the role that large hydrocarbon species may have in the early surface growth process. This aspect arises from the results described above, in which the fluorescence signals attributed to large PAH species maximized at some significant fraction of the mass addition to the soot particles, thus, allowing the possibility that these species contribute significantly to early soot growth.

The analysis has been carried out along the same particle path for which measurements are shown in figure 10. Similar results have also been obtained for the centerline region of these flames and discussion of those results is also included below. The present approach to the analysis is to represent the soot mass growth rate as

$$\frac{dm}{dt} = k\, S[C_x\, H_y] \qquad (13)$$

where m is the mass of soot (g/cm^3), k is the surface growth rate constant (g/cm^2-s-atm), S is the specific surface area (cm^2/cm^3) and $[C_x\, H_y]$ is the species concentration reacting with the surface to add mass (atm). In the experiments, the product of k and $[C_x\, H_y]$ can be determined since S and dm/dt are determined from the combined light scattering and velocity measurements. This product, $k\,[C_x\, H_y]$, is termed the specific surface growth rate constant. The specific surface area is calculated from the particle diameter and number density measurements, while the soot mass growth rate can be found from the measured soot volume fraction assuming the density of soot particles is 1.8 g/cm^3. Figures 11 and 12 show the specific surface growth rate constant for the C_4 fuel studies in the annulus and along the centerline, respectively. Shortly after the particles are formed, the specific surface growth is close to 2×10^{-4} g/cm^2-s. After a period for which the rate constant is approximately constant, the surface growth rate drops rapidly. It should be pointed out that the

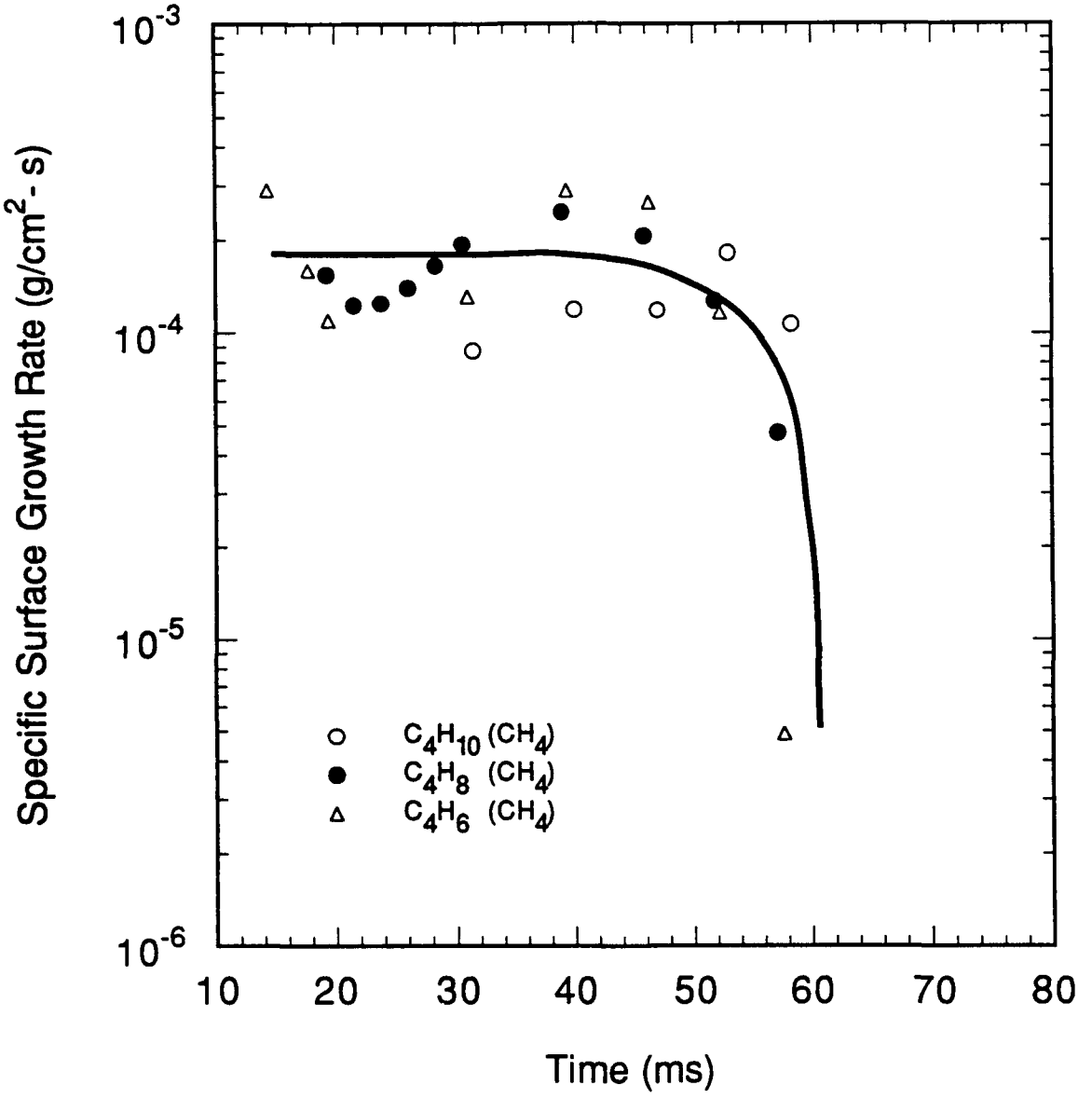

Figure 11. The specific surface growth rate as a function of time for the butane, 1-butene and 1,3 butadiene addition studies to the methane baseline flame. Results are for the particle path containing the maximum value of the soot volume fraction.

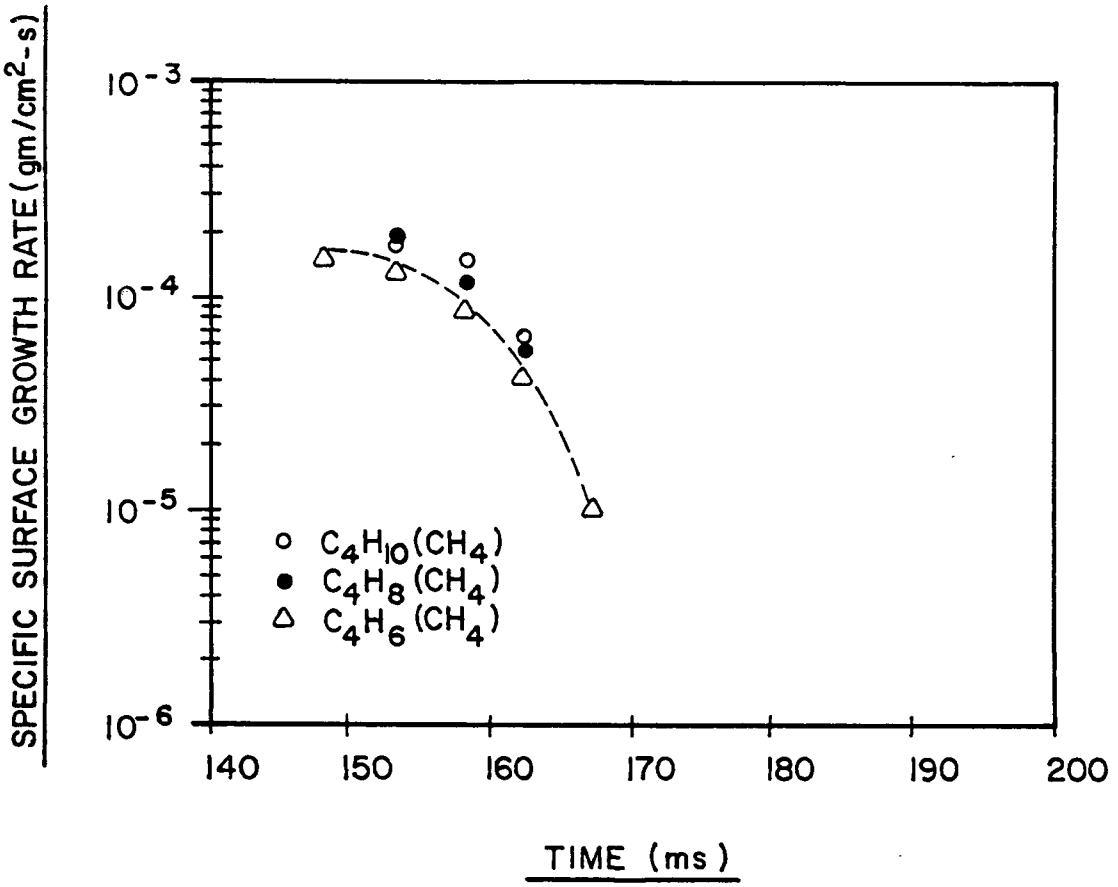

Figure 12. The specific surface growth rate constant as a function of time for the butane, 1-butene and 1,3 butadiene addition studies to the methane baseline flame. Results are for the particle path along the centerline of the flame.

present analysis has been limited to the region of the flame before the soot volume fraction reaches a maximum. Thus, regions where soot particle oxidation dominates have been excluded from consideration.

Figure 13 shows the results for the ethene baseline flame studies where ethene, propene, butene and toluene were added to the flame. Clearly the same behavior is observed in these flames. Also shown in figure 13 are the results of a rich ethene/air premixed flame studied by Harris and co-workers [31]. It is interesting to note that although the temporal behavior of the specific surface growth rate differs, there is order of magnitude agreement between the value for this rate constant in both flame systems.

From these extensive studies, it is clear that the surface growth process is similar in all the flames studied here. Furthermore, since accounting for the differences in available surface area substantially explains differences in the growth processes for flames of widely differing soot concentrations, the value of the initial surface area appears to be critical to subsequent surface growth. Additionally, these studies show that similar values of specific surface growth rate are found throughout the flame for the fuels studied.

Before making further observations concerning the present status of understanding in the area of soot particle surface growth, some discussion of the effect of the fluorescing species in this process is appropriate. Clearly, if the initial surface area is important in all subsequent growth, species involved in the first stages of surface mass addition should be carefully examined. The results described earlier regarding soot particle inception showed that the fluorescence measurements attained a maximum after some significant fraction of the mass due to surface growth had occurred. To quantify the contribution of large hydrocarbon species attributed as the source of the observed fluorescence, a series of highly spatially resolved radial profiles of the soot particle field were obtained for closely spaced intervals along the axis of the flame. These profiles correspond to the earliest data points shown in figure 11. With the exception of the butadiene flame, no systematic

increase in the specific surface growth rate constant is observed. Thus, the present data do not support a model in which the species observed in the fluorescence measurements contribute extensively to the surface growth in the region immediately following particle inception. However, the fluorescence results represent a global measurement of the large hydrocarbon species present in the flame. Recent work in premixed flames by Harris [36] and McKinnon [34] supports a more careful consideration of this matter.

Finally, the results shown in figures 11 through 13 indicate a decrease in the specific surface growth rate constant as reaction time proceeds. This observation has been noted for both premixed and diffusion flames. To date, however, there is no satisfactory explanation for this effect. In general, three mechanisms can be considered as likely candidates. First, the hydrocarbon growth species could be depleted resulting in decreased surface growth. Measurements in fuel-rich premixed flames do not support this mechanism, however, a similar data base for diffusion flames is lacking. A second mechanism involves a decrease in the particle surface reactivity. In this process, as the particle ages in the high temperature flame environment, a loss of radical reactive sites (active sites) on surface results, leading to a decrease in the surface reactivity. Finally, in the case of diffusion flames, there is a distinct possibility that oxidation begins to compete effectively with soot growth, causing the net growth rate to approach zero or even become negative. Previous studies have shown that the emission of soot particles from laminar diffusion flames is strongly affected by temperature, which soot particles influence through radiative transfer [12,24]. The specific local conditions which govern the transition from growth to oxidative destruction is, however, presently not known. An understanding of the transition region between the cessation of soot mass growth and the onset of oxidation would have a significant impact on predictive modeling efforts.

Recently there has been increased interest in the specific phenomena controlling the surface reactivity in soot surface growth processes [32,33,37-40]. Each of these studies has focussed on the concept of active surface sites as reaction centers for the addition of carbon through reactions with gas

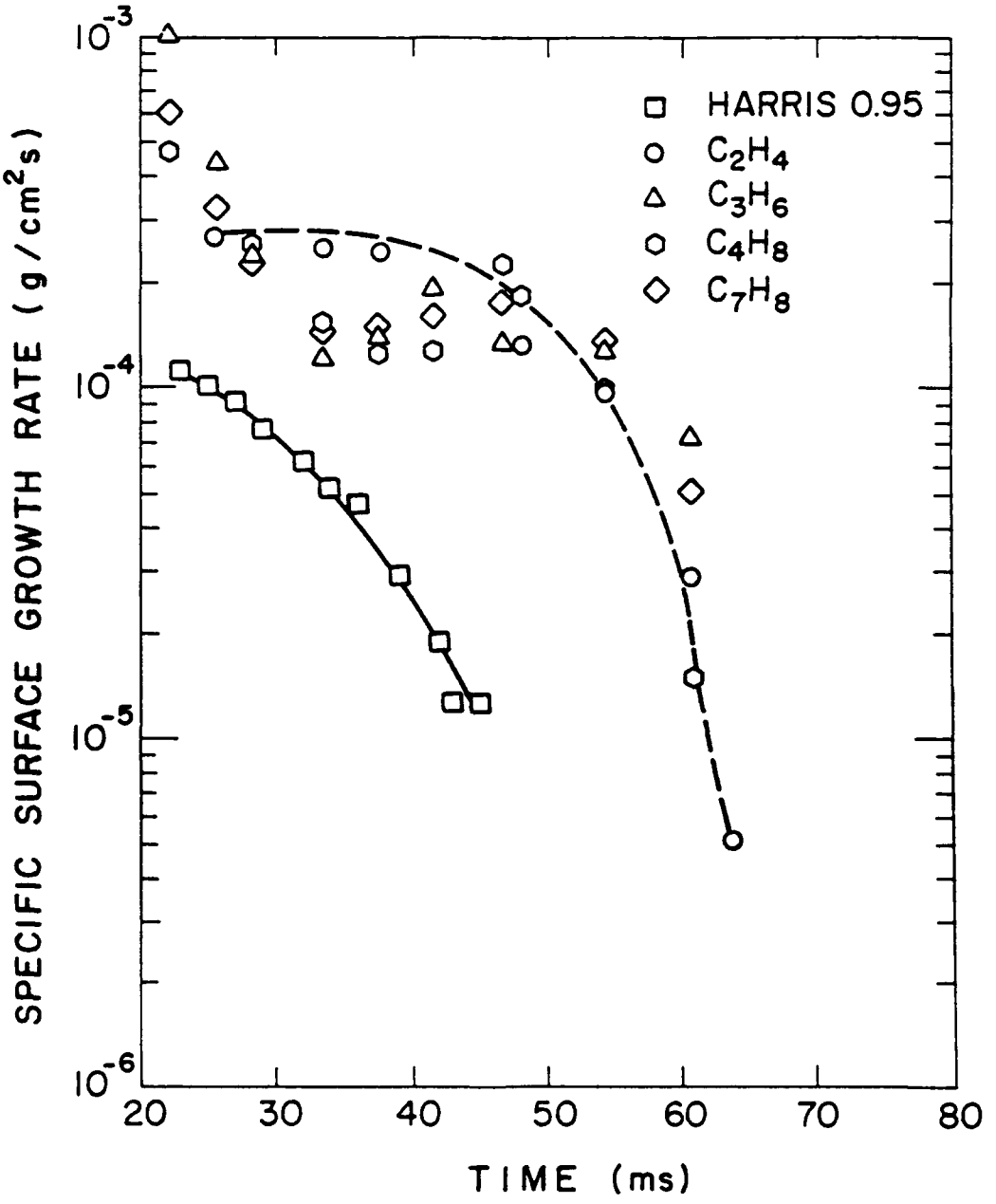

Figure 13. The specific surface growth rate along the particle path exhibiting the maximum soot volume fraction. The dashed line (----) is the best faired curve the ethene flame results.

phase species such as acetylene. The objectives of these studies differ, but they do raise a set of common features. First, soot particles possess highly reactive surfaces, exceeding by two orders of magnitude the reactivity of pyrolytically formed carbon particles (pyrocarbon) [39]. The regeneration of active sites appears to be related to atomic hydrogen reactions with the surface to form new reactive sites [32,33], which have a relativity constant concentration in many situations [38,40]. This approach has been used to reconcile the disparate observations in the literature regarding the sensitivity of the surface growth process to the available soot particle surface area. The results of Harris and Weiner [31,41] indicate a direct proportionality to available surface area as indicated by eq. 13. Results from the work of Haynes et al. [42] and Weischnowsky et al. [43] indicate that the surface growth process is independent of the available surface area. In the recent work, Harris [38], Haynes [40] and Frenklach [32] have replace or augmented the surface area arguments with the addition of a surface active site concentration. Although the details of the representations are different, the basic approach involves similar concepts with regard to the importance of these surface sites. For example, Haynes [40] represents the increase in soot volume fraction with time as:

$$\frac{df_v}{dt} = \alpha \frac{c}{4} N_s A_s v_g N_g \tag{14}$$

where f_v is the soot volume fraction, α is the growth reaction probability on collision, N_g is the number density of gas phase growth species, v_g is the molecular volume of the growth species when incorporated in the soot particle, c is the mean free speed of the gas phase growth species $(8kT/\pi m_g)^{1/2}$, N_s is the total concentration of active sites and A_s is the active area of a single site. In this representation the difference in the experimental results is determined by the behavior of the active sites in the various flames. In the results of Harris and Weiner [31,41] the active site concentration remains nearly constant and, thus, scales with particle surface area. In contrast, for the higher temperature flame studies by Haynes et al. [42] and Weischnowsky et al. [43], the surface site concentration is determined to decrease with time. The basis for the decay in the active surface site is

not known, although the higher temperature flames can be argued to provide an environment in which more rapid annealing of the soot particles may be present. Frenklach [32] has argued in a somewhat similar manner that the state of the initial surfaces of the soot particles may differ in the two flames with the higher temperature flames having fewer active sites.

The above work illustrates the detail to which present soot models and experiments can consider the fundamental mechanisms controlling individual processes. Although this modeling capability is impressive, there is little data particularly under diffusion flame conditions to compare with model prediction. Clearly, the results of the present project point to the need for further measurements obtained under conditions which allow detailed comparisons with mechanistic models for surface growth.

Despite the questions concerning the specifics of the surface growth mechanism, recent efforts to model soot particle growth in diffusion flames have met with some success in reproducing the general features of the soot formation process [26]. However, the model representation for the surface growth process shows a strong sensitivity to the specific surface growth rate constant. In this case, small differences in the growth rate constant could be argued to be responsible for variations in the sooting propensity of various fuels. In the discussion of the results shown in figures 11 through 13, emphasis was given to the importance of the available surface area and the critical nature of the inception process which controls initial soot surface area. Thus, we have argued along with others [44] that inception is controlling the amount of soot ultimately formed in the flame. From the modeling studies of Kennedy [26], this conclusion has been challenged based on the observation that in heavily sooting flames such as those involving ethene [2,3] surface growth controls the amount of soot formed. Since these modeling studies used the ethene data shown in figure 13 to validate the model, the observations by Kennedy provide a good justification for carefully reconsidering the analysis of these flames and assessing the need for further study of surface growth in laminar flames.

In fact, it is clear that more comparisons with the model for a wider range of fuels would be extremely valuable. For such comparisons, not only must the soot particle field be determined, but the major gas phase species also need to be determined. This latter requirement is due to the fact that the Kennedy model uses a measured mixture fraction relationship for each fuel studied [26].

3.4 Concentration and Temperature Effects

A detailed study has been made of the relative effects of concentration and temperature on soot formation in diluted laminar ethene/air diffusion flames employing: (1) argon and nitrogen diluted flames at equal calculated adiabatic flame temperatures but different initial concentrations to isolate the effect of concentration and 2) argon and nitrogen diluted flames with equal initial fuel concentrations but different temperatures to isolate the effect of temperature. Total integrated soot volume fraction measurements show that in argon and nitrogen diluted flames with equal calculated adiabatic flame temperatures, the more diluted argon flames consistently display lower soot concentrations. However, in flames of equal dilution, argon flames consistently display higher soot concentrations than the slightly cooler nitrogen diluted flames. Local temperature measurements show that for nitrogen and argon diluted flames with equal calculated adiabatic flame temperature, argon diluted flames display lower temperatures in the region where soot is first formed. Mass spectrometric measurements of gas concentrations in diluted and undiluted methane/air diffusion flames were obtained and compared with a numerical flame model. These results show that the initial difference in fuel concentration in diluted and undiluted flames diminishes rapidly with height. Furthermore, laser light scattering measurements show that as inert diluent is added to the flame, soot inception is delayed and consequently less time is available for soot growth. Based on this extensive set of data, a quantitative assessment was made of the relative effects of temperature and concentration indicating that for coflow diffusion flames, the role of temperature is more important than the decrease in reaction rate due to the reduction in fuel concentration when an inert diluent is added to the fuel flow.

A complete treatment of the results of these studies has been submitted to *Combustion Science and Technology* for publication and is attached as Appendix 1.

3.5 Analysis of Light Scattering From Soot Particles Using Optical Cross Sections for Aggregates

Soot formed in flames usually consists of aggregates (clusters or agglomerates) of a variable number of nearly spherical, monodisperse primary particles (monomers or spherules). In this work, the optical properties of polydisperse aggregates are used to analyze light scattering data from a coannular ethene diffusion flame. In previously reported studies, data have been obtained on the local extinction and volumetric scattering cross sections from laser scattering experiments, on the flame velocity field from laser velocimetry, and on the primary particle sizes determined by electron microscopy. The present analysis yields the average number of primary particles per aggregate, the mean-square radius of gyration, the soot volume fraction and the aggregation rate. It is found that sustained collisional growth of the aggregates occurs while their primary particles grow through heterogeneous reactions low in the flame, and contract through surface oxidation in the upper half of the flame. A recent value of the refractive index gives internally consistent moment ratios of the aggregate size distribution function. This method of analysis provides a more detailed and complete description of the formation, growth and oxidation of soot aggregates in a diffusion flame.

A complete treatment of the problem of aggregate structure on interpretation of soot particle properties is contained in Appendix 2. This appendix contains a reprint of a recent article published in the *Twenty-Third Symposium (International) on Combustion*.

3.6 Operating Pressure Effects on Soot Formation

A series of laminar diffusion flames have been studied over a range of pressures between 1 and 10 atm (.1 MPa to 1.0 MPa). The coannular diffusion flame burner and laser diagnostics for soot particle measurements were similar to those used for atmospheric flame studies previously reported.

The coannular burner has been mounted in a high pressure cell which was extensively described earlier. The studies undertaken involved laminar diffusion flames burning ethene (C_2H_4), ethane (C_2H_6) and a mixture of ethane and propene (C_3H_6) in air. The measured soot volume fraction is obtained from laser extinction measurements and is represented by [45]:

$$-\int_{-\infty}^{\infty} f_v \, dx = C(\lambda,m) \ln (I/I_o) \tag{15}$$

where f_v is the local soot volume fraction, x lies along a laser path through the flame on a diameter, $C(\lambda,m)$ is a constant which can be determined from Rayleigh light scattering theory to be 1.05×10^{-5} for $m=1.57-0.56\,i$ at $\lambda=514.5$nm [45], and finally I/I_o is the ratio of the transmitted to incident laser power. This quantity is proportional to the total soot present at a particular axial location in the flame. Figure 14 shows this quantity as a function of the non-dimensional axial location for the ethene/air flames at a series of operating pressures. The non-dimensional axial position is expressed as

$$\eta = (ZD/Q) \ln (1 + 1/s) \tag{16}$$

where Z is the axial position, D is the diffusion coefficient, Q is the volumetric fuel flow rate and S is the volume of air to the volume of fuel required for complete combustion.

If the increase in the maximum soot volume fraction at a particular operating pressure is related to that pressure through a power law dependence, that is

$$\left(\int f_v \, dx\right)_{max} \alpha P^n \tag{17}$$

then a fit to the data can be used to yield a value for n. Figure 15 shows the maximum soot volume fractions as a function of the operating pressure along with the best fit value for n determined from a linear least square procedure. For the ethene flame, the fuel flow rate was 3.9 cm^3/s and n was found to be $1.05 \pm .06$ in good agreement with the results of Flower and Bowman [45] who found

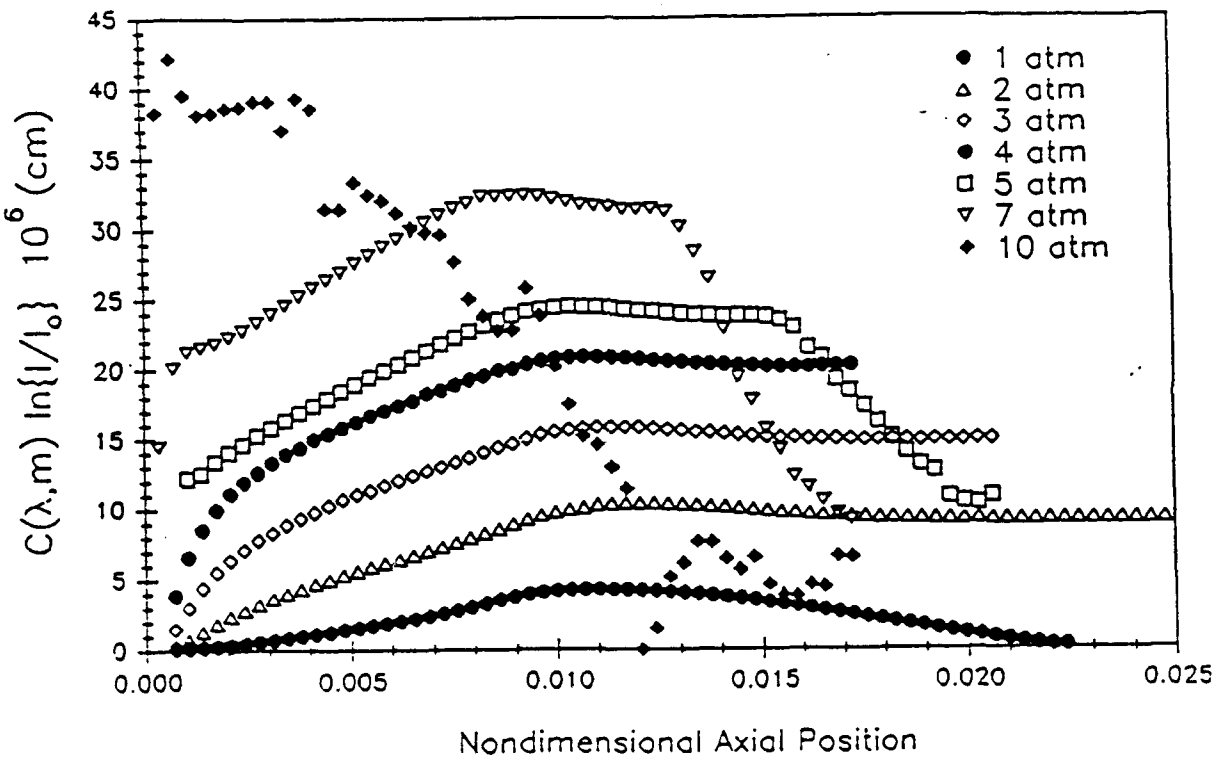

Figure 14. $C(\lambda,m)$ ln (I/I_o) as a function of the non-dimensional position, η, for the ethene/air laminar diffusion flames for operating pressures between 1 and 10 atm. The non-dimensional axial position is given by $\eta=(zD/Q)$ ln $(1+1/s)$, where z is the axial position, D is the diffusion coefficient (0.156 cm^2s^{-1}), Q is the fuel flow rate (3.9 cm^3/s) and s is the volume of air to the volume of fuel required for complete combustion. ($S=14.28$ for C_2H_4).

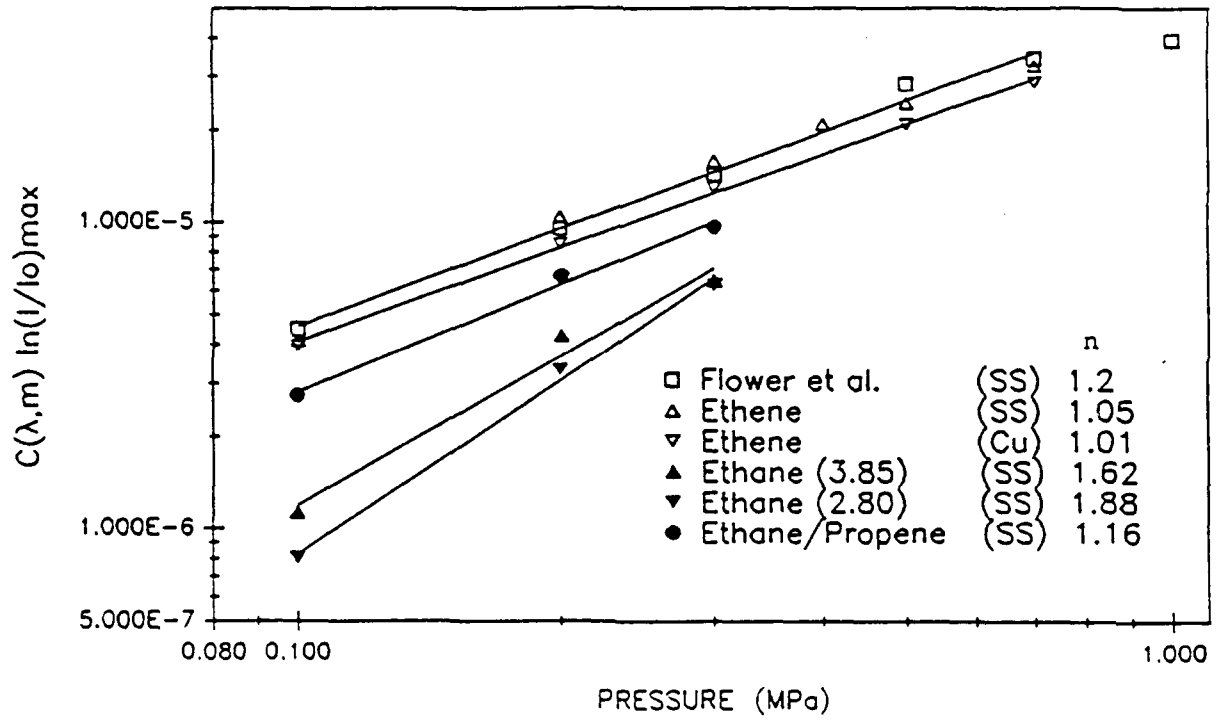

Figure 15. $C(\lambda,m)\ \ln (I/I_o)/_{max}$ as a function of operating pressure for a series of ethene, ethane and ethane/propene laminar diffusion flames burning in air. Solid lines are fits to P^n.

$n=1.2\pm0.1$. It should be noted that results shown in figures 14 and 15 have taken into account the slight burner diameter difference for the two studies. In the present study, the diameter was 1.1 cm where as Flower and Bowman employed a burner with a 1.27 cm diameter. Also shown on figure 15 are the results for an ethene/air diffusion flame where a copper (Cu) rather than a stainless steel (SS) fuel tube was utilized. The results are very similar for both fuel tube materials. Although the higher heat loss characteristics of the copper fuel tube were observed to slightly reduce the amount of soot formed as compared to the stainless steel case, the pressure dependence is largely unaffected by the fuel tube material.

Figure 15 also shows the results obtained for flames burning ethane or an ethane/propene mixture. For these flames, the pressure could only be varied over a range of 1 to 3 atm (.1 to .3 MPa) before a buoyancy driven flame instability was observed. These buoyancy effects, at elevated pressure, have recently been the subject of a collaborative investigation with workers at the National Institute of Standards and Technology (NIST) [46] and are discussed elsewhere in this report. An analysis similar to that applied to the ethene flame studies yields pressure power dependences of $n=1.88\pm0.13$ and $n=1.62\pm0.24$ for ethane fuel flow rates of 2.80 and 3.85 cm^3/s, respectively. These higher values of the pressure power dependence appear to be related to fuel structure effects, the direct nature of which remains to be understood. These observations of a fuel structure dependence are consistent with previous studies [47].

As a further investigation of fuel molecular structure effects, a mixture of ethane (2.80 cm^3/s) and propene (0.7 cm^3/s) was studied and these results are also shown in figure 15. In the ethane/propene study, the total carbon atom fuel flow rate was maintained constant with respect to the 3.85 cm^3/s ethane flame. For these conditions, the value of n is observed to be 1.16 ± 0.10, a value similar to that observed for the ethene studies. Thus, the present studies with an alkane species appear to yield a higher pressure dependence than observed for either of the alkene species. This occurrence of a variation in the pressure dependence may be important in providing an understanding

of the differences observed in premixed and diffusion flame studies at high pressure. For premixed flames, pressure dependence studies have yielded values of n=2 [48] as compared to the values of n between 1 and 1.2 reported for ethene. The higher values of n for the ethane flames are closer to the values observed in premixed flames. The cause of the higher pressure dependence obtained for the ethane diffusion flames remains to be established. Fuel structure effects may be reflected in the lower soot volume fractions rather than explicitly different chemical mechanisms. Premixed flame studies have examined a variety of fuels, including ethene and benzene, and obtained a P^2 dependence on pressure. The present experiments provide some important additional information for consideration in resolving the actual pressure dependence for soot formation processes and indicate further study of high pressure diffusion flames is required.

3.7 Isolation of Buoyancy Effects in Jet Diffusion Flame Experiments

The occurrence of instability phenomena in flames has been a topic of interest in combustion for a variety of reasons. Instability processes have been observed to enhance mixing and, thus, accelerate chemical reaction progress. Less favorable results have been observed to accompany combustion instabilities as well. For gas turbine and rocket engines, combustion instabilities can present serious operational problems and may, in fact, lead to catastrophic engine failure. In such cases, expensive engine redesign or implementation of damping devices has been necessary to resolve the problem. Clearly, a desirable situation would be one in which the potential benefits to enhanced mixing could be realized without the penalties of hardware performance loss. This requires a fundamental understanding of phenomena which controls the initiation and growth of the instability. One of the obstacles to achieving such an understanding lies in the inability to study instability phenomena under well controlled conditions.

In addition to the combustion instability interests, turbulence combustion phenomena may also be influenced by instability phenomena. The occurrence of well ordered structures in turbulent flames has been a subject of great interest over the preceding decade. Although often observed, the

importance of such features with respect to the transition to turbulent combustion conditions is still an area of active investigation. An understanding of the basic mechanisms controlling the onset of these structures is still lacking.

Recently, an interesting flame instability phenomena was observed during the study of soot formation in high pressure diffusion flames which possesses many of the desired features for the study of this phenomena. The flame instability was observed to evolve from a stable methane/air diffusion flame as the pressure was raised from one atmosphere (14.7 psia) to approximately 6 psig (20.7 psia). At this pressure, the flame exhibited a regular pulsation or oscillation. In order to examine this phenomena further, a series of high speed video images of this methane flame were recorded. These images were obtained at a framing rate of 500 frames per second and simply recorded the flame luminosity from the soot present in the flame. Analysis of these video recordings revealed the onset and evolution of a very regular flame structure with a repetition rate of approximately 15 Hz. Several attempts were made to eliminate these pulsating flames by modifying the pressure chamber with baffles or screens. These changes were intended to alter the acoustic modes of the chamber or to impede flow recirculation. None of these approaches significantly affected the phenomena. Thus, the observed oscillations are not believed to be an artifact of the apparatus.

Previous researchers have observed similar self-excited instabilities in laminar fuel jets [49,50]. In these studies, the fuel flow rate was varied to produce the onset of the instability. Analysis explaining the oscillatory behavior emphasized perturbations introduced into the velocity field which were amplified through either linear or non-linear mechanisms [49,50]. More recent work has placed a stronger emphasis on the effect of buoyancy in both laminar and turbulent flow regimes [51,52-55]. The general trends indicate that as Reynolds number increases ($Re > 7000$), the effect of these buoyancy related instabilities is less important [51,55]. The present evidence is not conclusive on the potential importance of such low frequency instabilities with regard to turbulent flows. There are studies which indicate that the above observed instabilities can couple to the inner core flow of the jet

and may be important in the dynamic processes which occur during transition to fully turbulent conditions [51,54]. Recent visualization studies of atmospheric pressure diffusion flames have shown that these flames are characterized by complex vortical structures [54].

The general flame structure of the present high pressure oscillating flames is similar to that reported in the studies referenced in the above discussion. The observed frequency is quite close to the 17 Hz frequency predicted by the analysis of Buckmaster and Peters [52]. Thus, it seems clear that these instability features are buoyancy driven. Recent modelling results for unsteady buoyancy-driven jet diffusion flames conducted at NIST have been quite successful in reproducing the general characteristics of the observed flames [46]. In the formulation of this model, three dimensionless parameters enter into the formulation: the Reynolds number, the Peclet number and the Richardson number. In the present experiments, because the mass flow rates of fuel and oxidizer are maintained at a constant value, the product of the density and inlet gas velocity remains constant as the pressure is changed. Since the viscosity is independent of the pressure, the Reynolds number also remains constant as the pressure is varied. In the limit of unity Lewis number, the Peclet number is equal to the fuel jet radius multiplied by the ratio of inlet gas velocity and the binary diffusion coefficient of the fuel. Since both the inlet gas velocity and the diffusion coefficient are inversely proportional to the pressure, the Peclet number also remains constant. Finally, the Richardson number, which expresses the ratio of buoyancy forces to inertial forces, can be expressed as gL/U^2 where g is the gravitational constant, L is the fuel jet radius and U is taken as the air inlet velocity. Clearly, this number will vary with the square of the pressure through the velocity term in this ratio. Thus, the effective gravitational acceleration will vary as the pressure squared. Consequently, in the model, a pressure of two atmospheres can be simply simulated by choosing a gravitational constant of 4 g.

The significance of the present experimental configuration is that relative effects of buoyancy can be examined in isolation from the other parameters. This situation is unique to this burner

configuration and offers an excellent opportunity for investigating the fundamental aspects of the instability onset from both experimental and theoretical modelling aspects.

Model comparisons with the imaging results described above show good agreement with respect to the instability frequency and tip cutting location [46]. This agreement includes the predication of the observation that the tip cutting location decreases as the pressure increases. One area where a ment has not been obtained to date, involves the pressure at which the onset of the instability is observed. The model predicts a pressure of about one half that observed experimentally. Appendix 3 contains a detailed discussion of the model and experiment comparisons.

Additional experiments using ethane and ethene have also displayed similar flame instability behavior as the pressure is increased. For each flame, however, the onset of the instability occurs at distinctly different pressures, even though the gas flow rates are identical. Thus, a measurable fuel dependence is observed with respect to the onset conditions. Previous studies at atmospheric conditions have not investigated fuel related effects, because the instability frequency generally is not strongly affected [52]. For the high pressure initiated instabilities, however, measurable fuel constituent effects are observed and, thus, provide a potential for further insights into the instability phenomena.

4.0 CONCLUSIONS

A fundamental study of soot particle inception and growth processes has been completed which specifically considered the effects of fuel molecular structure, fuel concentration, temperature and operating pressure on the formation of soot particles. Coannular laminar diffusion flames burning in air were studied for pure fuels (methane and ethene) as well as fuel mixtures involving ethene propene, butane, 1-butene and 1,3 butadiene individually mixed with methane or ethene. The fuel structure studies indicated that the fuel species most strongly affected the particle inception process for the fuels studied, as opposed to the surface growth process. Laser fluorescence measurements indicate that the soot particle precursors concentrations increased and were observed sooner in the flame as the sooting propensity of the fuel increased. Surface growth rate constants, when normalized by the available surface area, were typically within a factor of two for the fuels studied. These findings support an interpretation in which inception controls the maximum amount of soot formed in the flame.

Studies in which fuel concentration and flame temperature were varied through dilution of fuel with an inert species indicated that temperature effects dominate changes due to variations in the concentration under most conditions. Local temperature and concentration measurements were shown to be absolutely necessary to properly interpret the effects of inert dilution. In particular, small temperature differences in the initial soot formation region, as well as the mitigation of the initial concentration at the fuel tube exit by inter-diffusion of nitrogen from the air stream and fuel, were shown to make simple interpretation of the effects of dilution problematic. Based on studies over a wide range of flow conditions, it was possible to estimated the separate effects of dilution and concentration. This estimate showed that for the conditions studied, the temperature effects dominate over the concentration effects. The analysis yielded an apparent activation energy of 94.5 kcal/mole for the temperature dependence. The fuel concentration dependence, represented as $[X_o]^n$, where X_o is the fuel concentration at the exit of the fuel tube, was best represented by $n = 0.3$.

Studies of the evolution of the soot particles in laminar diffusion flames indicated that clusters or aggregates are found in the higher parts of the flame. These clusters, which are composed of nearly spherical primary particles, possess different optical properties from their spherical equivalents. Through a combination of transmission electron microscope and laser light scattering measurements, an analysis of the optical properties of these aggregates was developed.

A data reduction method that is based on the use of optical cross sections for aggregates was applied to measurements of local extinction and differential scattering at three angles by soot aggregates in a laminar ethene diffusion flame. As compared to the Rayleigh data reduction for spherical particles, this method yields higher values of volume-mean diameter, a larger surface area per unit volume, and lower values of the aggregate number concentration. The analysis also provides the mean-square radius of gyration and the average number of primary particles per aggregate. Both these quantities increase monotonically with time as is consistent with the occurrence of cluster-cluster aggregation. Primary particle diameter is also obtained from the optical observations and it has been independently measured by thermophoretic sampling followed by TEM analysis. By requiring the rms difference between the two observations of primary particle size to be a minimum, information on the allowable values of refractive index was obtained. Higher values of the real portion of the refractive index give more plausible moment ratios of the size distribution of the aggregates. The present results indicate that a self-consistent interpretation of the light scattering properties of the soot aerosol is afforded by recognizing its aggregate structure. In particular, significant differences in the surface area and number concentration are observed for soot aerosols consisting of aggregates of primary particles. These differences have important ramifications in deriving chemical and physical rate data from the laser scattering extinction experiment. Furthermore, when combined with TEM analysis of the primary particles which constitute the aggregates, this analysis provides the basis for evaluating the importance of other particle properties, such as refractive index. Thus, this method of data analysis provides a more detailed and comprehensive description of the development and

character of the soot aggregate population in laminar diffusion flames.

Operating pressure effects on soot formation were also studied. These studies indicated that a power law representation of the form of P^n, where P is the operating pressure, accurately represented the behavior of the soot volume fraction as the pressure was varied. For studies involving the alkene species, ethene and propene, the value of n was found to be close to first order (1.05 ± 0.06 and 1.16 ± 0.01, respectively). Studies of an alkane fuel, ethane, resulted in a significantly larger value for the power dependence closer to second order in n (1.62 - 1.88, depending on the flow rate). These results confirm the strong dependence of soot formation on the operating pressure and furthermore point to potential fuel structure effects.

Finally, studies of these high pressure diffusion flames have resulted in the observation of the onset of buoyant instabilities induced by changes in the pressure. A simple procedure has been described for isolating these buoyancy effects in jet diffusion flame experiments. All that is necessary is that background pressure be varied while maintaining constant mass flows of fuel and oxidizer into the burner. A theoretical model for these flames indicates that this procedure isolates Richardson number (or relative buoyancy force) as the only variable parameter, which is equivalent to varying the gravitational acceleration. A joint series of experiments and computations involving a pressurized low speed methane/air diffusion flame has provided strong evidence to support the theory.

It is clear that much work needs to be done in order to clarify the important role that buoyancy plays in jet diffusion flame dynamics. The results of the present studies only open the door to future studies, which can now be performed with reasonable effort and cost-effectiveness. Future research is also needed in order to determine the limits of usefulness of the buoyancy-isolation procedure described here. Clearly, use of this procedure to attain very small effective gravitational accelerations appears unreasonable, as chemical kinetics could certainly not be ignored at the low pressures required. Additionally, enhanced soot production at low g would not be simulated by this pressure variation technique. However, relaxation of the requirement that Lewis number be unity appears

feasible, since Prandtl and Schmidt numbers can both be considered as independent of pressure. Finally, since the basic model described here is not dependent on a particular geometry, other types of diffusion flames in different burner configurations could also be considered as candidates for buoyancy-isolation experiments. Thus, the possibilities for future research efforts in the area of buoyancy effects in diffusion flames appear rather substantial.

5.0 REFERENCES

1. Dobbins, R. A., Santoro, R. J. and Semerjian, H. G., "Analysis of Light Scattering From Soot Particles Using Optical Cross Sections for Aggregates," *The Twenty-Third Symposium (International) on Combustion*, The Combustion Institute, Pittsburgh, pp. 1525-1532 (1990).

2. Santoro, R. J., Semerjian, H. G. and Dobbins, R. A., "Soot Particle Measurements in Diffusion Flames," *Combustion and Flame*, 52, pp. 204-218 (1983).

3. Santoro, R. J., Yeh, T. T., Horvath, J. J. and Semerjian, H. G., "The Transport and Growth of Soot Particles in Laminar Diffusion Flames," *Combustion Science and Technology*, 53, p. 89 (1987).

4. Santoro, R. J., "Fuel Molecular Structure Effects on Soot Particle Growth in Diffusion Flames," *Twentieth Fall Technical Meeting of the Eastern Section of The Combustion Institute*, Paper #19, Nov. 2-5, 1987, Gaithersburg, MD.

5. Richardson, T. F. and Santoro, R. J., "Soot Growth in Diffusion Flames Burning Fuel Mixtures," *Twenty-First Fall Technical Meeting of the Eastern Section of The Combustion Institute*, Paper #44, December 5-7, Clearwater Beach, FL.

6. Santoro, R. J. and Richardson, T. F., "Concentration and Temperature Effects on Soot Formation in Diffusion Flames," in *Mechanisms and Models of Soot Formation*, Springer Verlag (in press).

7. Puri, R., Richardson, T. F., Santoro, R. J. and Dobbins, R. A., "Aerosol Dynamic Processes of Soot Aggregates in a Laminar Ethene Diffusion Flame," submitted to *Combustion and Flame*.

8. Richardson, T. F. and Santoro, R. J., "Soot Formation in Coannular Diffusion Flames: The Effect of Fuel Dilution with Inert Species," submitted to *Combustion Science and Technology*.

9. Smyth, K. C., Miller, J. H., Dorfman, R. C., Mallard, W. G. and Santoro, R. J., "Soot Inception in a Methane/Air Diffusion Flame as Characterized by Detailed Species Profiles," *Combustion and Flame*, 62, pp. 157-181 (1985).

10. Puri, R. and Santoro, R. J., "Sonic Probe Sampling in Particle Laden Combustion Flows," *The 1990 Fall Technical Meeting of the Eastern Section of The Combustion Institute*, paper #147, Orlando, FL, December 3-5, 1990.

11. Mitchell, R. E., Sarofim, A. F. and Clomburg, L. A., "Experimental and Numerical Investigations of Laminar Diffusion Flames," *Combustion and Flame*, 37, pp. 227-244, 1980.

12. Kent, J. H. and Wagner, H. Gg., "Why Do Diffusion Flames Soot?" *Combustion Science and Technology*, 41, pp. 245-269 (1984).

13. Schalla, R. L. and Hubbard, R. R., "Formation and Combustion of Smoke in Flames," in

Basic Considerations of Hydrocarbon Combustion, NACA Report 1300, Chap. IX (1959).

14. Schug, K. P., Manheimer-Timnat, Y., Yaccarino, P. and Glassman, I., "Sooting Behavior of Gaseous Hydrocarbon Diffusion Flames and the Influence of Additives," *Combustion Science and Technology*, 22, pp. 235-250 (1980).

15. Bahr, D.W. "Impact of Broad-Specification Fuels on Aircraft Turbine Engine Combustors", *J. Energy*, 6, pp. 392-398 (1982).

16. Jackson, T.A., "Fuel Property Effects on Air Force Gas Turbine Engines - Program Genesis", *J. Energy*, 6, pp. 376-383 (1982).

17. Strauss, K.H., "Future U.S. Jet Fuels - A Refiner's Viewpoint", *J. Energy*, 7, pp. 200-203 (1983).

18. Blazowski, W.S., "Future Jet Fuel Combustion Problems and Requirements", *Prog. Energy Combust. Sci.*, 4, pp. 177-199 (1978).

19. Santoro, R. J., Semerjian, H. G., Emmerman, P. J. and Goulard, R., *Int. J. Heat and Mass Transfer*, 24, pp. 1139-1150 (1981)

20. Miller, J. H., Mallard, W. G. and Smyth, K. C., "The Observation of Laser-Induced Visible Fluorescence in Sooting Diffusion Flames", *Combustion and Flame*, 47, pp. 205-214 (1982).

21. Cincotti, V., D'Alessio, A., Menna, P. and Venitozzi, C., "U. V. Absorption Spectroscopy and Laser Excited Fluorescence in the Study of Formation of High Molecular Mass Compounds in the Rich Combustion of Methane", *La Rivista dei Combustibili*, 35, pp. 59-68 (1981).

22. Coe, S. D., Haynes, B. S. and Steinfeld, J. D., "Identification of a Source of Argon-Ion-Laser Excited Fluorescence in Sooting Flames", *Combustion and Flame*, 43, pp. 211-214 (1981).

23. Petarca, L. and Marconi, F., "Fluorescence Spectra and Polycyclic Aromatic Species in a N-Heptane Diffusion Flame", *Combustion and Flame*, 78, pp 308-325 (1989).

24. Santoro, R. J. and Semerjian, H. G., "Soot Formation in Diffusion Flames: Flow Rate, Fuel Species and Temperature Effects", *Twentieth Symposium (International) on Combustion*, The Combustion Institute, Pittsburgh, pp. 997-1006 (1984).

25. Honnery, D. R. and Kent, J. H., "Soot Formation in Long Ethylene Diffusion Flames", *Combustion and Flame*, 82, p. 426-434 (1990).

26. Kennedy, I. M., Kollmann, W. and Chen, H.-Y., "A Model for Soot Formation in Laminar Diffusion Flames", *Combustion and Flame*, 81, pp. 73-85 (1990).

27. Megaridis, C. M. and Dobbins, R. A., "Morphological Description of Flame-Generated Materials", *Combustion Science and Technology*, 71, pp. 95-109 (1990).

28. Megaridis, C. M. and Dobbins, R. A., "Comparison of Soot Growth and Oxidation in Smoking and Non-Smoking Ethylene Diffusion Flames", *Combustion Science and Technology*, 66, pp. 1-16 (1989).

29. Dobbins, R. A. and Mulholland, G. W., "Interpretation of Optical Measurements of Flame Generated Particles", *Combustion Science and Technology*, 40, pp. 175-191 (1984).

30. Kent, J. H. and Honnery, D., "A Soot Formation Rate Map for a Laminar Ethylene Diffusion Flame", *Combustion and Flame*, 79, pp. 287-298 (1990).

31. Harris, S. J. and Weiner, A. M., "Surface Growth of Soot Particles in Premixed Ethylene Air Flames," *Combustion Science and Technology*, 31, pp. 155-167 (1983).

32. Frenklach, M. and Wang, H., "Detailed Modeling of Soot Particle Nucleation and Growth", *Twenty-Third Symposium (International) on Combustion*, The Combustion Institute, Pittsburgh, pp. 1559-1566 (1990).

33. Howard, J. B., "Carbon Addition and Oxidation Reactions in Heterogenous Combustion and Soot Formation", *Twenty-Third Symposium (International) on Combustion*, The Combustion Institute, Pittsburgh, PA, pp. 1107-1127 (1990).

34. McKinnon, J. T., Jr., "Chemical and Physical Mechanisms of Soot Formation", Ph.D. Thesis, Massachusetts Institute of Technology.

35. Santoro, R. J., "Optical Measurements of Soot Particles in Flames", *Mat. Res. Soc. Symp. Proc.*, 117, pp. 157-163 (1988).

36. Weiner, A. M. and Harris, S. J., "Optical Detection of Large Soot Precursors", *Twenty-Second Symposium (International) on Combustion*, Poster Session (1988).

37. Dasch, C. J., "The Decay of Soot Surface Growth Reactivity and Its Importance in Total Soot Formation", *Combustion and Flame*, 61, pp. 219-225 (1985).

38. Harris, S. J., "Surface Growth and Soot Particle Reactivity", preprint, 1989.

39. Tesner, P.A., "Growth Rate of Soot Particles", *Combustion and Flame*, 85, pp. 279-281 (1991).

40. Woods, I.T. and Haynes, B.S., "Soot Surface Growth at Active Sites", *Combustion and Flame*, 85, pp. 523-525 (1991).

41. Harris, S. J. and Weiner, A. M., "Determination of the Rate Constant for Soot Surface Growth", *Combustion Science and Technology*, 32, pp. 267-275 (1983).

42. Haynes, B.S., Jander, H. and Wagner, H.Gg., "The Effect of Metal Additives on the Formation of Soot in Premixed Flames", *Seventeenth Symposium (International) on Combustion*, The Combustion Institute, Pittsburgh, pp. 1365-1375 (1979).

43. Wieschnowsky, U., Bockhorn, H. and Fetting, F., "Some New Observations Concerning the Mass Growth of Soot in Premixed Hydrocarbon-Oxygen Flames", *Twenty-Second Symposium (International) on Combustion*, The Combustion Institute, Pittsburgh, pp. 343-352 (1988).

44. Glassman, I., "Soot Formation in Combustion Processes", *Twenty-Second Symposium (International) on Combustion*, The Combustion Institute, Pittsburgh, pp. 295-311, (1988).

45. Flower, W.L. and Bowman, C.T., "Soot Production in Axisymmetric Laminar Diffusion Flames at Pressures from One to Ten Atmospheres", *Twenty-First Symposium (International) on Combustion*, The Combustion Institute, Pittsburgh, pp. 1115-1124 (1986).

46. Davis, R.W., Moore, E.F., Santoro, R.J. and Ness, J.R., "Isolation of Buoyancy Effects in Jet Diffusion Flames", *Combustion Science and Technology*, 73, pp. 625-635 (1990).

47. Schalla, R.L., Clark, T.P. and McDonald, G.E., "Formation and Combustion of Smoke in Laminar Flames", NACA Report 1186 (1954).

48. Bohm, H., Hesse, D., Jander, H., Luers, B., Pietscher, J., Wagner, H.Gg. and Weiss, M., "The Influence of Pressure and Temperature on Soot Formation in Premixed Flames," *Twenty-Second Symposium (International) on Combustion*, The Combustion Institute, Pittsburgh, pp. 403-411 (1988).

49. Kimura, I., "Stability of Laminar-Jet Flames", *Tenth Symposium (International) on Combustion*, The Combustion Institute, Pittsburgh, pp. 1295-1300 (1965).

50. Toong, T.T., Salant, R.F., Topford, J.M. and Anderson, G.Y., "Mechanisms of Combustion Instability", *Tenth Symposium (International) on Combustion*, The Combustion Institute, Pittsburgh, pp. 1301-1313 (1965).

51. Coats, C.M. and Zhao, H., "Transition and Stability of Turbulent Jet Diffusion Flames," *Twenty-Second Symposium (International) on Combustion*, The Combustion Institute, Pittsburgh, pp. 685-692 (1988).

52. Buckmaster, J. and Peters, N., "The Infinite Candle and Its Stability - A Paradigm for Flickering Diffusion Flames", *Twenty-First Symposium (International) on Combustion*, The Combustion Institute, Pittsburgh, pp. 1829-1836 (1986).

53. Lewis, G.S., Cantwell, B.J., Vandsburger, U. and Bowman, C.T., "An Investigation of the Structure of a Laminar Non-Premixed Flame in an Unsteady Vortical Flow", *Twenty-Second Symposium (International) on Combustion*, The Combustion Institute, Pittsburgh, pp. 515-522 (1988).

54. Chen, L.-D., Seaba, J.P., Roquemore, W.M. and Goss, L.P., "Buoyant Diffusion Flames", *Twenty-Second Symposium (International) on Combustion*, The Combustion Institute, Pittsburgh, pp. 677-684 (1988).

55. Ballantyne, A. and Bray, K.N.C., "Investigations into the Structure of Jet Diffusion Flames Using Time-resolved Optical Measurement Techniques", *Sixteenth Symposium (International) on Combustion*, The Combustion Institute, Pittsburgh, pp. 777-787 (1976).

6.0 PUBLICATIONS

1. Santoro, R. J., Yeh, T. T., Horvath, J. J. and Semerjian, H. G., "The Transport and Growth of Soot Particles in Laminar Diffusion Flames," *Combustion Science and Technology*, 53, 89 (1987).

2. Solomon, P. R., Best, P. E., Carangelo, R. M., Markham, J. R., Chien, P., Santoro, R. J. and Semerjian, H. G., "FT-IR Emission/Transmission Spectroscopy for In-Situ Combustion Diagnostics", *Twenty-First Symposium (International) on Combustion*, The Combustion Institute, pp. 1763-1771 (1986).

3. Santoro, R. J. and Miller, J. H., "Soot Particle Formation in Laminar Diffusion Flames", *Langmuir*, 3, pp. 244-254 (1987).

4. Santoro, R. J., "Optical Measurements of Soot Particles in Flames," *Mat. Res. Soc. Symp. Proc.*, Vol. 117, p. 157 (1988).

5. Dobbins, R.A., Santoro, R.J. and Semerjian, H.G., "Analysis of Light Scattering from Soot Using Optical Cross Sections for Aggregates", *Twenty-Third Symposium (International) on Combustion*, The Combustion Institute, Pittsburgh, pp. 1525-1532 (1990).

6. Davis, R.W., Moore, E.F., Santoro, R.J. and Ness, J., "Isolation of Buoyancy Effects in Jet Diffusion Flames", *Combustion Science and Technology*, 73, pp. 625-635 (1990).

7. Santoro, R. J., "Coagulation in Soot Formation in Combustion", An International Round Table Discussion, H. Jander and H.Gg. Wagner (eds), Vandenhoeck and Ruprecht, Gottengen, p. 129 (1990).

8. Santoro, R. J. and Richardson, T. F., "Concentration and Temperature Effects on Soot Formation in Diffusion Flames," accepted for publication by Springer Verlag in *Mechanisms and Models of Soot Formation* (in press).

9. Puri, R., Richardson, T. F., Santoro, R. J. and Dobbins, R. A., "Aerosol Dynamic Processes of Soot Aggregates in a Laminar Ethene Diffusion Flame," submitted to *Combustion and Flame*.

10. Richardson, T. F. and Santoro, R. J., "Soot Formation in Coannular Diffusion Flames: The Effect of Fuel Dilution with Inert Species," submitted to *Combustion Science and Technology*.

7.0 MEETINGS AND PRESENTATIONS

1. "The Effect of Fuel Structure on the Formation and Growth of Soot Particles in Diffusion Flames," The Twenty-Third Biennial Conference on Carbon, Worcester Polytechnic Institute, July 19-24, 1987.

2. "Soot Particle Formation in Diffusion Flames," American Chemical Society Symposium on Advances in Soot Chemistry, ASC Symposium, New Orleans, LA, August 30-September 4, 1987.

3. "Soot Particles Studies as Applied to the Carbon Black Industry," invited seminar Columbia Chemicals Company, Swartz, LA, September 4, 1987.

4. "Fuel Molecular Structure Effects on Soot Particle Growth in Diffusion Flames", Twentieth Fall Technical Meeting of the Eastern Section of the Combustion Institute, Gaithersburg, MD, November 2-5, 1987.

5. "Optical Measurements of Soot Particles in Flames," Materials Research Society Symposia, Reno, Nevada, April 5-8, 1988.

6. "Soot Growth in Diffusion Flames Burning Fuel Mixtures," 1988 Fall Technical Meeting of the Eastern Section of the Combustion Institute, Clearwater Beach, FL, December 5-7, 1988.

7. "Optical Diagnostics for Microgravity Studies in Space," International Microgravity Combustion Workshop, Cleveland, OH, January 25-26, 1989.

8. "Optical Measurements of Soot Particles in Flames," Wright Patterson Air Force Base, Dayton, Ohio, March 6, 1989.

9. Invited Attendee for the Round Table Discussion on "Current Problems in Soot Formation During Combustion," The Commission on Condensation Phenomena of the Academy Science, Gottingen, Germany, March 29 and 30, 1989.

10. Invited Tutorial on Particle Diagnostics, 1989 Annual Meeting of the American Association for Aerosol Research, Reno, Nevada, October 9, 1989.

11. "Surface Growth and Coagulation Processes in Soot Particle Formation," AIChE Annual Meeting, San Francisco, CA, November 6-10, 1989.

12. "Isolation of Buoyancy Effects in Jet Diffusion Flames," presented at the 1990 Central States Section of the Combustion Institute, Cincinnati, OH, May 20-22, 1990.

13. "Two-Dimensional Imaging Techniques for Particle Size Characterization", Twenty-First Annual Meeting of the Fine Particle Society, San Diego, CA, Aug. 21-25, 1990.

14. "An Application of Two-Dimensional Imaging Techniques for Soot and Droplet Studies", 1990 ASME Winter Annual Meeting, The Symposium on Heat and Mass Transfer in Fire and Combustion Systems, Dallas, TX, Nov. 25-30, 1990.

15. "The Effect of Inert Diluent Addition on Diffusion Flame Height in an Oxygen Atmosphere", 1990 Fall Technical Meeting, Eastern Section of the Combustion Institute, Orlando, FL, Dec. 3-5, 1990.

16. "Sonic Probe Sampling in Particle Laden Combustion Flows", 1990 Fall Technical Meeting, Eastern Section of the Combustion Institute, Orlando, FL, Dec. 3-5, 1990.

17. "Concentration and Temperature Effects on Soot Formation in Diffusion Flames," Mechanisms and Models of Soot Formation, an International Workshop, Heidelberg, Germany, September 29-October 2, 1991.

18. Interactive Use of Electron Microscopy and Light Scattering/Extinction Tests in Particle Formation Diagnostics. II. Light Scattering/Extinction Tests," 10th Annual meeting, American Association for Aerosol Research, Traverse City, MI, October 10, 1991.

8.0 PARTICIPATING PROFESSIONALS

Dr. Robert J. Santoro, Professor of Mechanical Engineering
Mr. Rahul Puri, Graduate Student, Department of Mechanical Engineering (Ph.D. expected 9/92, accepted post-doctoral position Yale University)
Mr. Jeff Leet, Graduate Student, Department of Mechanical Engineering (M.S. completed 8/90, presently employed at Southwest Research Institute)
Mr. Thomas Richardson, Graduate Student, Department of Mechanical Engineering (Ph.D. expected 9/92).
Mr. John Ness, Graduate Student (AFRAPT), Department of Mechanical Engineering (M.S. employed at David Taylor Laboratory)
Mr. Darrell Rapp, Graduate Student (AFRAPT), Department of Mechanical Engineering (Ph.D. expected 12/93).
Ms. Yamilla Cancel-Sanchez, Undergraduate Student, Department of Chemical Engineering (B.S. 6/93).
Dr. Wonnam Lee, Research Associate
Mr. Daniel Boone, Technician

9.0 INTERACTIONS

A number of researchers have directly used the extensive data set developed as part of this work to compare with or extend their own research. Some of those who have been directly provided data include:

Professor R. A. Dobbins, Brown University, Providence, RI
Dr. R. Hall, United Technologies Research Center, East Hartford, CT
Dr. R. Davis, The National Institute of Standards and Technology, Gaithersburg, MD
Dr. P. Solomon, Advanced Fuel Research, Inc., East Hartford, CT
Dr. I. Kennedy, University of California, Davis, CA
Drs. C. Merkle and S. Turns, The Pennsylvania State University, University Park, PA
Dr. H. Mongia, Allison Gas Turbine Division-GM, Indianapolis, IN
Dr. K. Smyth, National Institute of Standards and Technology, Gaithersburg, MD

In addition to the interactions resulting from interest in the soot particle data, there have been interactions with researchers on particle diagnostic problems. In some cases this has resulted in direct visits to particular laboratories to assist in solving these problems. These interactions include:

Dr. M. Zachariah, The National Institute of Standards and Technology, Gaithersburg, MD
Dr. Valerie Lyons, NASA-Lewis Research Center, Cleveland, OH

Several other interactions have also occurred through a general interest in the work supported by AFOSR with:

Columbian Chemical Company, Monroe, LA
Cummins Engine Company, Columbus, IN
E. I. DuPont de Nemours, Wilmington, DE
Eastman Kodak, Rochester, NY
Allison Gas Turbine Division
Cummins Engine, Inc., Columbus, IN
Lubrizol, Wickliffe, OH

DuPont is currently supporting work on titanium dioxide particle formation as a direct result of the AFOSR research program. A student, Peter Strakey, has spent two summers with DuPont exchanging expertise and technology developed as part of this research.

Recent work with Allison Gas Turbine Division involving the incorporation of a revised soot model in the gas turbine combustion codes also occurred as a result of the present work. Mr. Darrell Rapp, who is an AFRAPT participant, has spent two summers working at Allison on the implementation of that model. This work is an attempt to directly transfer the results of our work to industry.

We have also participated by invitation in two international workshops on soot formation:

"Current Problems in Soot Formation During Combustion," sponsored by The Commission on Condensation Phenomena of the Academy of Science, held in Gottingen, Germany, March 29-30, 1989.

"Mechanisms and Models of Soot Formation--An International Workshop," sponsored by Volkswagen, Heidelberg, Germany, September 29-October 2, 1991.

APPENDIX 1

Soot Formation in Coannular Diffusion Flames: The Effect of Fuel Dilution with Inert Species

Submitted to *Combustion Science and Technology*

Soot Formation in Coannular Diffusion Flames: The Effect of Fuel Dilution with Inert Species

T. F. Richardson and R.J. Santoro
Department of Mechanical Engineering
The Pennsylvania State University
University Park, PA 16802

April, 1992

Key Words: soot, pollutants, diffusion flame, dilution

Abstract

A detailed study has been made of the relative effects of concentration and temperature on soot formation in diluted laminar ethene/air diffusion flames employing: (1) argon and nitrogen diluted flames at equal calculated adiabatic flame temperatures but different initial concentrations to isolate the effect of concentration and (2) argon and nitrogen diluted flames with equal initial fuel concentrations but different temperatures to isolate the effect of temperature. Total integrated soot volume fraction measurements show that in argon and nitrogen diluted flames with equal calculated adiabatic flame temperatures, the more diluted argon flames consistently display lower soot concentrations. However, in flames of equal dilution, argon flames consistently display higher soot concentrations than the slightly cooler nitrogen diluted flames. Local temperature measurements show that for nitrogen and argon diluted flames with equal calculated adiabatic flame temperatures, argon diluted flames display lower temperatures in the region where soot is first formed. Mass spectrometric measurements of gas species concentrations in diluted and undiluted methane/air diffusion flames were obtained and compared with a numerical flame model. These results show that the initial difference in fuel concentration in diluted and undiluted flames diminishes rapidly with height. Furthermore, laser light scattering measurements show that as inert diluent is added to the flame, soot inception is delayed and consequently less time is available for soot growth. Based on this extensive set of data, a quantitative assessment was made of the relative effects of temperature and concentration indicating that for coflow diffusion flames the role of temperature is more important than the decrease in reaction rate due to the reduction in fuel concentration when an inert diluent is added to the fuel flow.

Introduction

The formation of soot particles in combustion environments involves a complex series of chemical and physical processes which result in the conversion of carbon contained in the fuel to carbonaceous soot particles. A variety of combustion systems have been previously examined to investigate the specific details of the soot formation process. These studies range from simple laboratory premixed and diffusion flames to more practical scale combustion involving, for example, gas turbines, diesel engines and furnaces. Extensive reviews of soot formation phenomena exist summarizing many of these studies [Glassman, 1988; Haynes and Wagner, 1981; Wagner, 1978, 1981]. These previous studies investigated the basic importance of parameters such as pressure, temperature, and fuel molecular structure. An additional parameter of potential importance to which recent attention has been given is fuel concentration.

One means to investigate the effect of fuel concentration is through the introduction of an inert diluent into the fuel stream. Several studies note that the addition of an inert diluent to the fuel reduces soot concentration in laminar diffusion flames [e.g., Deardon and Long, 1968; McLintock, 1968]. This reduction is in part a result of lower flame temperatures achieved in diluted flames as compared to the undiluted case. These lower temperatures reduce the pyrolysis reaction rates leading to decreased soot formation rates and consequently lower soot concentrations [Glassman and Yaccarino,1981]. Reducing the fuel concentration may also have an effect on soot concentration through a proportional reduction in fuel species concentration in the soot formation region, i.e., reaction rates are decreased by lower species concentrations. The objective of the present paper is to examine the effects of changes in temperature and fuel concentration on soot formation when an inert diluent gas is mixed into the fuel stream of a coannular laminar diffusion flame. This study also considers other processes that are influenced by inert dilution.

Although reduction in soot through inert diluent addition has been observed by numerous researchers, only a few studies exist which investigate the relative roles of fuel concentration and flame temperature. Previous studies of laminar diffusion flames have employed dilution as a means to study temperature effects on soot formation [Glassman and Yaccarino, 1981; Santoro and Semerjian, 1984]. In these cases the effects of decreasing fuel concentration were argued to be small relative to the temperature reduction contribution. However, Kent observed that soot concentrations in diluted flames are reduced by an amount that can not be explained by the reduction in flame temperature alone [Kent and Wagner, 1984b]. Kent and Wagner [1984b] concluded that fuel concentration appears to be a significant factor influencing soot production rates. Markstein [1984, 1986] in a series of studies examining the radiative characteristics of laminar diffusion flames also commented on the relative contributions of temperature and concentration effects when diluents are added to the flame [Markstein, 1986]. Axelbaum and et al. addressed this issue quantitatively in a series of experiments in counterflow diffusion flames [Axelbaum et al., 1988a, 1988b]. The important conclusion from these studies is that soot formation rates depend linearly on the initial fuel concentration. Axelbaum and Law recently extended their dilution studies to include coflow diffusion flames [Axelbaum and Law, 1990]. They report a dilution effect for coflow flames that is consistent with the counterflow flame results; that is, the maximum soot volume fraction increases linearly with the fuel concentration at the burner exit. These results imply that when diluents are added to the fuel the role of temperature in soot formation, commonly believed to be the governing parameter of soot formation rates, is in some situations less important than fuel concentration. Recent studies in similar coflow diffusion flames have been reported in which the temperature field is varied through preheating of the fuel and air streams [Gülder and Snelling, 1990; Gülder, 1992]. The results of these studies have been interpreted to support the dominant role of dilution effects on soot formation in these laminar diffusion flame experiments. In the present investigation, the role of

dilution on soot reduction is investigated by making detailed measurements of the critical quantities: soot particle concentration, gas species concentrations and temperature.

Experimental

Investigating the role of temperature and concentration on soot formation in laminar diffusion flames requires careful selection of experimental conditions and measurement approaches. Following a method similar to the approach used by Axelbaum and Law [1990], dilution is studied through a series of flames at identical calculated adiabatic flame temperatures, but which have different initial fuel concentrations. The differences in heat capacities of argon and nitrogen in theory permit comparison of flames with identical temperatures, but different dilutions. Therefore, the effect of concentration is systematically isolated from temperature. Similarly, flame conditions can be selected with identical dilutions, e.g.,(50% N_2 and 50% Ar), but different temperatures, thus isolating the effect of temperature on soot formation. The present study examines both flame diluent conditions. Desired flame temperature conditions are calculated with the NASA Chemical Equilibrium Code [Gordon and McBride, 1976] based on the assumption that the temperatures in the formation region of laminar diffusion flames scale with calculated adiabatic temperatures [Boedeker and Dobbs, 1986a].

A coannular burner operating at atmospheric pressure conditions was used to study laminar diffusion flames burning ethene or methane. A laser scattering/extinction system was used to obtain data on the soot particle field. The burner and light scattering apparatus have been previously described in detail [Santoro et al., 1983] and are only briefly reviewed here. The coannular burner consists of an inner brass fuel tube (1.1 cm id) surrounded by an outer tube (10.0 cm id) for air flow. A 40.5 cm long brass cylinder was used as a chimney to shield the flame from laboratory air currents. Slots 0.476 cm high and 2.54 cm wide were machined in the chimney providing access for the incident, transmitted and scattered light. These slots also allowed access for the thermocouple probe. Two of the slots were modified to provide access for a mass spectrometer sampling probe which required a 1.252 cm circular opening in the chimney. The fuel or fuel inert diluent mixture is burned in a highly over-ventilated air flow, minimizing the effect of air flow rate [Roper et al., 1977a, 1977b]. Fuel flow rates are monitored using calibrated rotameters, while a mass flow meter measured the air flow rates. Fuel gases had a stated purity of 99.0% and 99.5% for methane and ethene respectively. Air was supplied from an in-house compressor which was filtered to remove particles and moisture. Nitrogen and argon were added to the fuel flow using separately calibrated rotameters and had stated purities of 99.99% and 99.995% respectively. The air flow rate for the flames studied was 1062 cm^3/s. Table 1 summarizes the ethene flame flow conditions, which span a range of flow rates, dilutions, and calculated adiabatic flame temperatures.

The laser light scattering/extinction apparatus used a 4W argon ion laser operating at the 514.5 nm laser line. A mechanical chopper operating at 1 kHz modulated the laser source allowing synchronous detection of the transmitted light signals. The laser beam was focused into the burner using a 40 cm focal length lens and was typically operated with an output power of 0.5W. The transmitted light was detected using a silicon photodiode. The transmitted laser light intensity was reduced by a neutral density filter (N.D.=2) to a level suitable for linear photodiode response. The output of this detector was input into a two phase lock-in amplifier which was interfaced to an IBM-XT computer.

Laser light scattering measurements at a scattering angle of 90° with respect to the incident beam could also be obtained with this system. However, in the present experiments such measurements were only used for comparisons with previous studies and to determine the location where soot particles first form.

The entire atmospheric burner was mounted on a three-dimensional translating stage system. Computer controlled stepper motors were used to adjust the vertical and one of the horizontal coordinates. This allowed radial profiles of the laser extinction to be achieved at various axial positions in the flame.

Rapid insertion thermocouple measurements provided measurements of the temperature distributions in the flames studied. The rapid insertion thermocouple technique [Kent and Wagner, 1984a] avoids continuous coating with soot by burning off deposited soot on the thermocouple surface by positioning the thermocouple in the oxidation zone of the flame prior to making measurements at a new location. Pt/Pt-10% Rh fine wire thermocouples were made from 127 μm diameter wire. The resulting bead diameter was 160 μm. A limited number of temperature profiles were also taken with a thermocouple whose junction was made with 63.5 μm wire (95 μm bead diameter) to verify some of the trends. The uncoated thermocouples were mounted on a stepper motor stage for rapid positioning. This technique provides accurate measurement of relative changes in the temperature as diluent species and concentrations were varied.

In order to examine the effect of diluent addition on the local gas species concentrations in the flame, a series of mass spectrometric measurements were obtained. These measurements are similar in approach to previous studies [Smyth et al., 1985]. Coflowing methane/air flames were studied in order to avoid the difficulties introduced by the presence of large soot concentrations which clog the quartz microprobe orifice used in the sampling procedure. The quartz microprobe used in these studies had a 90 μm orifice. This probe was connected to an Extrel model C50 quadropole mass spectrometer. Species mole fraction information from the measurements was obtained using a procedure in which the spectrometer sensitivity to a particular species is measured using a calibration mixture at room temperature. The relative sensitivities are assumed to be independent of temperature allowing calculation of the actual mole fraction by assuming the mole

fraction of measured species sums to unity at each measurement location [Bittner, 1981]. An undiluted methane flame and a 50% diluted methane (with nitrogen) flame were studied. The methane fuel flow rate was 5.70 cm^3/s for both flames with an equal amount of nitrogen added for the diluted case. The air flow rate for these studies was 1062 cm^3/s.

Analysis

In the present study, the quantity of interest is the change in soot volume fraction, f_v, resulting from dilution of the fuel. In previous studies of laminar diffusion flames, tomographic reconstruction approaches have proven useful in providing spatially resolved measurements of f_v from line-of-sight extinction measurements [Santoro et al., 1983]. In the present case, however, errors associated with the tomographic reconstruction approach detract from its usefulness since small relative variations in f_v need to be measured.

An alternate approach is to relate the extinction measurement to an appropriate spatial integral of the soot volume fraction. For soot particles in the Rayleigh size limit ($d<<\lambda$) the extinction (I/I_o) is defined as the ratio of the transmitted laser intensity (I) to incident laser intensity (I_o) , and is related to f_v as:

$$\int_{-\infty}^{\infty} f_v dx = -c(\lambda,m)\ln\left(\frac{I}{I_o}\right) \qquad \text{Eq-1}$$

where x is the direction along which the laser beam propagates, $c(\lambda,m)$ is a constant determined from Rayleigh theory which depends on the wavelength, λ, of the laser and the refractive index , m, of soot particles and x is the path length through the flame. As in previous work, the value of complex index of refraction used is m=1.57-0.56i [Dalzell and Sarofim, 1969]. The constant, $c(\lambda,m)$ calculated from this value is 1.05 x 10^{-5} cm. A measure of the total integrated soot volume fraction, F_v, can be obtained by integrating equation (1) along the direction perpendicular to x. This integrated volume fraction is a measure of the total amount of soot at a particular axial location and is given by

$$F_v = -\int_{-\infty}^{\infty} c(\lambda,m)\ln\left(\frac{I}{I_o}\right)dy \qquad \text{Eq-2}$$

where y is the direction perpendicular to x. The total integrated soot volume fraction, F_v, has been selected because it also incorporates any contributions due to changes in flame diameter as the fuel/diluent flow rate is varied.

Results

The ensuing sections present and discuss the experimental results from the dilution studies. These studies address four aspects of the influence of inert additives on the reduction in soot formation: 1) the relation between fuel species concentration and soot concentration; 2) the relation between temperature and soot formation; 3) the evolution of species concentrations in both diluted and undiluted flames; and 4) variation in soot particle residence time associated with dilution. Using the information from these experiments, the relative influence of fuel concentration and temperature is then considered for coflowing laminar diffusion flames.

Constant Adiabatic Flame Temperature Studies

Temperature Results

The approach used to determine the relationship between the degree of dilution (i.e., fuel concentration) on soot formation involved comparing argon and nitrogen diluted flames having the same calculated adiabatic flame temperature. Since argon and nitrogen have different molar heat capacities, the initial fuel concentration of these flames must be different if the temperature is to be maintained constant. To ensure that the observed differences in soot formation rates in these flames of equal calculated adiabatic flame temperature are a result of differences in fuel concentration and not temperature, the temperature field was determined from rapid insertion thermocouple measurements. In addition, these measurements allow a determination of whether calculated adiabatic flame temperatures may be used to represent the changes in temperature expected with dilution. This may not be self evident since calculated adiabatic flame temperatures are based on the fuel/diluent mixture being supplied to the burner and not the local fuel concentration of the flames.

Thermocouple measurements of the temperature field were obtained in the 4.90 cm^3/s ethene flames (see Table 1) whose calculated adiabatic flame temperatures were 2369K (flame 12), 2346K (flames 5 and 6) and 2333K (flames 7 and 8). The two lower temperature conditions were established individually for nitrogen (flames 5 and 7) and argon (flames 6 and 8) diluent. Radial temperature profiles at several axial locations were obtained for flames 12 and 7 while the other flames were examined only at an axial location 5 mm above the fuel tube exit. Uncorrected measured temperatures at four selected axial locations are shown in Figure 1 for an undiluted and diluted flame (flames 12 and 7). The radial temperature profiles of flames 12 (undiluted) and 8 (diluted), shown in Figure 1 as a function of axial position, reveal a trend expected in the temperature field. For the displayed heights less than 50 mm from the burner exit, temperatures are reduced in the diluted flame. Above 50 mm the ordering of the flames reverses and the diluted flame has a higher temperature. This reversal in temperature is due to more soot being formed in the initially hotter undiluted flame, increasing radiative losses, thus cooling the flame to a greater extent at higher

locations [Kent and Wagner, 1984a, 1984b; Santoro and Semerjian, 1984; Boedeker and Dobbs, 1986a, 1986b].

Careful inspection of the temperature profiles (Figure 1) reveals that low in the flame, dilution reduces temperatures at the centerline to a greater extent than in the annular region [Boedeker and Dobbs, 1986a, 1986b]. This difference in the effect of the diluent as a function of position is related to the diffusional nature of these flames. For both the nitrogen and argon diluent cases as well as the undiluted flame cases, nitrogen from the air stream is diffusing towards the centerline while the "fuel" (diluted or undiluted) diffuses towards the flame front. This interdiffusional aspect of the flame tends to mitigate the initial fuel concentration differences resulting from the addition of the diluent species. This point will be discussed in detail in a subsequent section.

A comparison of the effect of diluent addition on the temperature profiles is further illustrated in Figure 2. For these measurements an axial location 5 mm above the burner exit has been selected. This is near the location where soot is first observed to form in these flames based on light scattering profile measurements. Since soot particles were not observed or exist in very low concentration at this location [Santoro and Semerjian, 1984], radiation effects due to the presence of soot particles are absent and do not complicate the interpretation of measured temperature differences for various flame conditions. Furthermore, by selecting a location close to the fuel tube exit, potential concentration effects introduced by diluting the fuel flow are more likely to be observed.

From the temperature profiles it is observed that in the region near the maximum temperature, low in the flame, the measured temperature differences between the undiluted and diluted flames are similar to the differences in calculated adiabatic flame temperature (see Figure 2, insert). Similar results using CARS temperature measurements were obtained by Boedeker and Dobbs [1986a, 1986b]. Furthermore, temperatures observed in flames in which diluent conditions are chosen to result in the same calculated adiabatic flame temperature differ by less than 10K in the region near the temperature maximum. However, as the centerline is approached from the temperature maximum, differences between the N_2 and Ar diluted flames for identical calculated adiabatic flame conditions increase with the N_2 diluted flames having slightly higher temperatures. Near the radial location (r=5 mm) where soot is formed [Santoro and Semerjian, 1984; Santoro et al., 1983], this difference can be as large as 33-56K (see Table 2). Positioning uncertainty with respect to the thermocouple measurement location is not believed to be the source for these observed differences, since both the centerline minimum and the symmetric temperature maximums in the annular region show good positional agreement for each of the flames (see Figure 2). These observed differences are likely due to the differences in the thermal transport properties in the individual flames. Since the thermocouple measurements are also influenced by local thermal transport phenomena, differences in the observed temperatures could be a result of this systematic

variation. To investigate this possibility, an estimate of the effect of the difference in the transport properties between argon and nitrogen on the thermocouple measurements was made [Bradley and Mathews, 1968]. This estimate indicated that at most one third of the measured temperature difference was due to variation in transport properties. Furthermore, the thermocouple measurements were repeated for the 5 mm axial location using a smaller bead (95 μm) thermocouple. These measurement showed very similar temperature differences as compared with the larger bead thermocouple (160 μm) measurements. Since variations in the bead diameter result in significant differences in the heat transfer and radiative processes involving the thermocouple bead, the insensitivity of the measured temperature differences to variations in the bead size suggests that the measured differences are indeed representative of actual temperature differences in the flame.

The temperature measurement results comparing the argon and nitrogen diluted cases at the 5 mm axial location for several flames are summarized in Table 2. Listed in this table are the calculated adiabatic flame temperature (T_{AD}), the maximum temperature observed (T_{MAX}, uncorrected for radiative effects), and the difference in the temperature ($\Delta T_{R=5\ mm}$) observed at the 5 mm radial position between the N_2 diluted and Ar diluted flames which is near where soot is first observed.

The following observations can be made based on the results shown in Table 2. Flames with similar calculated adiabatic flame temperatures achieve similar measured maximum temperatures. For the nitrogen and argon flames with similar calculated temperatures, the observed temperature difference between flames increases with dilution in the interior region of the flame (i.e. r= 5 mm and ΔT). Thus, although dilution with differing diluents can be used to achieve similar maximum temperature conditions, measurable differences in the temperature field will result in regions interior to the maximum temperature region. These observations underscore the need to consider the local temperature and concentration as well as the overall expected behavior of the flame in assessing the effects of dilution.

Soot Formation Results

To investigate the variation in soot formation rate with the initial fuel concentration, the soot yield in flames of similar temperatures but different dilutions were undertaken using three pairs of flames, each pair at a different temperature. The variation in the total integrated soot volume fraction, F_v, at various axial locations is shown in Figure 3 for each of the ethene flames with a flow rate of 4.90 cm^3/s. It is interesting to note that, although addition of diluent increases the burner exit velocities, the height at which the peak volume fraction is reached is nearly constant in these flames with possibly the exception of flame 4 which has the highest dilution. The height at which the soot maximum is reached is determined by the location where the oxidizer replaces the fuel at the centerline [Roper, 1977a, 1977b]. Thus, the rate of diffusion of oxidizer into the flame front is only weakly dependent on the amount of fuel dilution.

The maximum F_v is used as a readily determined measure of the sooting propensity of these flames. The reduction in soot formed is calculated as the ratio of the maximum F_v in the diluted and undiluted flames (see Table 1). In this comparison, the reduction in soot may be due to temperature and/or concentration effects. As expected, the maximum soot concentration ratios show that reducing fuel concentration and temperature reduces the amount of soot formed. The flames which show the largest relative reduction in soot (flames 3 and 4), the most diluted flames, show a dependence on the soot formation rate which is directly proportional to the initial fuel concentration. This implies soot formation rates vary with initial fuel concentration in less than a first order dependence, since a temperature reduction effect on soot formation has not been taken into account.

Of course the motivation for establishing flames with the same temperature field but different fuel concentration is to presumably isolate concentration effects from temperature effects. The following discussion therefore emphasizes comparisons between diluted flames having identical calculated adiabatic flame temperatures. Under these conditions the peak soot concentrations are observed to decrease to a greater extent for the more heavily diluted argon flames. This result is similar to previous observations and is argued to be a measure of the dilution effect [Axelbaum and Law, 1990]. In order to quantify the effects of fuel concentration on soot formation rates, the maximum F_v was taken to be related to the initial mole fraction by:

$$F_v \propto \left[X_{F_0}\right]^b \qquad \text{Eq-3.}$$

Based on the ratio of the maximum F_v values and the known initial concentrations, a value for b can be obtained for flames with equal calculated adiabatic flame temperatures. The results of these calculations are shown in Table 3 for several flames. As can be seen no unique value of b results and a first order dependence does not appear to be generally valid. It should be mentioned that relatively small changes in F_v are involved in some of the results and thus the accuracy in b may not be high.

The above results indicate that the concentration effect of soot formation may not be first order in the initial fuel mole fraction. Furthermore, for flames with the different diluents but equal calculated adiabatic flame temperature, measurements indicate that differences in temperature exist in the region in which soot inception occurs. The potential significance of these temperature differences will be addressed in the discussion section.

Constant Concentration Studies

As a complement to the studies at constant temperature, a series of flames was also studied in which the initial concentration of the fuel was held constant and the temperature was varied. In this approach the variation of soot concentration due to temperature differences in pairs of ethene flames equally diluted with nitrogen or argon were measured. For these constant concentration studies, the

argon flames have higher calculated adiabatic flame temperatures (see Table 1). Since argon and nitrogen diffuse in a similar manner, these flames should have similar concentration fields. Three pairs of flames (Flames 1 and 1a, Flames 3 and 3a, and Flames 6 and 7) were compared with fuel mole fractions of 0.5, 0.5 and 0.64 respectively.

Temperature profile measurements at an axial location 5 mm above the fuel tube exit show the maximum temperatures in the flames differed by 16-25K in agreement with adiabatic flame temperature calculations. In addition, centerline temperatures were found to be 10-22K larger for the argon diluted flames. Any meaningful assessment of the temperature differences between these two locations was not possible since the argon profiles were observed to extend to a slightly larger radial coordinate.

Measurements of the soot concentrations of these flames with the same dilution show that the nitrogen flames with lower calculated adiabatic flame temperature produce less soot (Figure 4). Thus, reducing temperature clearly reduces the production of soot. In conjunction with the constant temperature studies, these results can be used to assess the relative contributions of temperature and concentration on the soot formation process in these diluted flames.

Concentration Measurement Results

In any chemically reacting system the reaction rates must clearly be sensitive to the concentration of the reactants. In studies where the initial fuel concentration is varied through dilution, the occurrence of concentration effects on the soot formation process appears to be self evident. However, such concentration effects should be related to the local concentration in the region where soot formation and growth occur. Thus, it is important to understand the manner in which variations in the initial fuel concentration affect species concentration at other locations in the flame. For this reason a series of mass spectrometric profiles were obtained in an undiluted methane flame and a methane flame in which the fuel was diluted to 50% with nitrogen. The objective of these studies was to quantify specifically the variation in local species concentration as the initial fuel concentration was changed. Methane/air flames were studied in order to avoid probe plugging problems associated with regions of high soot concentration typical of ethene diffusion flames.

Radial mole fraction profiles of major species (CH_4, N_2, O_2, CO_2, CO, H_2O, and H_2) were obtained at axial positions of 5 and 12 mm. The results for CH_4, N_2, O_2, CO_2 at 12 mm were compared with gas chromatography analysis and showed agreement to better than 10%. Figures 5 and 6 show the radial concentration profile results for both flame conditions at an axial location of 12 mm. As is clear from these results, the initial difference in the fuel concentration rapidly narrows as diffusion of fuel and nitrogen, as well as combustion products, proceeds. Comparisons of the measured concentrations for both flames have been made at the centerline and at a radial position of

5 mm. The 5 mm radial position is again taken to be characteristic of the soot precursor region. For the 5 mm axial location, the ratio of the measured concentrations in the diluted and undiluted methane flames are 0.71 and 0.69 for the 5 mm radial location and centerline (r =0.0 mm) respectively. At the 12 mm axial location, the values for the same two radial locations are 0.96 and 0.92 respectively. The values depart markedly from 0.5, the ratio which represents the initial concentration ratio at the fuel tube exit for the diluted and undiluted flame cases. The rapid interdiffusion of nitrogen from the air stream and fuel has previously been noted by Boedeker and Dobbs [1986b]. It should also be mentioned that the temperature as well as the fuel concentration is varied in these two methane/air diffusion flame cases. However the temperature differences are not large enough to significantly affect the diffusion rates. A clear observation from these results is that variations in the local fuel concentration introduced through dilution differ significantly from those at the fuel tube exit.

Residence Time Results

Residence time effects have been shown to be important in diffusion flame studies of soot formation [Santoro et al., 1987; Honnery and Kent, 1990]. In fact, the mass flow rate of soot in laminar diffusion flames has been observed to have a squared or cubed power dependence on residence time [Honnery and Kent, 1990]. Thus, changes in velocity which result from addition of diluent species could affect the residence time and the ultimate soot volume fraction achieved as a result. However the present measurements in these buoyancy dominated diffusion flames indicate that the major observed effect of dilution with respect to residence time is a shift of the location where soot is formed to higher axial positions. Since the location of the maximum soot volume fraction is largely unaffected by dilution (see Figure 3), the total soot residence time is reduced. A reduction in residence time under diluted flame conditions may account for a significant reduction in soot volume fraction and should be accounted for separately in studies where the effects of temperature and concentration are studied. To determine the location where soot particles first form, the scattered light intensity at a scattering angle of 90° was measured in the lower region of flames 1, 2, 9, 10, 11, and 13 of this study. Additional light scattering measurements were taken for 3.85 cm^3/s C_2H_4 flame diluted with 8.82 cm^3/s of N_2 (experiment no. 7 of Santoro and Semerjian [1984]). These results, which are shown in Figure 7 indicate that once soot particles are present the maximum scattered light intensity at a given axial location increases rapidly with height above the burner. Furthermore, this figure clearly shows that as the flames are diluted with inert gas, inception is delayed, and less time for soot growth is possible. Note that the shift in the location of the initial soot formation region could be a result of temperature, velocity and/or concentration effects.

Discussion

From the above results, it is clear that studies which utilize dilution of the fuel flow to vary temperature and concentration parameters, are difficult to unambiguously interpret in terms of global effects. Mixing and transport processes have been shown in this work to locally alter the global dilution effects of temperature and concentration. In order to understand the relative effects of temperature and concentration variations on soot formation processes, it is important to account for these local effects.

There are two major observations based on the present work regarding local temperature and concentration effects when diluents are added to the fuel flow in laminar diffusion flames. The first involves the case when different diluents (e.g., N_2 and Ar) are used to achieve constant temperature conditions, but varying concentration conditions in the flame. The present work indicates that although nearly equal maximum temperatures are achieved, interior to the flame front in the region where soot particles are initially formed, temperature differences of 33-56 K are observed. The second observation is that mixing effects due to interdiffusion of species, such as nitrogen from the air flow and combustion products from the reaction zone, mitigate the effects of dilution rapidly in these flames. Thus, the ratio of the local concentration between flames of varying fuel dilution can differ significantly from initial concentration ratio at the fuel tube exit. These observations imply a more complicated interaction between temperature and concentration effects when fuel dilution is used to study soot formation than was anticipated in some previous work [e.g. Santoro and Semerjian, 1984].

In the discussion below, supporting evidence for the importance of the observations described above will be given. This will be followed by an analysis which is intended to estimate the relative importance of the contributions of temperature and concentration effects on soot formation when fuel dilution is used as a means to alter the soot formation characteristics of the flame. The later topic is of interest because of the present diversity of results in the literature regarding this matter [Glassman and Yaccarino, 1981; Santoro and Semerjian, 1984; Axelbaum and Law, 1990; Gülder and Snelling, 1990; Gülder, 1992].

It has been previously mentioned that the present studies indicate that small temperature differences are observed near the soot formation region for diluted flame conditions of equal calculated adiabatic flame temperatures. It is appropriate, therefore, to inquire as to the potential significance of such small temperature variations (ΔT=33-56 K) on the soot formation process.

Results from previous work by Kent and Wagner [1984b] for laminar diffusion flames and Böhm et al. [1988] for premixed flames indicate that relatively small changes in temperature have a significant affect on the amount of soot produced. Kent and Wagner [1984b] investigated the effect of fuel tube lip conditions on the production of soot by replacing their water cooled fuel tip with an

uncooled glass tip while holding all other conditions constant. They found for fuel flow rates comparable to the present study that the maximum soot volume fraction increased by approximately 20% for the glass fuel tip. Accompanying temperature measurements made 5 mm above the lip of the fuel tube showed very small differences for the two fuel tube configurations [Kent and Wagner, 1984b]. These results indicate that the soot particle formation process is quite sensitive to temperature changes in the region of the flame near the fuel tube exit.

Studies by Böhm et al. [1988] in premixed flames show for ethene/air flames that changes in the measured temperature of 50 K can result in approximately a factor of two change in the soot volume fraction, $f_{v\infty}$, for temperatures between 1550 K and 1625 K. Further increasing the temperature results in $f_{v\infty}$ reaching a maximum at about 1675 K and then decreasing for higher temperatures. These same trends were observed for a range of C/O ratios between 0.6 and 0.8 which correspond to an equivalence ratio between 1.8 and 2.4 for ethene burning in air. This range of temperatures is similar to the range for which soot particles are observed to form in laminar diffusion flames. An interesting result of these experiments is that the observed temperature sensitivity of $f_{v\infty}$ varies, being larger for temperatures below 1600 K than for temperatures between 1600 K and 1675 K. Above 1675 K, $f_{v\infty}$ decreases as temperature is further increased. Thus, the Böhm et al. [1988] results clearly show that the temperature sensitivity observed for the soot formation process will depend on the temperature region studied. In the present studies we argue that the temperature lies in the range between 1350 K and 1625 K (see Figure 2, r=5 mm) where significant temperature sensitivity is observed [Böhm et al., 1988]. If temperatures were raised above 1650 K by some means, one would expect a less significant temperature sensitivity or possibly a decrease in the amount of soot formed if temperatures above 1675 are achieved. It should also be noted that the above observations are for ethene flames. Other fuels are observed to have different temperature sensitivities [Böhm et al., 1988; Frenklach et al., 1983] and care must be exercised in generalizing results obtained over a specific temperature range to all hydrocarbon fuels. The critical point for the present study is that significant temperature sensitivity has been observed for the soot volume fraction for temperature changes of 50 K in ethene flames. Thus, the observed temperature variations between the nitrogen and argon diluted flames in the interior regions where soot is formed is potentially important in terms of changes in the observed soot volume fraction.

The second observation involves the effect of diffusion on the evolution of the fuel concentration field when diluent is added to the fuel flow. The previously presented results show that diffusion processes diminish the effects of diluting the fuel at locations downstream of the fuel tube exit. This is particularly true for the region where soot particles are first observed to form. In order to further investigate the generality of these observations a numerical modeling study was conducted and compared to the mass spectrometric measurements of species concentrations in the methane/air diffusion flame described earlier.

A generalized flame sheet model for laminar diffusion flames developed by Mitchell and coworkers [Mitchell et al., 1980] was used to investigate the variation of fuel concentration as a function of position in the flame. The calculations shown in Figure 8 were carried out for undiluted and 50% nitrogen diluted ethene/air flames at fuel flow rates of 2.75 and 6.58 cm^3/s. The lower fuel flow rate conditions correspond to flames 11 and 1. This figure plots the calculated fuel mole fraction as a function of height along the flame center line. In each case, undiluted or diluted, the fuel mole fractions reach similar values at axial locations between 10 to 30 mm above the burner exit depending on the fuel flow rate. These results are further examined in Figure 9 where radial profiles are presented for Flames 11 and 1 at three axial locations (0.3 mm, 2.7 mm and 14.5 mm). Additionally, Table 4 shows results tabulated for other fuel flow rates at specific axial locations for selected radial positions (4.63 mm and the center line). Comparisons shown in Table 4 and in Figure 9 indicate that in the region where soot is first formed, the local fuel concentration ratio between the diluted and undiluted flame is typically between 0.72 and 0.88. Additionally, the effect of dilution is slightly more pronounced for the lower volumetric fuel flow rate case. For example, at z = 2.7 mm and R = 4.63 mm, the concentration ratio is 0.76 for the 2.75 cm^3/s case as compared to 0.85 for the 6.58 cm^3/s flame. Thus, these modeling results show that in the region where soot is first formed, the ratio of the fuel concentration in the diluted and undiluted flames achieves similar values to those based on mass spectrometric measurements in the methane flames previously presented. The experimental data shows a similar diminishing effect of the initial fuel dilution as predicted using the flame code. This effect is a result of the rapid interdiffusion of nitrogen from the air with the fuel, mitigating the initial dilution. Consequently, all laminar diffusion flames burning in air undergo "dilution" by nitrogen, rapidly reducing the local fuel concentration [see also Boedeker and Dobbs, 1986a, 1986b]. From these results, one can conclude that the local concentration of fuel and combustion products will quickly achieve similar values in both diluted and undiluted flames. Furthermore, concentration effects, based on initial values at the fuel tube exit, will not reflect the true concentration effects in the soot formation region.

An additional aspect of the soot formation process observed to be affected by dilution is the change in time available for soot growth or the soot residence time. Figure 7 which shows the maximum scattered light intensity at selected axial positions, clearly indicates that soot inception is delayed with increased dilution of the fuel flow. To calculate the soot residence time a buoyancy driven acceleration of 3100 cm/s^2 is used [Flower, 1989; Santoro et al.,1987]. The soot residence time is then calculated assuming a flow with constant acceleration and an initial velocity determined by the flow conditions at the fuel tube exit. For the diluted ethene flames in this study, a decrease in soot residence time was estimated to account for between 2% and 15% of the reduction in F_v from the undiluted flames, assuming the soot volume fraction increases linearly with time, with the largest reductions corresponding to the 6.58 cm^3/s ethene flames. In more dilute flames such as the

nitrogen diluted ethene flame of Santoro and Semerjian [1984] (see Figure 7), the decrease in residence time is observed to be more significant, accounting for 27% of the reduction in soot again assuming a linear relation between F_v and time.

Although the reduction in soot particle residence time with increased dilution may be a temperature or a concentration effect, two observations exist which suggest that the decrease in residence time is due to a reduction in temperature. First, the height at which soot inception occurs, as defined by a rapid increase in scattered light intensity, is nearly the same for flames with equal calculated adiabatic flame temperature indicating that the soot particle inception location is more strongly influenced by temperature (see Figure 7). Additional temperature measurements are needed to fully confirm this effect. Second, soot is observed to form at slightly larger (Δr=0.25 mm) radial coordinates for the more dilute flames. Larger radial coordinates correspond to higher temperatures and lower fuel concentrations. Thus, an increase in temperature is a physically more satisfying explanation for the radial shift in the soot particle inception location.

A more quantitative assessment of the effects of temperature and fuel concentration can be made based upon the dilution experiments previously discussed. To separate the temperature and concentration effects on soot formation, a functional form for soot growth is assumed. The functional dependence on temperature and concentration is taken to be similar to the form used by Axelbaum et al. [1988]

$$\frac{dF_v}{dt} \propto [X_{F_o}]^{\alpha} e^{-E_a/RT_{AD}} \qquad \text{Eq-4.}$$

where α is the apparent order of the soot growth rate with respect to the initial fuel mole fraction and E_a is the apparent activation energy. In the present analysis, the dependence on initial fuel concentration, X_{FO}, is not taken to be first order, rather α is estimated from a fit to the experimental data.

Several cautionary remarks need to be made about the use of such an expression. Soot formation in diluted diffusion flames is affected by a series of complex interactions due to diffusional mixing, temperature field variations, and soot formation chemistry. Furthermore, the local soot volume fraction within the flames is a result of soot inception and subsequent surface growth which are described by two different temperature sensitivities, i.e. apparent activation energies [Vandsburger et al., 1984]. In addition, temperature measurements in this study have shown that even under equal calculated adiabatic flame temperature conditions, differences in temperature in argon and nitrogen diluted flames occur in the region where soot is first formed. Clearly such a simple expression does not incorporate enough of the physical details of these processes to make general use of this relationship to describe soot growth in diffusion flames justified. Instead, the deduced values for α and E_a represent purely empirical values based on a correlation to the ethene

flames in this study. These results are then used to assess the relative importance of temperature and concentration effects in the present study, which can be extended to studies under similar conditions.

To evaluate equation 4 for values of α and E_a , the time rate of change of the total soot volume fraction is needed. The calculation of the time coordinate is carried out in the same manner described for the calculation of soot particle residence time. The slope of a linear least squares fit of the F_V vs. time data in the soot growth region was taken to represent dF_V/dt. Temperature values are the calculated adiabatic flame values and X_{FO} is the fuel mole fraction at the fuel tube exit. Using a nonlinear least squares curve fitting procedure applied to the results of the twelve diluted ethene flame conditions listed in Table 1, values of α and E_a were determined to be 0.30±0.18 and 94.5±25.5 kcal/mole, respectively. It should be noted that the use of calculated adiabatic temperatures results in apparently large activation energies. For example, if an apparent activation energy was determined from the premixed flame results of Böhm et al. [1988] based on the variation of $f_{v\infty}$ over the measured temperature region of 1550 K and 1600 K, one calculates a value of 68 kcal/mole. If instead the calculated adiabatic temperature of 2369 K is used with a ΔT of 50 K as appropriate to an undiluted and diluted ethene/air diffusion flame, a value of 150 kcal/mole results. Similarly, Vandsburger et al. [1984] reported the apparent activation energy for the overall soot growth rate for an ethene counterflow diffusion flame as 41 kcal/mole. However, because actual measured temperatures in the range 1270-1480 K were used, an assessment of the apparent activation energy using the higher calculated adiabatic flame temperatures would result in a significantly larger value of the apparent activation energy. Thus, interpretation of the physical meaning of this activation energy needs to be done with care. Essentially for the present purposes E_a represents a measure of the temperature sensitivity of the soot formation process as observed in these studies and has no further fundamental chemical kinetic significance.

The relative effects of concentration and temperature can be deduced from this expression by making comparisons between an undiluted and diluted flame. For example, the reduction in the fuel concentration term comparing an ethene flame diluted with 50% nitrogen to its undiluted counterpart is 0.81 ($=(0.5/1.0)^{0.30}$) while the corresponding reduction in the exponential temperature term for temperatures of 2310 K and 2369 K is 0.60. The ratio of the reduction in soot concentration due to temperature effects to the reduction due to concentration effects (1-0.60)/(1-0.81), indicates a temperature effect which is 2.1 times more important. It should be noted that this estimate is believed to be a lower limit on the temperature dependence since other factors which would likely increase the temperature dependence were not included in the analysis. Specifically, thermocouple measurements in flames which have equal calculated flame temperature show that in the region where soot is being formed, the argon diluted flames actually have lower temperatures. Also, neglecting changes in residence time, which appears to be more strongly influenced by temperature than concentration, would likely lead to an underestimation of the temperature effect.

A second assessment of the dependence on temperature can be made by direct comparison of the soot formation rate in pairs of flames with equal concentration. In this comparison, the parameter α need not be evaluated. The activation energy, E_a, was found to be 235, 105, and 97 kcal/mole for flame pairs 1 and 1a, 3 and 3a, and 6 and 7 respectively. The larger temperature dependence displayed for the 2.75 cm^3/s flames (1 and 1a) may indicate a more complex relation between fuel flow rate and the dependence of soot formation rate on temperature than indicated by Equation 4. One should be aware that since these values are based on comparison between only two flames they are subject to considerable uncertainty. However, in each case these values indicate a dominant temperature effect. These results can, therefore, be viewed as indicating an upper limit on the temperature sensitivity of the soot formation process in fuel dilution studies.

The relative effects of concentration and temperature on the soot formation rate are shown graphically in Figure 10. In this representation, the measured soot formation rate for diluted flames normalized by their undiluted counterparts is shown with the corresponding ratio of the exponential temperature term in Equation 4 for the diluted flames and their undiluted counterparts. The exponential temperature dependence is shown for apparent activation energies, E_a, of 40, 95, and 150 kcal/mole for the calculated adiabatic flame temperature of each of the ethene flames in this study. The dashed line represents a slope of unity, or the total reduction in the soot formation rate by both temperature and concentration. For a given apparent activation energy, the reduction in soot formation rate due to temperature reduction is the difference between the exponential temperature dependence (the solid line) from unity. The contribution of concentration to the reduction in soot formation rate with dilution is then given by the difference between the solid line and the dashed line. For example, for an activation energy of 40 kcal/mole, concentration is nearly twice as important as temperature in reducing soot formation in diluted flames. Figure 10 also shows that an activation energy of 150 kcal/mole represents an upper limit, since the calculated reduction in soot formation rate due to temperature fully accounts for the measured reduction in the soot formation rate. The present results argue for an apparent activation energy closer to 95 kcal/mole to represent the temperature sensitivity of the soot formation process in these diluted ethene flames. However, this single value can not be rigorously justified for all flames conditions as the above reported variation in E_a attests. The present results, however, do indicate that under conditions where diluents are added to the fuel flow, the temperature effect is more important than the concentration effect.

Any attempt to further quantitatively narrow the estimate of the temperature sensitivity of the soot formation process in terms of an activation energy is complicated by the nature of the dilution experiments. Dilution of the fuel results in only small changes in temperature and, as shown in this work, the local fuel concentration. Thus, highly accurate measurements of the changes in soot particle concentration, temperature, and gas species concentration are required. This observation highlights the difficulty in studying concentration and temperature effects through a fuel dilution

approach where, based on the current results, coupled interactions involving thermal and mass transport are seen to be important. The complexity of this flame environment may contribute to the variety of interpretations regarding the effects of inert dilution on soot reduction.

Conclusions

Measurements of the decrease in soot volume fraction at various dilutions have shown that soot is reduced considerably as both the adiabatic flame temperature and initial fuel concentration are simultaneously decreased. Both temperature reduction and fuel concentration reduction were considered as likely explanations for the reduction in the soot formation rate. An examination of the decrease in the soot formation rate in flames with equal fuel concentration, but different degrees of initial dilution, show that the more heavily diluted argon flames produce less soot than the nitrogen diluted flames. Rapid insertion thermocouple measurements made in these flames near the region where soot first forms show that the argon diluted flames display lower temperatures than their nitrogen diluted counterparts. This point attests to the need for local measurements when trying to quantitatively deduce temperature and concentration effects in diffusion flames. The use of adiabatic temperatures to quantify small changes in temperature due to dilution appears to underestimate the effect of temperature when comparing soot formation rates in argon and nitrogen diluted flames with the same calculated adiabatic flame temperatures.

The results from this study suggest that the role of temperature on the soot reduction process exceeds the reduction due to a decrease in fuel concentration. These results are consistent with the measured and calculated effect of dilution on the local fuel concentration; that is, in the coannular geometry, the local fuel concentration quickly approaches a similar value regardless of the initial dilution conditions. In fact, in the region where soot is first formed, diffusion greatly reduces the fuel concentration ratio when comparing diluted flames to undiluted flames as compared to the initial fuel tube exit conditions. A comparison of argon and nitrogen diluted ethene flames at equal dilution and different calculated adiabatic flame temperatures shows that temperature significantly alters the soot formation rates. One difficulty in accessing the relative contribution of temperature is that very small changes in temperature need to be measured accurately. In addition, dilution experiments offer only a narrow range over which temperature can be modified and the resulting changes in temperature and concentration are observed to be small. Although the present analysis does not lead to a singular assessment of the relative effect of concentration and temperature on soot formation rates in diluted flames (one may not expect this as these effects may be functions of fuel flow rate, fuel etc. for these diffusion flames), these results support a temperature effect which is more important than the fuel concentration effect on the soot reduction associated with inert dilution to the fuel flow in coannular laminar diffusion flames.

Acknowledgment

This material is based upon work supported by the Air Force Office of Scientific Research under Award No. AFOSR-87-0145, Dr. Julian M. Tishkoff, program manager. Useful discussions with R. L. Axelbaum, R. A. Dobbins, I. Glassman and S. Harris are also gratefully acknowledged.

References

Axelbaum, R. L., Flower, W. L. and Law, C. K. (1988a). Dilution and Temperature Effects of Inert Addition on Soot Formation in Counterflow Diffusion Flames. *Combust. Sci. and Tech.* **61**, 51.

Axelbaum, R. L., Law, C. K. and Flower, W. L. (1988b). Preferential Diffusion and Concentration Modification in Sooting Counterflow Diffusion Flames. *Twenty-Second Symposium (International) on Combustion*, The Combustion Institute, p. 379.

Axelbaum, R. L. and Law, C. K. (1990). Soot Formation and Inert Addition in Diffusion Flames *Twenty-Third Symposium (International) on Combustion*, The Combustion Institute, p. 1517.

Bittner, J. D. (1981). A Molecular Beam Mass Spectrometer Study of Fuel-Rich and Sooting Benzene-Oxygen Flames. Ph.D. Dissertation, Massachusetts Institute of Technology.

Boedeker, L. R. and Dobbs, G. M. (1986a). CARS Temperature Measurements in Sooting, Laminar Diffusion Flames. *Combust. Sci. and Tech.* **46**, 301.

Boedeker, L. R. and Dobbs, G. M. (1986b). Soot Distribution and Cars Temperature Measurements in Axisymmetric Laminar Diffusion Flames With Several Fuels. *Twenty-First Symposium (International) on Combustion*, The Combustion Institute, p. 1097.

Böhm, H., Hesse, D., Jander, H., Lüers, B., Pietcher, J., Wagner, H. Gg. and Weiss, M. (1988). The Influence of Pressure and Temperature on Soot Formation in Premixed Flames. *Twenty-Second Symposium (International) on Combustion*, The Combustion Institute, p. 403.

Bradley, D. and Mathews, K. J. (1968). Measurement of High Gas Temperatures With Fine Wire Thermocouples. *J. of Mech. Eng. Sci.* **10**, 299.

Dalzell, W. H. and Sarofim, A. F. (1969). Optical Constants of Soot and Their Application to Heat-Flux Calculations. *ASME J. of Heat Transfer* **91**, 100.

Deardon, P. and Long, R. (1968). Soot Formation in Ethylene and Propane Diffusion Flames. *J. Appl. Chem.* **18**, 243.

Flower, W. L. (1989). Soot Particle Temperatures in Axisymmetric Laminar Ethylene-Air Diffusion Flames at Pressures up to 0.7 MPa. *Combust. and Flame* **77**, 279.

Frenklach, M., Taki, S., Durgaprasad, M. B. and Matula, R. A. (1983). Soot Formation in Shock Tube-Pyrolysis of Acetylene, Allene, and 1,3-Butadiene. *Combust. and Flame* **54**, 81.

Glassman, I. and Yaccarino, P. (1981). The Temperature Effect in Sooting Diffusion Flames. *Eighteenth Symposium (International) on Combustion*, The Combustion Institute, p. 1175.

Glassman, I. (1988). Soot Formation in Combustion Processes. *Twenty-Second Symposium (International) on Combustion*, The Combustion Institute, p. 295.

Gordon, S. and McBride, B. J. (1976). Computer Program for Calculation of Complex Chemical Equilibrium Compositions, Rocket Performance, Incident and Reflected Shocks, and Chapman Jouguet Detonations. NASA SP-273, Interim Revision N278-17724.

Gülder, O. L. and Snelling, D. R. (1990). Formation and Temperature of Soot Particles in Laminar Diffusion Flames with Elevated Temperatures. *Twenty-Third Symposium (International) on Combustion*, The Combustion Institute, p. 1509.

Gülder, O. L. (1992). Soot Formation in Laminar Diffusion Flames at Elevated Temperatures. *Combust. and Flame* **88**, 74.

Haynes, B. S. and Wagner, H. Gg. (1981). Soot Formation. *Prog. Energy Combust. Sci.* 7, 229.

Honnery, D. R. and Kent J. H. (1990). Soot Formation in Long Ethylene Diffusion Flames. *Combust. and Flame* **82**, 426.

Kent, J. H. and Honnery, D. R. (1991). Soot Formation Rates in Diffusion Flames-A Unifying Trend. *Combust. Sci. and Tech.* **75**, 167.

Kent, J. H. and Wagner, H. Gg. (1984a). Temperature and Fuel Effects in Sooting Diffusion Flames. *Twentieth Symposium (International) on Combustion*, The Combustion Institute, p. 1007.

Kent, J. H. and Wagner, H. Gg. (1984b). Why Do Diffusion Flames Emit Smoke? *Combust. Sci. and Tech.* **41**, 245.

Markstein, G. H. (1984). Relationship Between Smoke Point and Radiant Emission From Buoyant Turbulent and Laminar Diffusion Flames. *Twentieth Symposium (International) on Combustion*, The Combustion Institute, p. 1055.

Markstein, G. H. (1986). Radiant Emission and Smoke Points for Laminar Diffusion Flames of Fuel Mixtures. *Twenty-First Symposium (International) on Combustion*, p. 1107.

McLintock, I. S., (1968). The Effect of Various Diluents on Soot Production in Laminar Ethylene Diffusion Flames. *Combust. and Flame* **12**, 217.

Mitchell, R. E., Sarofim, A. F. and Clomburg, L. A. (1980). Experimental and Numerical Investigation of Confined Laminar Diffusion Flames. *Combust. and Flame* **37**, 237.

Roper, F. G. (1977a). The Prediction of Laminar Jet Diffusion Flame Sizes: Part I. Theoretical Model. *Combust. and Flame* **29**, 219.

Roper, F. G., Smith, C. and Cunningham, A. C. (1977b). The Prediction of Laminar Jet Diffusion Flame Sizes: Part II. Experimental Verification. *Combust. and Flame* **29**, 227.

Santoro, R. J., Semerjian, H. G. and Dobbins, R. A. (1983). Soot Particle Measurements in Diffusion Flames. *Combust. and Flame* **51**, 203.

Santoro, R. J. and Semerjian, H. G. (1984). Soot Formation in Diffusion Flames: Flow Rate, Fuel Species, and Temperature Effects. *Twentieth Symposium (International) on Combustion*, The Combustion Institute, p. 997.

Santoro, R. J., Yeh, T. T., Horvath, J. J. and Semerijian, H. G. (1987). The Transport and Growth of Soot Particles in Laminar Diffusion Flames. *Combust. Sci. and Tech.* **53**, 89.

Smyth, K. C., Miller, J. H., Dorfman, R. C., Mallard, W. G. and Santoro, R. J. (1985). Soot Inception in a Methane/Air Diffusion Flame as Characterized by Detailed Species Profiles. *Combust. and Flame* **62**, 157.

Vandsburger, U., Kennedy, I. and Glassman, I. (1984). Sooting Counterflow Diffusion Flames with Varying Oxygen Index. *Combust. Sci and Tech.* **39**, 263.

Wagner, H. Gg. (1978). Soot Formation in Combustion. *Seventeenth Symposium (International) on Combustion*, The Combustion Institute, p. 3.

Wagner, H. Gg. (1981). Soot Formation - An Overview. In D. C. Siegla and G. W. Smith (Eds.), *Particulate Carbon, Formation During Combustion*, Plenum Press, New York, p. 1.

Figure Captions

Figure. 1. Uncorrected thermocouple measurements of the temperature profiles as a function of radial position for several axial heights in an undiluted (flame 8) and diluted (flame 12) ethene diffusion flame. The ethene flow rate is 4.90 cm^3/s while the argon diluent flow rate is 4.50 cm^3/s

Figure 2. Comparison of uncorrected thermocouple measurements of the temperature profile at an axial height of 5 mm as a function of radial position. Results are presented for an undiluted ethene flame (flame 12) and two pairs of diluted flames (flame 5 and 6 and flames 7 and 8) which have identical calculated adiabatic temperatures (2346 and 2333 K respectively).

Figure 3. The total integrated soot volume fraction, F_v, as a function of height in the flame for a) flames 12, 5, and 6; b) flames 12, 7, and 8; c) flames 12, 3, and 4. The fuel mole fraction is listed in parentheses next to the symbol identification. The lines represent a spline fit to the data.

Figure 4. The total integrated soot volume fraction, F_v, as a function of height in the flames for pairs of flames (3 and 3a) and (6 and 7) at equal dilutions of 50% and 64% respectively. The lines represent spline fits to the data.

Figure 5. Mass Spectrometric mole fraction measurements of N_2, O_2, H_2O, and CH_4 as a function of radial position in an undiluted methane diffusion flame burning in air. The axial measurement location is 12 mm above the burner exit. The methane fuel flow rate was 5.7 cm^3/s.

Figure 6. Mass Spectrometric mole fraction measurements of CO, CO_2, H_2, and C_2H_2 as a function of radial position in an undiluted methane diffusion flame burning in air. The axial measurement location is 12 mm above the burner exit. The methane fuel flow rate was 5.7 cm^3/s. Note negative CO mole fractions are a result of a differencing procedure in which the mole fraction of CO and N_2 are deduced from measurements at two different electron voltages.

Figure 7. The maximum volumetric scattering cross section, Q_{vv}, as a function of height for diluted and undiluted ethene diffusion flames. Flow rate conditions in cm^3/s are shown in parentheses next to the symbol identification.

Figure 8. Comparison of the calculated fuel mole fraction as a function of height along the center line of a diffusion flame for two ethene fuel flow rates (2.75 cm^3/s and 6.58 cm^3/s). Calculations compare an undiluted and diluted (50% N_2) flame case. Flow rates in cm^3/s for C_2H_4 and N_2 are listed in parentheses next to the identifications of the line symbols.

Figure 9. Comparison of the calculated fuel mole fraction as a function of radial position for a diluted (50% N_2) and an undiluted ethene diffusion flame at heights of a) 0.3 mm, b) 2.7 mm, and c) 14.7 mm above the fuel tube. Flow rates in cm^3/s for C_2H_4 and N_2 are listed in parentheses next to the identifications of the line symbols.

Figure 10. Comparison of temperature and concentration effects on soot reduction with dilution for the ethene flames. Plotted is the ratio of the exponential temperature dependence of the diluted and undiluted flames versus the ratio of the soot formation rate for the corresponding diluted and undiluted conditions. The dashed line represents the total reduction in soot formation rate. The contributions of temperature and fuel concentration are shown for E_a of 40, 95, and 150 kcal/mole. The contributions of the temperature and concentration dependence for E_a=40 kcal/mole are indicated by the arrows. The present results support a value of E_a close to 95 kcal/mole.

Table 1. Flow conditions for the diluted and undiluted laminar flames specifying fuel, fuel flow rate (Q), diluent, initial fuel mole fraction (X_F) and calculated adiabatic flame temperature (T_{AD}). The total integrated soot volume fraction, F_v, and the ratio expressed in percentage of the measured F_v to the F_v for a pure undiluted fuel case is also given.

Exp #	Fuel (Q) (cm^3/s)	Diluent	X_F	T_{AD} (K)	F_v (cm^2)	% of Pure $(F_v)/(F_v)_{Pure}$
1	C_2H_4(2.75)	N_2	0.50	2310	1.66E-06	46.7
1a	C_2H_4(2.75)	Ar	0.50	2330	2.29E-06	64.7
2	C_2H_4(2.75)	Ar	0.37	2310	1.05E-06	29.6
3	C_2H_4(4.90)	N_2	0.50	2310	2.91E-06	51.8
3a	C_2H_4(4.90)	Ar	0.50	2330	3.70E-06	65.8
4	C_2H_4(4.90)	Ar	0.37	2310	2.12E-06	37.7
5	C_2H_4(4.90)	N_2	0.74	2346	4.90E-06	87.2
6	C_2H_4(4.90)	Ar	0.64	2346	4.56E-06	81.2
7	C_2H_4(4.90)	N_2	0.64	2333	4.08E-06	72.7
8	C_2H_4(4.90)	Ar	0.52	2333	3.77E-06	67.2
9	C_2H_4(6.58)	N_2	0.64	2333	5.30E-06	74.5
10	C_2H_4(6.58)	Ar	0.52	2333	4.48E-06	63.0
11	C_2H_4(2.75)	--	1.00	2369	3.54E-06	100.0
12	C_2H_4(4.90)	--	1.00	2369	5.62E-06	100.0
13	C_2H_4(6.58)	--	1.00	2369	7.10E-06	100.0

Table 2. Comparison of thermocouple temperature measurements at an axial position of 5 mm above the fuel tube for ethene flames diluted with argon and nitrogen at the same calculated adiabatic flame temperature. Maximum temperatures (T_{MAX}) as well as temperature differences ($\Delta T_{R=5mm}$) between the nitrogen and argon diluted flames (T_{N2}-T_{Ar}) are shown.

Exp. #	Fuel (Q) (cm^3/s)	Diluent	X_F	T_{AD} (K)	T_{MAX} (K)	$\Delta T_{R=5mm}$ (K)
1	C_2H_4(2.75)	N_2	0.50	2310	1934	56
2	C_2H_4(2.75)	Ar	0.37	2310	1924	
5	C_2H_4(4.90)	N_2	0.74	2346	1994	33
6	C_2H_4(4.90)	Ar	0.64	2346	2003	
7	C_2H_4(4.90)	N_2	0.64	2333	1988	56
8	C_2H_4(4.90)	Ar	0.52	2333	1988	

Table 3. Comparison of fuel concentration effects for flames at similar calculated adiabatic flame conditions.

Exp. #	Fuel (Q) (cm^3/s)	T_{AD} (K)	ΔX_F* %	ΔF_v** %	b***
1 & 2	C_2H_4(2.75)	2310	26.0	36	1.50
3 & 4	C_2H_4(4.90)	2310	26.0	27	1.06
5 & 6	C_2H_4(4.90)	2346	13.5	6.9	0.36
7 & 8	C_2H_4(4.90)	2333	18.8	7.6	0.38
9 & 10	C_2H_4(6.58)	2333	18.8	15	0.81
14 &15	C_3H_8(2.56)	2240	18.0	7.7	0.40

* ΔX_F is the difference in fuel mole fraction and is based on a comparison of Ar and N_2 diluted flam at the same calculated temperature.

** ΔF_v is the difference in total integrated soot volume fraction and is based on a comparison of Ar and N_2 diluted flames at the same calculated temperature.

*** b is based on assuming ΔF_v, is proportional to ΔX_F.

Table 4. Mitchell flame model comparisons for fuel mole fraction (X_F) in 50% diluted and undiluted ethene diffusion flames at selected radial (R) and axial (Z) coordinates.

Fuel Flow Rate (cm^3/s)	R (mm)	Z (mm)	X_F (Pure)	X_F (50%)	$\frac{X_F(50\%)}{X_F(\text{Pure})}$
6.58	4.63	0.3	0.482	0.351	0.727
6.58	4.63	2.7	0.256	0.218	0.849
6.58	0.00	14.5	0.504	0.401	0.795
4.90	4.63	0.3	0.410	0.304	0.740
4.90	4.63	2.7	0.207	0.170	0.823
4.90	0.00	14.5	0.383	0.330	0.860
2.75	4.63	0.3	0.298	0.220	0.738
2.75	4.63	2.7	0.132	0.101	0.764
2.75	0.00	14.5	0.215	0.189	0.879

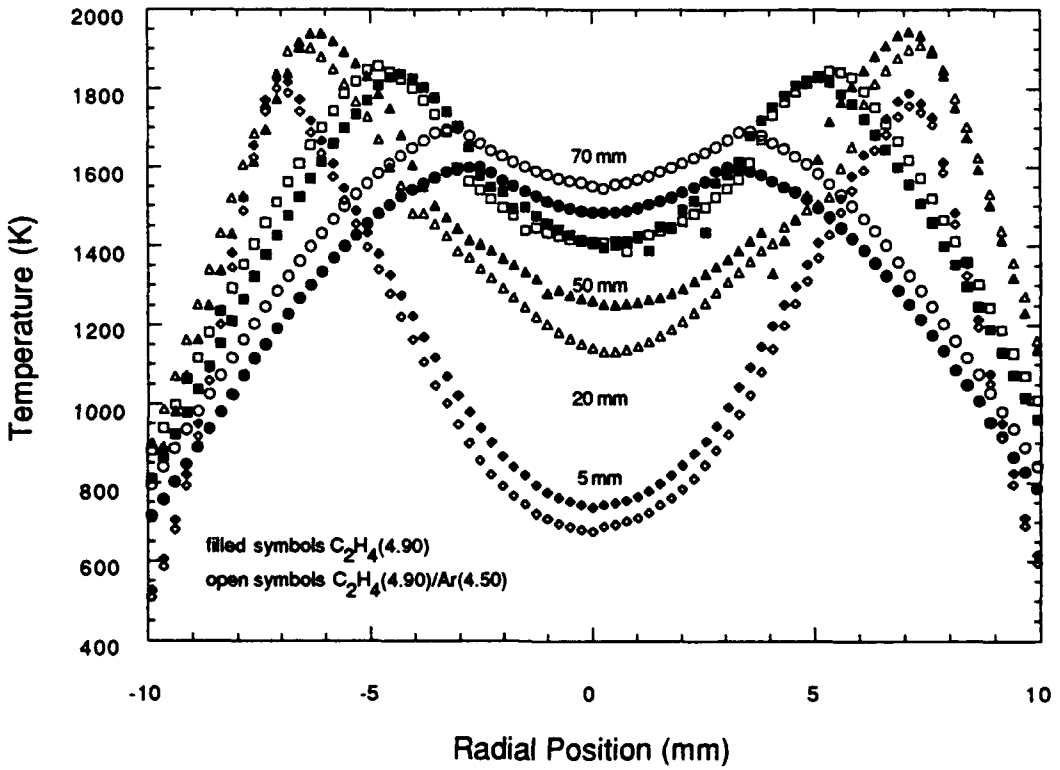
2000
1800
1600
1400
1200
1000
800
600
400
Temperature (K)
-10
-5
0
5
10
Radial Position (mm)
70 mm
50 mm
20 mm
5 mm
filled symbols C2H4(4.90)
open symbols C2H4(4.90)/Ar(4.50)

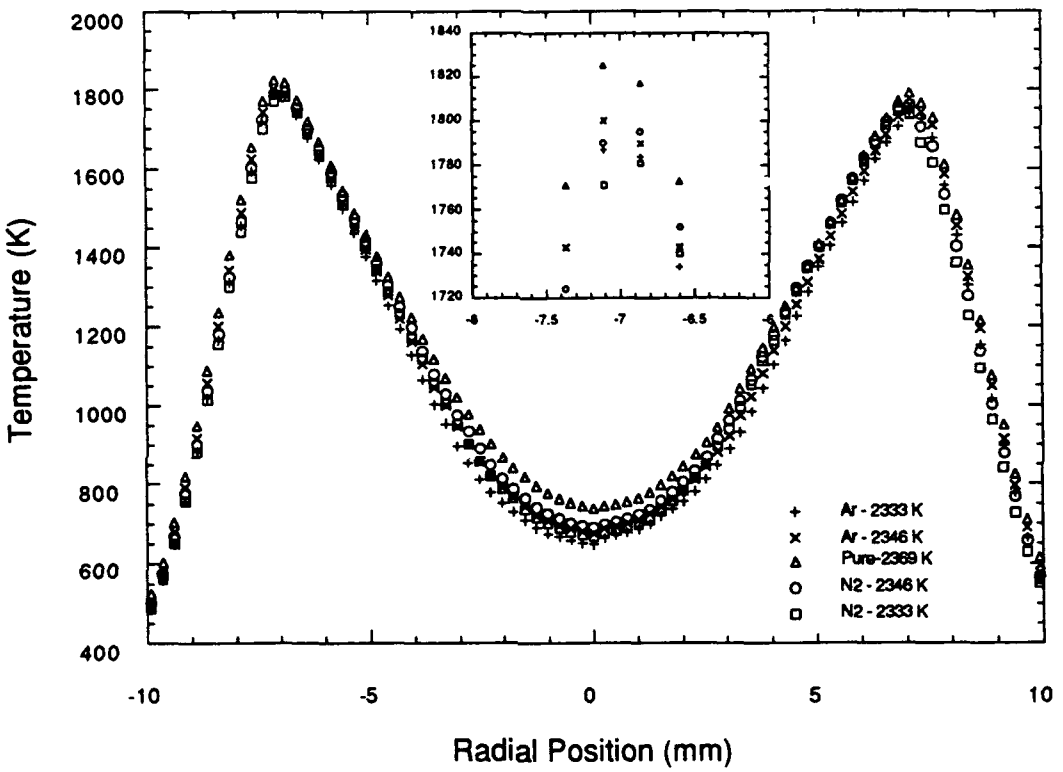

D. Anderson. Fig 2

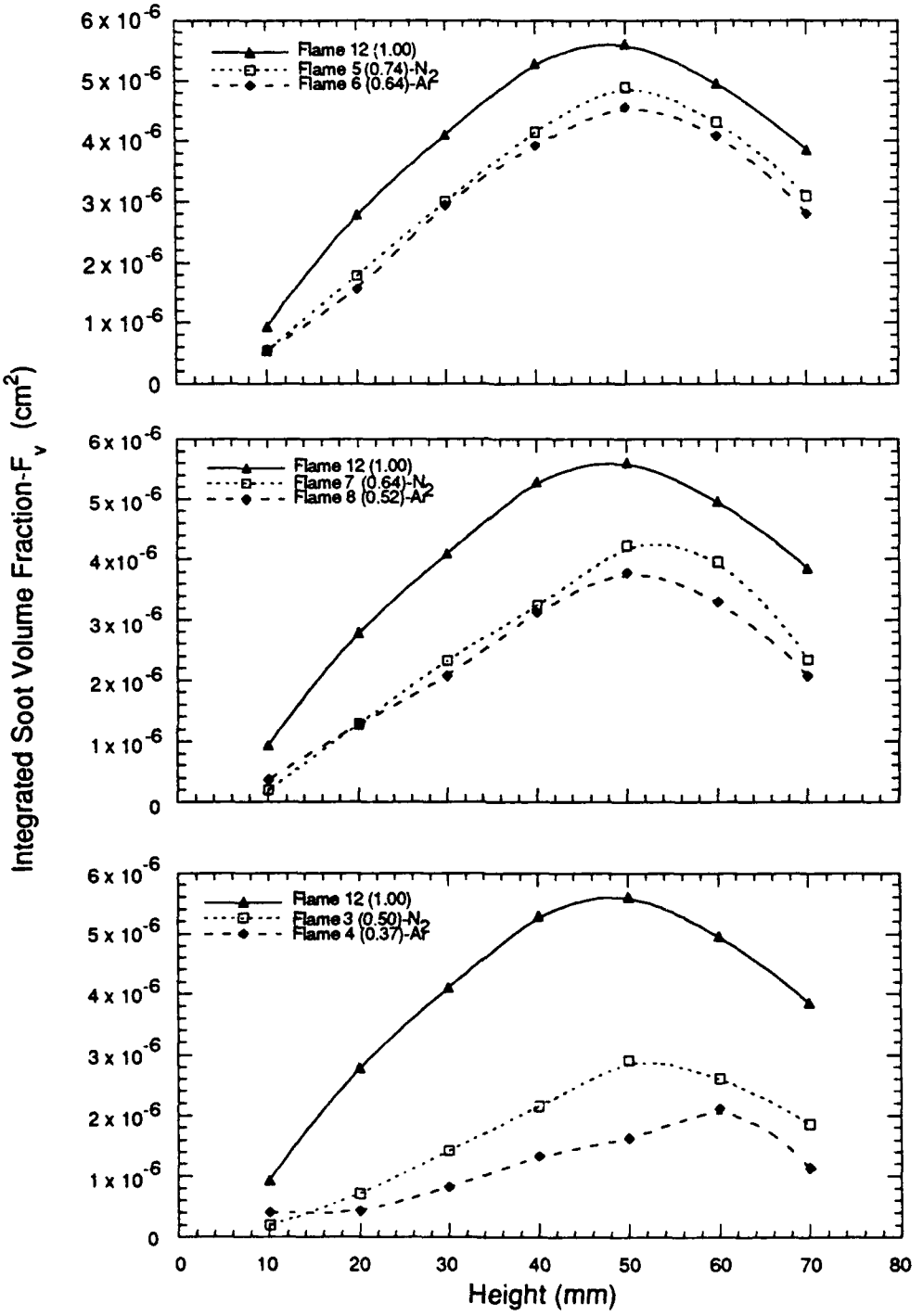
Integrated Soot Volume Fraction-F_v (cm^2)
Flame 12 (1.00)
Flame 5 (0.74)-N_2
Flame 6 (0.64)-Ar
Flame 12 (1.00)
Flame 7 (0.64)-N_2
Flame 8 (0.52)-Ar
Flame 12 (1.00)
Flame 3 (0.50)-N_2
Flame 4 (0.37)-Ar
0
1 x 10^{-6}
2 x 10^{-6}
3 x 10^{-6}
4 x 10^{-6}
5 x 10^{-6}
6 x 10^{-6}
0
10
20
30
40
50
60
70
80
Height (mm)

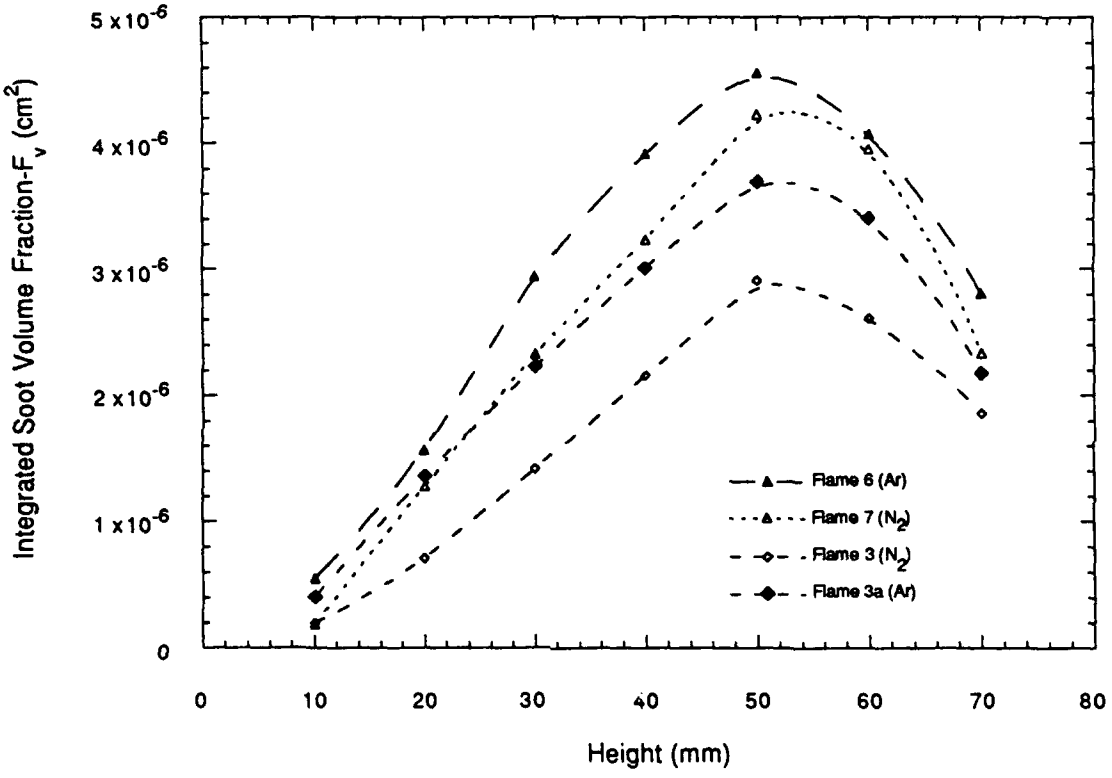

Richardson Fig. 4

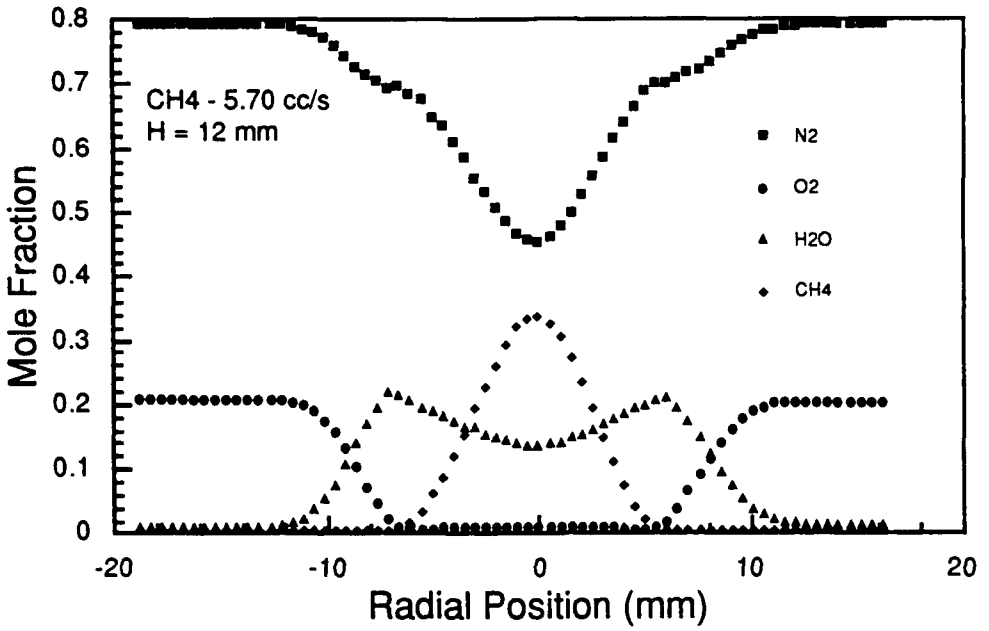

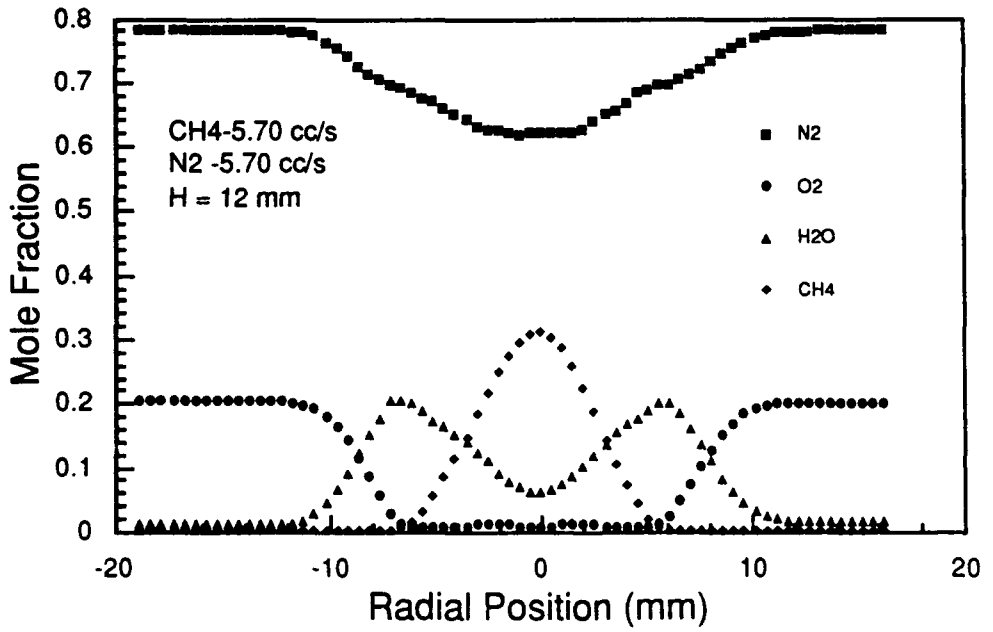

Richardson, Fig 5

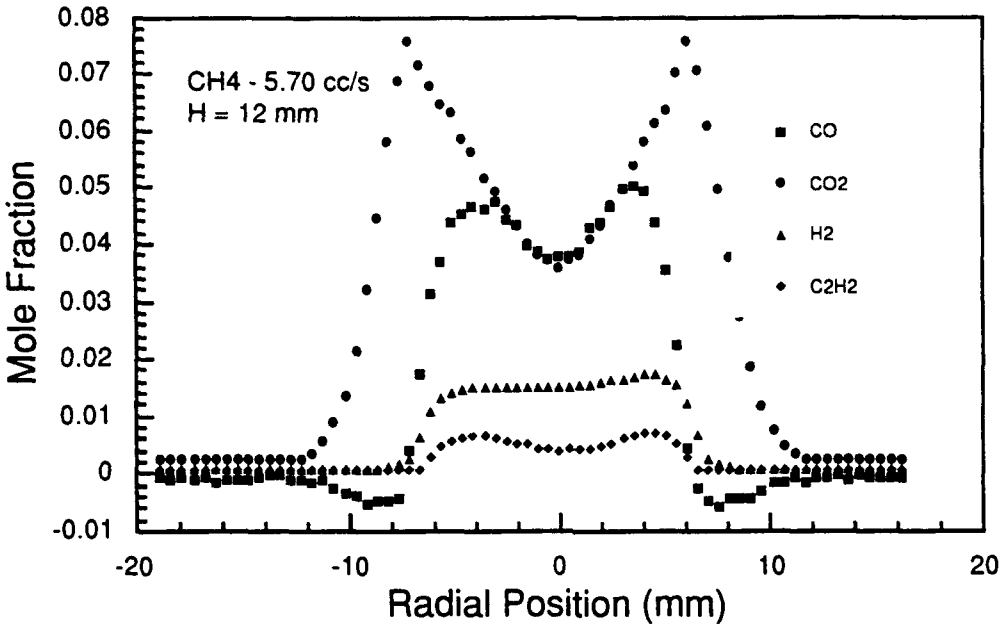
CH4 - 5.70 cc/s
H = 12 mm
CO
CO2
H2
C2H2
Mole Fraction
Radial Position (mm)
0.08
0.07
0.06
0.05
0.04
0.03
0.02
0.01
0
-0.01
-20
-10
0
10
20

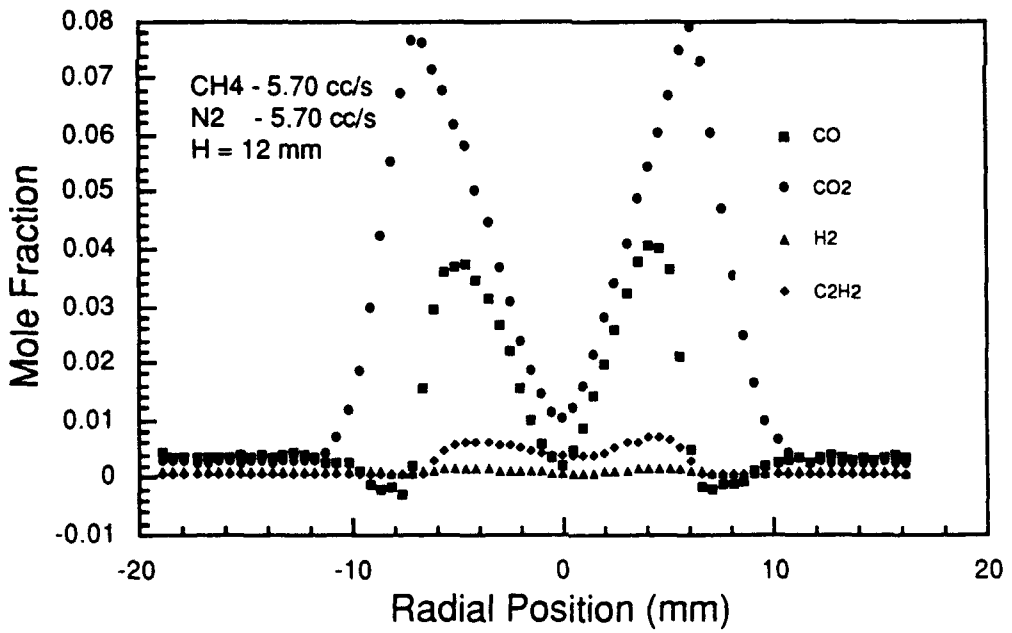
CH4 - 5.70 cc/s
N2 - 5.70 cc/s
H = 12 mm
CO
CO2
H2
C2H2
Mole Fraction
Radial Position (mm)
0.08
0.07
0.06
0.05
0.04
0.03
0.02
0.01
0
-0.01
-20
-10
0
10
20

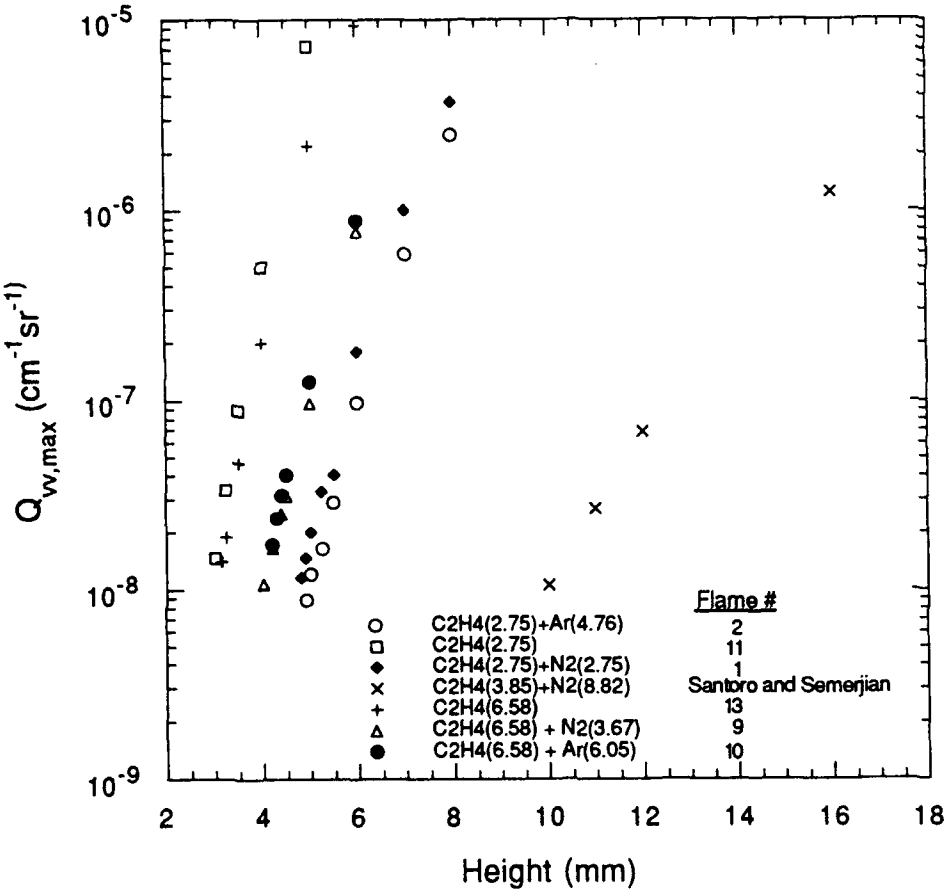

Richardson, fig 7

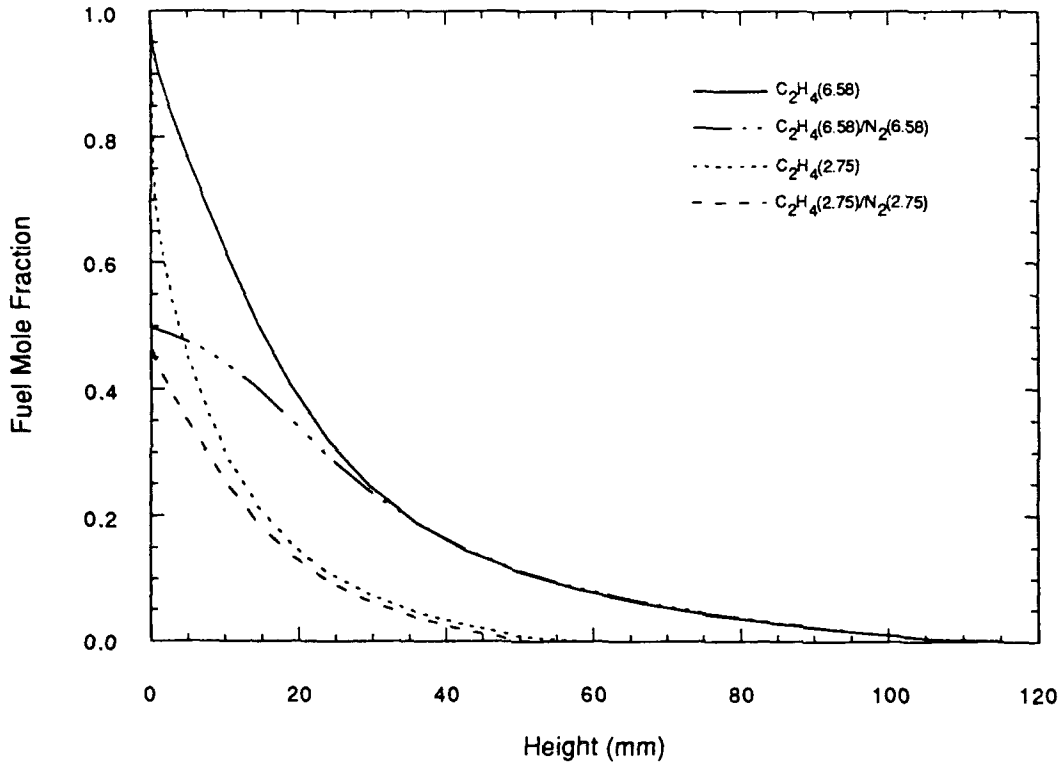
1.0
0.8
0.6
0.4
0.2
0.0
Fuel Mole Fraction
0
20
40
60
80
100
120
Height (mm)
C2H4(6.58)
C2H4(6.58)/N2(6.58)
C2H4(2.75)
C2H4(2.75)/N2(2.75)

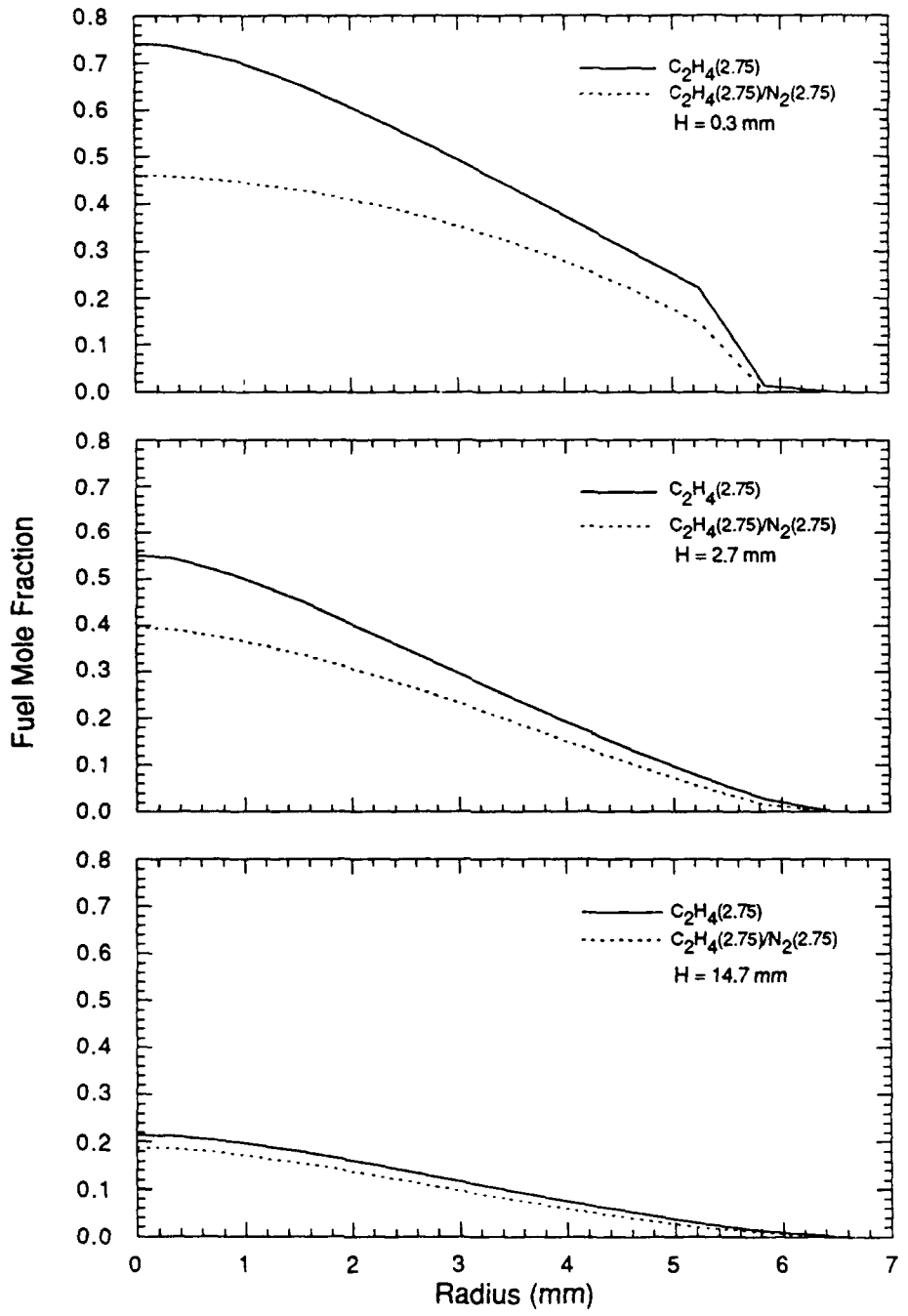
Fuel Mole Fraction
Radius (mm)
C_2H_4(2.75)
C_2H_4(2.75)/N_2(2.75)
H = 0.3 mm
H = 2.7 mm
H = 14.7 mm
0.0
0.1
0.2
0.3
0.4
0.5
0.6
0.7
0.8
0
1
2
3
4
5
6
7

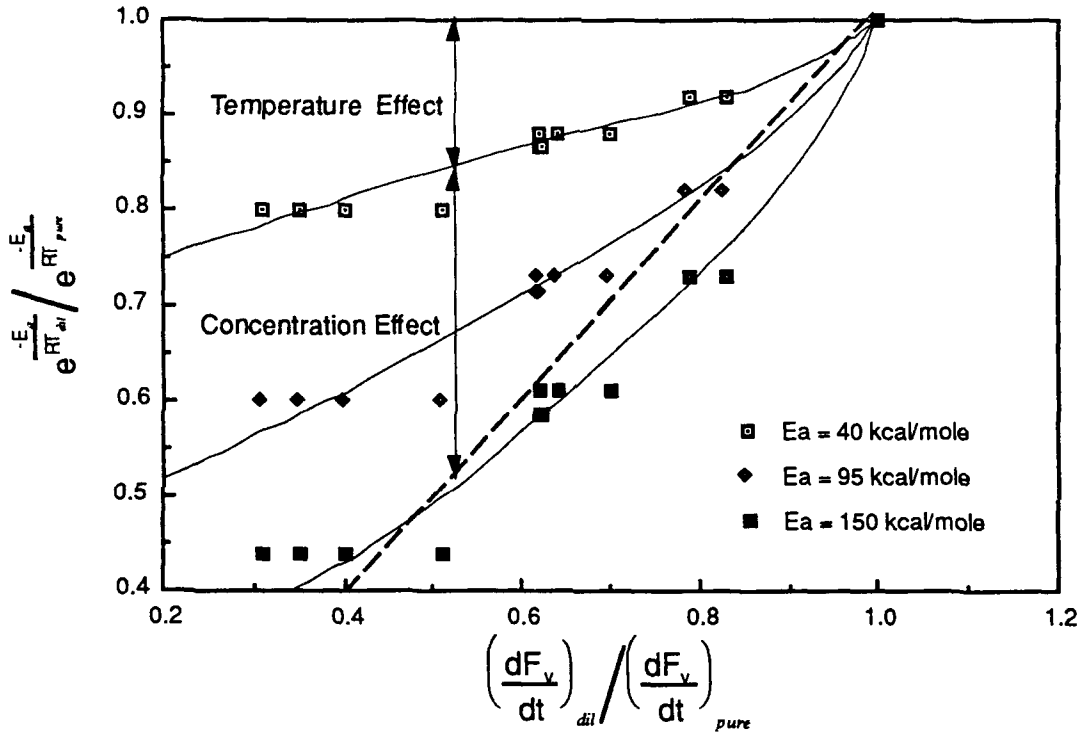
1.0
0.9
0.8
0.7
0.6
0.5
0.4
0.2
0.4
0.6
0.8
1.0
1.2
Temperature Effect
Concentration Effect
Ea = 40 kcal/mole
Ea = 95 kcal/mole
Ea = 150 kcal/mole
$\frac{-E_a}{RT_{dil}} / \frac{-E_a}{RT_{pure}}$
$\left(\frac{dF_v}{dt}\right)_{dil} / \left(\frac{dF_v}{dt}\right)_{pure}$

APPENDIX 2

Analysis of Light Scattering From Soot Using Optical Cross Sections for Aggregates

Published in the *Twenty-Third Symposium (International) on Combustion*,
The Combustion Institute, pp. 1525-1532 (1990)

Twenty-Third Symposium (International) on Combustion/The Combustion Institute, 1990/pp. 1525–1532

ANALYSIS OF LIGHT SCATTERING FROM SOOT USING OPTICAL CROSS SECTIONS FOR AGGREGATES

R. A. DOBBINS
Division of Engineering
Brown University
Providence, RI 02912

R. J. SANTORO
Department of Mechanical Engineering
The Pennsylvania State University
University Park, PA 16802

AND

H. G. SEMERJIAN
Center for Chemical Technology
National Institute of Standards and Technology
Gaithersburg, MD 20899

Soot formed in flames usually consists of aggregates (clusters or agglomerates) of a variable number of nearly spherical, monodisperse primary particles (monomers or spherules). In this work, the optical properties of polydisperse aggregates are used to analyze light scattering data from a coannular ethene diffusion flame. In previously reported studies, data have been obtained on the local extinction and volumetric scattering cross sections from laser scattering experiments, on the flame velocity field from laser velocimetry, and on the primary particle sizes determined by electron microscopy. The present analysis yields the average number of primary particles per aggregate, the mean-square radius of gyration, the soot volume fraction and the aggregation rate. It is found that sustained collisional growth of the aggregates occurs while their primary particles grow through heterogeneous reactions low in the flame, and contract through surface oxidation in the upper half of the flame. A recent value of the refractive index gives internally consistent moment ratios of the aggregate size distribution function. This method of analysis provides a more detailed and complete description of the formation, growth and oxidation of soot aggregates in a diffusion flame.

Introduction

The use of laser light scattering experiments to probe the development of the soot field in the coannular laminar ethene diffusion flame has been previously reported.[1] This work was based on the progress made by various investigators to measure the optical properties of the soot particles field with high spatial resolution[2–4] and the application of a tomographic inversion technique[5] to obtain local values of the extinction coefficient for axisymetric diffusion flames. The measured extinction and volumetric scattering cross sections were introduced into expressions derived from the Rayleigh description for the scattering of light by small spheres. Polydispersity was included by assuming the size distribution to be self preserving. However, Rayleigh theory implies that the vertically polarized component of scattering is independent of the scattering angle Θ measured from the forward direction. This condition is not fulfilled in the annular region of the flame where high soot concentrations were observed and the scattering in the forward direction was more pronounced.[6]

Subsequently a detailed mapping of the flame velocity and temperature fields[7] provided information on the soot transport and growth processes. Information on particle morphology was also developed[8] by means of a thermophoretic sampling technique. These results showed the soot particles in the ethene diffusion flame to consist of aggregates of primary particles whose shape was approximately spherical and whose diameters d_p in any one flame location was quite uniform. The optical

properties of aggregates was further studied through computational simulation[9] of both the cluster-cluster growth and the light scattering processes. These results together with the observations of the soot field by electron microscopy (TEM)[10-12] were used to formulate[13] the optical cross sections of polydisperse aggregates. Polydispersity results when the number n of primary particles per aggregate is variable within a given aggregate population, and is the inevitable result of the cluster-cluster aggregation process.

These developments now make possible the analysis of the measured optical properties of soot using the cross sections for randomly-oriented aggregates. The presence of angular dissymmetry of the scattered light provides the opportunity to perform a more detailed study than would otherwise be possible. Additionally, the accumulated data on this flame—scattering and extinction measurements, velocity data from laser Doppler anemometry, and primary particle sizes as determined by TEM—in the region of maximum soot concentration allow for a detailed examination of the dynamics of the processes which influence the soot field. In particular, with the development of an aggregate model for the optical cross sections, the effects of the aggregation process on particle morphology, surface area and number concentration can be investigated. The combination of detailed optical measurements along with an aggregate-based analysis provides an improved understanding into the evolution of soot particle fields in flames. Given the recent interest in the modeling of the formation and growth of soot particles and their relationship to flame radiation, improved approaches for the interpretation of optical measurements of soot aggregates is a topic of significant importance.

Theoretical Background

Aggregate Statistics:

A single aggregate is characterized by the primary particle diameter d_p, the number of primary particles within the aggregate n, and its radius of gyration R_g that is given by

$$R_g^2 = \frac{1}{n}\sum_i r_i^2 \tag{1}$$

where r_i is the distance of the ith primary particle to the center of mass of the aggregate. Large aggregates are mass fractals[14-16] which display scale similarity and obey the relationship

$$n = k_f\left(\frac{R_g}{d_p}\right)^{D_f} \tag{2}$$

where k_f is the prefactor and D_f is the fractal or Hausdorf dimension. When aggregates grow by cluster-cluster collision processes, the fractal dimension is in the range of 1.7 to 1.9. Although Eq. (2) applies to a population of particles on a statistical basis, even relatively small aggregates ($n \approx 5$) that do not display scale similarity have been found to follow this relationship.[12]

In order to describe a population of aggregates, it is necessary to introduce the probability distribution function (PDF) $p(n)$ that represents the relative frequency of occurrence of aggregates containing n primary particles. The q^{th} moment of the PDF is given by

$$\overline{n^q} = \sum_n n^q\, p(n) \tag{3}$$

Furthermore, for each value of n there is an associated volume-equivalent diameter D and, for the total aggregate population, the corresponding volume-mean diameter D_{30} is given[12] by

$$D_{30}^3 = d_p^3\,\overline{n^1} \tag{4}$$

where $\overline{n^1}$ is the average number of primary particles per aggregate. Since the diameters of the primary particles in a given region of a laminar flame are narrowly distributed (see Ref. 12 and the references cited therein), in this work we treat the *primary* particles as monodisperse at each flame location. With this definition, the volume fraction f_v of an aerosol of N_a *aggregates* per unit volume can be expressed as

$$f_v = \frac{\pi}{6} D_{30}^3 N_a. \tag{5}$$

The volume fraction is a quantity for which optical techniques provide direct information and is a primary quantity of interest in the present analysis.

Finally a series of relationships exist relating primary and aggregate particle properties to each other and to important observables. A moment ratio that is important in the reduction of light scattering data is f_n, which is a measure of the width of the PDF, and is defined by

$$f_n = \frac{\overline{n^2}}{(\overline{n^1})^2}. \tag{6}$$

For monodisperse aggregates f_n is unity and it attains a value near 2.0 for the continuous self preserving distribution function. This quantity explicitly enters into the analysis of light scattering measurements for determining D_{30} which is described in the next section.

The number of primary particles per unit volume can be related to the number of aggregates by

$$N_p = \overline{n^1} N_a \tag{7}$$

and the surface area per unit volume S_t can be calculated if it is assumed that the primary particles are in point contact with one another, yielding

$$S_t = \pi d_p^2 \overline{n^1} N_a. \tag{8}$$

Since surface growth leads to the formation of menisci that reduce the surface area, the value of S_t yielded by Eq. (8) is an upper bound estimate. A population of polydisperse aggregates has a mean-square radius of gyration $\overline{R_g^2}$ that is defined by weighting $R_g^2(n)$ by n^2, see Appendix I. The final important relationship relates the mean-square radius of gyration $\overline{R_g^2}$ with d_p and D_{30},

$$d_p = \frac{D_{30}^3}{\overline{\mathcal{H}}\ \overline{R_g^2}} \tag{9}$$

where $\overline{\mathcal{H}}$ is a high moment ratio of the PDF defined in Appendix I.

The above equations contain eight properties relevant to the description of a suspension of aggregates—d_p, D_{30}, f_V, N_a, N_p, $\overline{n^1}$, $\overline{R_g^2}$, and S_t. As five algebraic relationships exist, [Eqs. (4), (5), (7), (8) and (9)] and, if f_n, $\overline{\mathcal{H}}$ and D_f are known, there are three degrees of freedom. Measurements of three optical properties which are independent functions of three or more of the above eight properties are required to completely specify the aggregate population when the refractive index of the aggregate material is known. In the procedure employed below, we will consider f_n and $\overline{\mathcal{H}}$, which are not independent, as unknown and will use, as substitute information, a determination of d_p by TEM.

Optical Properties of Aggregates:

The extinction coefficient of aggregates which both absorb and scatter light[13] is given by

$$K_{ext}^A = K_{abs}^A(1 + \overline{\rho_{sa}}) = \frac{4\pi N_a \overline{n^1} x_p^3 E(m)}{k^2}(1 + \overline{\rho_{sa}}) \tag{10}$$

where

$$E(m) = -Im\left(\frac{m^2 - 1}{m^2 + 2}\right) \tag{11}$$

with $x_p = \pi d_p/\lambda$, $k = 2\pi/\lambda$, $m = m_r - im_i$ is the refractive index, and $\overline{\rho_{sa}}$ is the ratio of the scattering to absorption cross sections for the population of polydisperse aggregates.[13] The determination of $\overline{\rho_{sa}}$, which is often small but is significant at midflame heights in the ethene diffusion flame, is given in Appendix II.

Because the product of $\overline{n^1}$, d_p^3, and N_a appears in Eq. (10), the particle volume fraction is directly obtainable from a measurement of extinction without any requirement of knowledge of the size distribution function. By combining Eqs. (5) and (10), we find the particle volume fraction,

$$f_V = \frac{K_{ext}^A}{3\,k\,E(m)(1 + \overline{\rho_{sa}})} = \frac{K_{abs}^A}{3\,k\,E(m)} \tag{12}$$

The volumetric scattering cross section $Q_{VV}^A(\Theta)$ for vertically polarized scattered light, when the incident beam is also vertically polarized with respect to the scattering plane, is the product of N_a and the mean cross section of the aggregates.[13] It is given by

$$Q_{VV}^A(\Theta) = \frac{N_a \overline{n^2}\, x_p^6\, F(m)}{k^2} f(q_i^2\, \overline{R_g^2}) \tag{13}$$

with

$$F(m) = \left|\frac{m^2 - 1}{m^2 + 2}\right|^2 \tag{14}$$

and q_i is the modulus of the scattering vector defined by

$$q_i = \frac{4\pi}{\lambda} \sin\frac{\Theta_i}{2}. \tag{15}$$

The function $f(q_i^2\, \overline{R_g^2})$ results from the examination of the angular scattering of light by aggregates[13] and its functional form depends on $q_i^2\, \overline{R^2}$ and D_f as summarized below. For small and intermediate sizes, $q_i^2\, R_g^2 < 1.5\, D_f$, the function $f(q_i^2\, \overline{R_g^2})$ is given by

$$f(q_i^2\, \overline{R_g^2}) = \exp\left(-\frac{q_i^2\, \overline{R_g^2}}{3}\right) \tag{16}$$

while for larger sizes, $q_i^2\, \overline{R_g^2} > 1.5\, D_f$, the following expression applies,

$$f(q_i^2 \overline{R_g^2}) = \frac{C_p}{(q_i^2 \overline{R_g^2})^{D_f/2}} \tag{17}$$

where $C_p = (1.5\, D_f/e)^{D_f/2} = 0.9939$ for $D_f = 1.80$ as is representative for cluster-cluster aggregation. Equations (16) and (17) result from the detailed investigation[13] of the influence of polydispersity on the optical properties of randomly oriented aggregates, and they are related to expressions which ap-

pear in the literature of fractals.[14-16] The inclusion of the effects of polydispersity of the aggregates is an imperative consideration in understanding the soot formation processes in flames.

The mean-square radius of gyration, $\overline{R_g^2}$, is directly yielded by solving Eqs. (13), (16) and (17) as appropriate for the ratio $R_{ij} = Q_{VV}^{A}(\Theta_i)/Q_{VV}^{A}(\Theta_j)$, which depends only on $k^2\,\overline{R_g^2}$ for specified values of Θ_i and Θ_j since all other quantities cancel. When $q_f^2\,\overline{R_g^2} < 1.5\ D_f$ ($R_{ij} < b_{ij}$), Eq. (16) is applicable and we find

$$\overline{R_g^2} = \frac{a_{ij}}{k^2}\,\ell n\ R_{ij} \tag{18}$$

Somewhat larger aggregates will result in $q_f^2\,\overline{R_g^2} > 1.5\ D_f$ ($R_{ij} > c_{ij}$) and $\overline{R_g^2}$ is then found by using both Eqs. (16) and (17) to formulate R_{ij}. In this event, it becomes necessary to solve the transcendental equation

$$(q_f^2\,\overline{R_g^2})\exp\left(-\frac{q_f^2\overline{R_g^2}}{1.5\ D_f}\right) = \left(\frac{R_{ij}}{d_{ij}}\right)^{2/D_f} \tag{19}$$

The values of the quantities a_{ij}, b_{ij}, c_{ij}, and d_{ij} are defined in general terms in Table I where they are also tabulated for $\Theta_i = 45°$ and Θ_j equal to either 90° or 135° for a fractal dimension $D_f = 1.8$. Two determinations of $\overline{R_g^2}$ yielded by the use of two sets of dissymmetry ratios provide replication of this datum, but they do not afford independent information about the aggregate population. In the data analysis given below, we report the average of the two values of $\overline{R_g^2}$ found from the dissymmetry ratios R_{12} and R_{13}.

We find the volume mean diameter by dividing Eq. (10) by (13) and using Eq. (6) to eliminate n^2 in favor of f_n and n^1. The result is

$$D_{30} = \frac{\lambda}{\pi}\left(\frac{4\pi E(m)\,Q_{VV}^{\lambda}(\Theta_i)}{f_n\,F(m)f(q_i^2\,\overline{R_g^2})K_{abs}^{\lambda}}\right)^{1/3} \tag{20}$$

From Eqs. (5) and (20) for f_V and D_{30} we find N which can be expressed as

$$N_a = \frac{36k^3 f_V}{4\pi x_{30}^3} \tag{21}$$

where $x_{30} = \pi D_{30}/\lambda$.

When $q_i^2\overline{R_g^2} \ll 1$, Eq. (13) reduces to the expression applicable to Rayleigh-size spheres even though the particles are actually aggregates of small spheres. In this particular case, $\overline{R_g^2}$ and d_p do not appear in the equations, and their values cannot be determined from the above measurements. Although the values of f_V, D_{30}, and N_a are yielded by the extinction-scattering measurements, no direct information on whether the observed particles are spheres or aggregates is provided. Independent observations are then required in order to determine the actual particle morphology. Without this added information the determination of S_f is impeded.

Data Analysis and Discussion

The flame burner which is described elsewhere[1] consisted of two coannular brass tubes of 11.1 and 101.6 mm i.d.; ethene flows through the central tube at the rate of 3.85 cm^3/s while the air flow is 713 cm^3/s corresponding to the nonsooting (NS) flame previously described.[1] In this experiment a laser light scattering apparatus is used to determine the local extinction K_{ext} and the volumetric scattering cross sections $Q_{VV}(\Theta_i)$ at $\Theta_i = 45°$, 90°, and 135°. These quantities were measured as a function of height along a soot particle path in the annular region of

Table I
Value of Constants for Use in the Determination of the Mean Square Radius of Gyration from Eqs. (18) and (19) for $\Theta_i = 45°$, and $\Theta_j = 90°$ or 135° when $D_f = 1.80$

	r_{ij}	a_{ij}	b_{ij}	c_{ij}	d_{ij}
$ij = 12$	0.5412	2.121	1.890	3.020	3.039
$ij = 13$	0.4142	1.061	2.108	4.886	4.916

The above quantities are defined by

$$r_{ij} = \sin(\Theta_i/2)/\sin(\Theta_j/2) \qquad a_{ij} = 0.75\Big/\left(\sin^2\frac{\Theta_i}{2} - \sin^2\frac{\Theta_j}{2}\right)$$

$$b_{ij} = \exp[0.5D_f(1 - r_{ij}^2)] \qquad c_{ij} = r_{ij}^{(D_f+2)}$$

$$d_{ij} = c_{ij}/C_{ij} \qquad C_{ij} = (1.5\ D_f/e)^{D_f/2}$$

high soot concentration in the coannular laminar flame. In the following analysis we take advantage of three bodies of experimental data—the scattering-extinction measurements,[1] the laser velocity data,[7] and observations of primary particle size obtained by thermophoretic sampling and TEM examination.[8,11] The availability of this information for the ethene diffusion flame allows the soot field to be examined along a soot particle path which, owing to the action of thermophoresis, does not coincide with a gas streamline in the lower portion of the flame where velocities are lower and thermal gradients are large. In addition, the velocity data provides a conversion of height above the burner, z, to time and allows differentiation of certain quantities to obtain rate data.

The quantity $\bar{\mathcal{H}}$ contains a ratio of higher moments of the aggregate PDF about which only limited information is available. The values of f_n and $\bar{\mathcal{H}}$ are not independent as both are influenced by the width of the aggregate PDF. We have therefore analyzed the data by treating $\bar{\mathcal{H}}$ and f_n as quantities to be adjusted to give the best agreement between d_p based on optical measurements using Eq. (9) and from TEM observations. The values of D_{30} and N_a are independent of $\bar{\mathcal{H}}$ and are weakly influenced by f_n, while d_p is sensitive to f_n and to $\bar{\mathcal{H}}$ that has a broader range of variation. On the other hand, the quantities f_V and $\overline{R_g^2}$ are calculated without reference to $\bar{\mathcal{H}}$.

The values of d_p obtained from Eq. (9) are also influenced by the refractive index m that is used in the analysis of this data. For a given value of m, we find a unique value of the product $(f_n\bar{\mathcal{H}})$ that yields the minimum rms of $[d_p\text{ (TEM)} - d_p\text{ (opt)}] = C_r$. In Table II, we list the optimum values of f_n and $\bar{\mathcal{H}}$ that are mutually consistent with a single value of the geometric mean standard deviation σ_z for a discrete log normal distribution. Three values of refractive index[17-19] are used in this analysis. In Table II we find incompatible values of f_n and $\bar{\mathcal{H}}$ result when $m = 1.57 - i0.56$. On the other hand, when the recent value[19] of $m = 2.10 - i0.55$ is used, $f_n = 1.3$ and $\bar{\mathcal{H}} = 3.1$ are found to be mutually consistent with a narrow distribution, $\sigma_z = 0.15$. This combination of parameters was selected to obtain the data used in Figs. 1 to 4 for which $C_r = 18\%$.

Recently it has been reported[20,21] that the value of m depends on the hydrogen content of the soot. We have explored this possibility by treating of the refractive index to be height dependent to simulate the annealing action of the hot flame gases. The refractive index m is allowed to vary weakly with height z and achieves the value of the $m = 2.10 - i0.55$ near the tip of the flame as described in the footnote in Table II. In addition, $\bar{\mathcal{H}}$ is varied to be consistent with the vertical variation of $\overline{n^1}$ shown in Fig. 3 below for a log normal distribution with $\sigma_z = 0.30$. These interesting results are shown in the last line of Table II and, although tentative, they suggest a future direction for research.

Figure 1 shows the values of N_a and D_{30} obtained from Rayleigh theory and from aggregate theory plotted against height. At $t_1 = 25$ ms the quantity $f_V q_t^2 \overline{R_g^2}$ is equal to unity and the two methods give the same values for these two properties. The differences between the values of D_{30} and N_a that are predicted by the two methods is significant at all other times.

The quantities f_V, D_{30}, and N_a are displayed in Fig. 2, and the quantities R_g, D_{30}, d_p(TEM), and $\overline{n^1}$ are given in Fig. 3. These quantities follow a consistent pattern. The soot volume fraction f_V in-

Table II

Values of f_n, $\bar{\mathcal{H}}$ and K_a recovered from minimization of fractional RMS of $[d_p\text{ (TEM)} - d_p\text{ (opt)}]$ for selected values of refractive index, m at $\lambda = 514.5$ nm.

m	Ref.	f_n	$\bar{\mathcal{H}}$	σ_z note 1)	K_a note 2)
$1.57 - i0.56$	17	1.0	10.1	—	490×10^{-6} m/s
$1.90 - i0.55$	18	1.1	5.0	0.05	180
$2.10 - i0.55$	19	1.3	3.1	0.15	96
$m(z)$ note 3)	—	1.44	2.97 to 1.95 note 4)	0.30	79

1. Values of geometric mean standard deviation σ_z are estimated from discrete log normal distributions which yield the indicated values of f_n and $\bar{\mathcal{H}}$.

2. K_a is the aggregation rate as defined by Eq. (23).

3. Refractive index varies according to $m(z) = m_r - 1 - i\,m_i(x - z/h)^{0.08} + 1$ with $m_r = 2.10$, $m_i = 0.55$, and $h = 70$ mm corresponding to the highest observation.

4. The values of f_n and $\bar{\mathcal{H}}$ are determined to be consistent with $\overline{n^1}(z)$ shown in Fig. 3 by assuming a discrete log normal distribution with $\sigma_z = 0.30$ and $K_a = 3.8$.

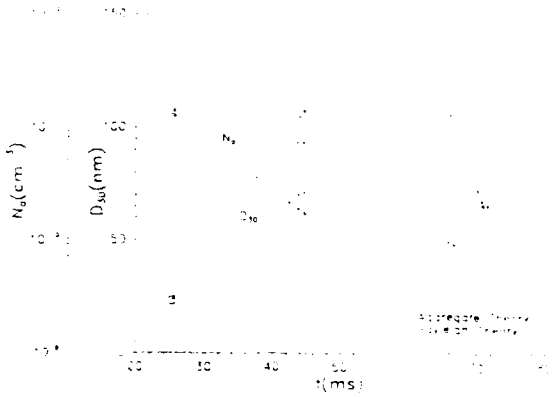

FIG. 1. Comparison of Data Reduction of Rayleigh Theory for Spheres and Aggregate Theory for the Coannular Laminar Diffusion Flame (NS flame, Q = 3.85 cm³/s). (N_a and D_{30} are plotted versus residence time t. Time equals zero at the burner mouth.)

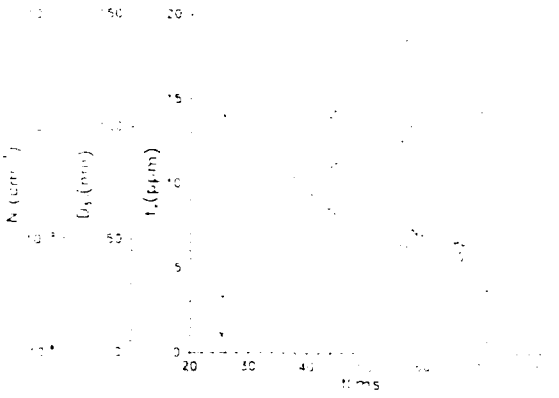

FIG. 2. The Quantities D_{30}, f_v, and N_a vs. t as Determined Using Cross Sections for Aggregates.

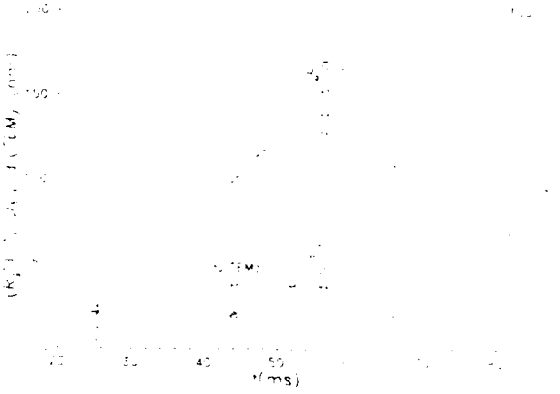

FIG. 3. The Quantities D_{30}, $\overline{n^1}$ and $(\overline{R_z^2})^{1/2}$ vs. t as Determined Using Cross Sections for Aggregates. (Values of d_p (TEM) are from electron microscopy.)

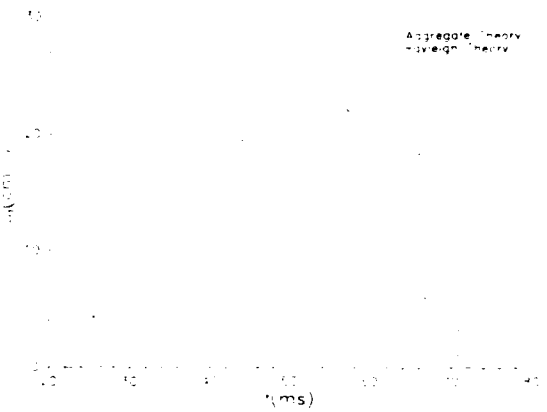

FIG. 4. Surface Area per Unit Volume S_t from Rayleigh Theory for Spheres and from Aggregate Theory Based on Point Contact of Primary Particles vs. t.

creases during the region where surface growth dominates ($25 < t < 56$ ms) and then decreases as particle oxidation occurs. Both D_{30} and d_p parallel this trend. The aggregate number concentration N_a generally decreases as would occur if aggregation continues in the presence of either surface growth or oxidation of the primary particles. The average number of primary particles per aggregate $\overline{n^1}$ and the mean-square radius of gyration $\overline{R_z^2}$ increase as a result of cluster-cluster aggregation. Primary particle concentration N_p is not shown but is found to remain close to 1×10^{12} cm^{-3} for all t.

The particle surface area, S_t, calculated using $\overline{n^1}$, N_a, and d_p (TEM) is shown in Figure 4. Also displayed is the value of S_t were it to be calculated on the basis that the particles are spheres rather than aggregates. It is apparent that the predicted surface areas differ by a factor of two to four. This difference is quite significant in the evaluation of the surface growth rates and points to the importance of accounting for the aggregate structure of the particles.

From the aggregate number concentration that is shown in Fig. 1, we calculate the aggregation rate K_a which is defined through the expression[22]

$$\frac{dN_a}{dt} = -\frac{K_a}{2} N_a^2 \qquad (22)$$

The latter equation can be rearranged as

$$K_a = \frac{2}{N_a t_1} \frac{d}{dt}\left(\frac{N_a t_1}{N_a t}\right) \qquad (23)$$

and therefore the slope of the least-square straight line fit to the graph of the ratio $N_a t_1/N_a t$ vs. time t yields an average value of K_a. Values of K_a that result from use of the several values of refractive

index are given in Table II. A value of $\approx 6.0 \times 10^{-10}$ cm^3/s at 298 K is typical of spherical particles.[22] The lowest value of $K_a = 79 \times 10^{-10}$ cm^3/s (quoted in Table II) appears to be reasonable, but replication of these results is desired.

Summary and Conclusions

A data reduction method that is based on the use of optical cross sections for aggregates has been applied to measurements of local extinction and differential scattering at three angles by soot aggregates in a laminar ethene diffusion flame. As compared to the Rayleigh data reduction for spherical particles, this method yields higher values of volume-mean diameter, a larger surface area per unit volume, and lower values of the aggregate number concentration. The analysis also provides the mean-square radius of gyration and the average number of primary particles per aggregate. Both these quantities increase monotonically with time as is consistent with the occurrence of cluster-cluster aggregation. Primary particle diameter is also obtained from the optical observations and it has been independently measured by thermophoretic sampling followed by TEM analysis. By requiring the rms difference between the two observations of primary particle size to be a minimum, we obtain information on the allowable values of refractive index. Higher values of the real portion of the refractive index give more plausible moment ratios of the size distribution of the aggregates. The present results indicate that a self-consistent interpretation of the light scattering properties of the soot aerosol is afforded by recognizing its aggregate structure. In particular, significant differences in the surface area and number concentration are observed for soot aerosols consisting of aggregates of primary particles. These differences have important ramifications in deriving chemical and physical rate data from the laser scattering extinction experiment. Furthermore, when combined with TEM analysis of the primary particles which constitute the aggregates, the present analysis provides the basis for evaluating the importance of other particle properties such as refractive index. Thus, this method of data analysis provides a more detailed and comprehensive description of the development and character of the soot aggregate population in laminar diffusion flames.

Acknowledgments

This work was supported by the Center for Fire Research of the National Institute of Standards and Technology, under grant numbers **60NANB6D0643** and **60NANB7D0706** and the Air Force Office of Scientific Research, Air Force Systems Command, USAF under grant number **AFOSR-87-0145**. One of the authors (R. A. D.) received partial support from the Center for Chemical Technology of the National Institute of Standards and Technology during a recent sabbatical leave. The assistance of Mr. Michael Carrier of NIST with aspects of the computations is acknowledged with appreciation.

Appendix I
Relationship Between d_p and $\overline{R_g^2}$ For Polydisperse Aggregates

For a polydispersion of aggregates, the mean-square radius of gyration is defined by

$$\overline{R_g^2} = \frac{\sum_n R_g^2(n)\, n^2\, p(n)}{\sum_n n^2\, p(n)} \tag{A1}$$

and from Eqs. (2), (4) and (A1), it follows that

$$d_p = \frac{D_{30}^3}{\bar{\mathcal{H}}\, \overline{R_g^2}} \tag{A2}$$

where

$$\bar{\mathcal{H}} = \frac{\sum_n n^2\, p(n) \sum_n n\, p(n)}{\sum_n \left(\frac{n}{k_f}\right)^{2/D_f} n^2\, p(n)}. \tag{A3}$$

When $D_f = 2.0$, Eq. (A3) reduces to

$$\bar{\mathcal{H}} = k_f \frac{\overline{n^1}\ \overline{n^2}}{\overline{n^3}}. \tag{A4}$$

The value of the prefactor k_f was found through computer simulations[9] to be 5.8. For narrow size distributions $\bar{\mathcal{H}} \to k_f$, while for discrete log normal distributions of moderate width $\bar{\mathcal{H}}$ decreases to less than two when $D_f = 1.8$. An examination of two aggregate samples, which were taken in the ethene diffusion flame[12] at a height $z = 15$ mm above burner, yields $f_n \approx 1.8$ and $\bar{\mathcal{H}} \approx 1.5$ to 1.7, in general agreement with calculations based on a discrete log normal PDF.

Appendix II
Correction of Observed Extinction to Obtain the Volumetric Rayleigh Absorption Cross Section

For aggregates of moderate size, $q^2\overline{R_g^2}$ about equal to unity or larger, the measured extinction contains, in addition to absorption which dominates in

the case of the smaller aggregates, a significant contribution owing to scattering. The extinction can be expressed

$$K_{ext} = K_{abs}(1 + \overline{\rho_{sa}}) \quad (A5)$$

where $\overline{\rho_{sa}}$ is the ratio of the scattering cross section to the absorption cross section. The latter is given by[13]

$$\overline{\rho_{sa}} = f_n \overline{n^1}\, \omega_p\, g(k^2 \overline{R_g^2}) \quad (A6)$$

where ω_p, the albedo of the primary particle, is given by

$$\omega_p = \frac{2}{3} x_p^3 \frac{E(m)}{E(m)} \quad (A7)$$

and the function $g(k^2 \overline{R_g^2})$ given by

$$g(k^2 \overline{R_g^2}) = \left(1 + \frac{4}{3D_f} k^2 \overline{R_g^2}\right)^{D_f/2} \quad (A8)$$

From Eqs. (4) and (A2) the first moment of the aggregate size distribution can be expressed by

$$\overline{n^1} = \bar{n} \frac{\overline{R_g^2}}{d_p^2} \quad (A9)$$

The ratio of scattering to extinction $\overline{\rho_{sa}}$ can be calculated using TEM observations of d_p and the values of $\overline{R_g^2}$ found using the observed disymmetry ratios, R_{12} and R_{13}. With specified values of $\bar{n}$ and f_n, the quantities $\overline{n^1}$ ω_p, g and $\overline{\rho_{sa}}$ can be calculated. In the non-smoking ethene flame, the value of $\overline{\rho_{sa}}$ is as high as 30% in the midflame region where the primary particles are 33 nm in diameter. Thus, the peak values of soot volume fraction f_v are reduced by about 30% below the value which would be predicted by the conventional Rayleigh analysis for spheres in which a contribution to extinction by scattering is not included.

REFERENCES

1. Santoro, R. J., Semerjian, H. G., and Dobbins, R. A., Comb. Flame 51, 203 (1983).
2. D'Alessio, A., Dilorenzo, A., Borghese, A., Beretta, F., and Masi, S., Sixteenth Symposium (International) on Combustion, p. 695. The Combustion Institute 1977.
3. Haynes, B. S. and Wagner, H. Gg., Ber. Bunsenges Phys. Chem. 84, 499 (1980).
4. Kent, J. H., Jander, H. and Wagner, H. Gg., Eighteenth Symposium (International) on Combustion, p. 113. The Combustion Institute 1981.
5. Santoro, R. J., Semerjian, H. G., Emmerman, P. J., and Goulard, R., Int. J. Heat and Mass Trans. 24, 1139 (1981).
6. Dobbins, R. A., Santoro, R. J., and Semerjian, H. G., Combustion Diagnostics by Nonintrusive Methods, (T. D. McCay and J. A. Roux, Eds), Progress in Astronautics and Aeronautics, 92, 208 (1984).
7. Santoro, R. J., Yeh, T. T., Horvath, J. J., and Semerjian, H. G., Comb. Sci. Tech. 53, 89 (1987).
8. Dobbins, R. A. and Megaridis, C. M., Langmuir 3, 254 (1987).
9. Mountain, R. D. and Mulholland, G. W., Langmuir 4, (1988).
10. Megaridis, C. M. and Dobbins, R. A., Twenty-Second Symposium (International) on Combustion, p. 353. The Combustion Institute 1989.
11. Megaridis, C. M. and Dobbins, R. A., Comb. Sci. Tech. 66, 1 (1989).
12. Megaridis, C. M. and Dobbins, R. A., Comb. Sci. Tech. 71, 95 (1990).
13. Dobbins, R. A. and Megaridis, C. M., to appear in Applied Optics. See also Proceedings of the 2nd International Symposium on Optical Particle Sizing, Tempe, AZ, March 1990.
14. Jullien, R. and Botet, R., Aggregation and Fractal Aggregates, World Scientific, Singapore (1987).
15. Schaefer, D. W., MRS Bulletin XIII, 22 (1988).
16. Botet, R. and Jullien, R., Annales de Physique 13, 153 (1988).
17. Dalzell, W. H. and Sarofim, A. F., Heat Transfer 91, 100 (1969).
18. Lee, S. C. and Tien, C. L., Eighteenth Symposium (International) on Combustion, p. 1159. The Combustion Institute 1981.
19. Vaglieco, B. M., Beretta, F., D'Alessio, A., Comb. Flame 79, 259 (1990).
20. Habib, Z. G. and Vervisch, P., Comb. Sci. Tech. 59, 261 (1988).
21. Charalampopoulos, T. T., Chang, H. and Stagg, B., Fuel 68, 1173 (1989).
22. Hinds, W. C., Aerosol Technology, Wiley and Sons, New York (1982).

APPENDIX 3

Isolation of Buoyancy Effects in Jet Diffusion Flame Experiments

Published in *Combustion Science and Technology*,
73, pp. 625-635 (1990)

Combust. Sci. and Tech., 1990, Vol. 73, pp. 625-635
Photocopying permitted by license only

SHORT COMMUNICATION

Isolation of Buoyancy Effects in Jet Diffusion Flame Experiments

R. W. DAVIS and E. F. MOORE *Center for Chemical Technology, National Institute of Standards and Technology, Gaithersburg, MD 20899*

R. J. SANTORO and J. R. NESS *Department of Mechanical Engineering, The Pennsylvania State University, University Park, PA 16802*

(*Received February 15, 1990; in final form June 25, 1990*)

Abstract—Buoyancy is an important factor in the dynamic behavior of jet diffusion flames. In order to determine the exact role that buoyancy plays, a simple procedure is described for varying in isolation the relative buoyancy force in stationary laboratory jet diffusion flame experiments. This procedure, which is derived from a theoretical model of these flames, merely requires that background pressure be varied while maintaining constant mass flows of fuel and oxidizer into the burner. It is shown that the sole result of these pressure variations in the theoretical model is that the effective gravitational acceleration acting upon the flame varies as the square of the pressure. Comparisons are made between the structure of a low speed laboratory methane/air flame at various pressures and the results of a direct numerical simulation of the same flame with various gravitational accelerations. Similar evolutions in flame structure are observed in both cases.

INTRODUCTION

Investigations into the dynamic structure of jet diffusion flames have become more common in the last decade [Yule *et al.* (1981), Eickhoff and Winandy (1985), Roquemore *et al.* (1989), Takahashi *et al.* (1988), Chen *et al.* (1988)]. This is because these geometrically-simple flames exhibit many features which are generic to more complex combusting flows. The interactions between the flame surface and outer surrounding vortex structures are of particular concern, especially in low speed and transitional (buoyancy-dominated) jet diffusion flames. It is these interactions which are apparently responsible for various forms of flame flicker [Chen *et al.* (1988), Roquemore *et al.* (1989), Buckmaster and Peters (1986)]. Since the outer vortex structures form in a buoyancy-driven shear layer outside the flame surface, it becomes highly desirable to vary the buoyancy force (relative to inertial and viscous forces) in isolation from all other parameters in order to observe the resulting effects, especially on flame flicker. However, this has been difficult and expensive to do, requiring accelerating test rigs [*e.g.*, Altenkirch *et al.* (1976)]. It is the purpose of the present paper to outline a more practical procedure for isolating buoyancy effects in experiments involving jet diffusion flames.

The procedure to be described here is derived from a theoretical model for jet diffusion flames based on the flame sheet and conserved variable approximations. It will be shown that buoyancy effects in this model can be isolated by simply maintaining constant mass flows of fuel and oxidizer into the burner while varying the background pressure. In order to test the validity of this procedure, results obtained from numerical solutions of the equations of motion are compared with experimental results obtained in a pressure chamber. A similar evolution in large-scale flickering behavior is observed both numerically and experimentally as pressure increases, albeit

at different pressure levels due presumably to stability differences between the computed and actual flames. Previous experimental investigations of jet diffusion flames at varying pressures have focused on the structural effects of Reynolds number variations in the excited case [Strawa and Cantwell] or on soot formation [Flower (1988)]. The present study is believed to be the first investigation of these flames to focus solely on isolating buoyancy effects. It is not, however, the purpose of this paper to thoroughly document these effects but instead to open the door to future more exhaustive studies.

THEORETICAL BACKGROUND

The nondimensional continuity, momentum and state equations for the unsteady axisymmetric flow of a multicomponent fuel jet surrounded by a coflowing airstream are

$$\frac{\partial \rho}{\partial t} + \nabla \cdot (\rho \mathbf{q}) = 0, \tag{1}$$

$$\rho \frac{\partial \mathbf{q}}{\partial t} + \rho(\mathbf{q} \cdot \nabla)\mathbf{q} = -\nabla \tilde{p} - \rho Ri \hat{e}_z + \frac{1}{Re}\{-\nabla x(\nabla x \mu \mathbf{q}) + 4/3\nabla(\mu \nabla \cdot \mathbf{q}) + \nabla(\mathbf{q} \cdot \nabla \mu) - \mathbf{q}\nabla^2 \mu + \nabla \mu x(\nabla x \mathbf{q}) - (\nabla \cdot \mathbf{q})\nabla \mu\}, \tag{2}$$

$$\rho T \sum_i R_i Y_i = p_0 = R_{air}. \tag{3}$$

Here ρ is density; μ is viscosity; T is temperature; $\mathbf{q} = (v, u)$, where v and u are velocity components in an axisymmetric reference frame (r, z); Y_i is the mass fraction of species i with gas constant R_i; and $\hat{e}_z$ is the unit normal in the axial direction. The pressure consists of a constant background pressure, p_0, plus a perturbation pressure, $\tilde{p}(r, z, t)$, where $p_0 > > \tilde{p}$. As discussed by Rehm and Baum (1978), the omission of $\tilde{p}$ from Eq. (3) is entirely appropriate here, resulting in the suppression of acoustic waves while admitting the low frequency motions due to buoyant effects. All quantities in Eqs. (1–3) have been nondimensionalized with respect to conditions in the coaxial airstream at the burner inlet. Thus Re = Reynolds number = $\frac{U_0 L}{\nu_0}$ and Ri = Richardson number = $\frac{gL}{U_0^2}$, where U_0 and ν_0 are the entering airstream velocity and kinematic viscosity; L is the fuel jet radius, and g is gravitational acceleration.

In order to reduce the complexity of the problem while still providing a good approximation to the physical situation, a flame sheet model (infinite rate kinetics) will be employed here. In addition, the Lewis number (ratio of thermal to species diffusivities) is assumed to be unity. Therefore, conserved variables, β_i, for species mass fractions and enthalpy can be utilized. These obey the simple nondimensional convection-diffusion equation

$$\frac{\partial(\rho \beta_i)}{\partial t} + \nabla \cdot (\rho \mathbf{q} \beta_i) = \frac{1}{Pe} \nabla \cdot (\rho D \nabla \beta_i), \tag{4}$$

where D is binary diffusion coefficient and Pe = Peclet number = $U_0 L/D_f$, with D_f taken as the diffusion coefficient of fuel into nitrogen at the burner inlet. The conserved variables are defined as

$$\beta_1 = \frac{\alpha Y_{ox} + Y_f^I - Y_f}{\alpha Y_{ox}^I + Y_f^I},$$

$$\beta_2 = \frac{h - h_{ox}^I + \dfrac{Y_f Q}{\alpha}}{\dfrac{Y_f^I}{\alpha} Q + h_f^I - h_{ox}^I}.$$

Here h is enthalpy; Q is heat release per unit mass of oxygen consumed; $\alpha = \dfrac{\nu_f M_f}{\nu_{ox} M_{ox}}$, where ν is stoichiometric coefficient and M molecular weight; subscripts f and ox refer to fuel and oxidizer (with nitrogen accounted for in the enthalpy); and superscript I refers to burner inlet conditions. The analytical model for the jet diffusion flame under discussion here consists of Eqs. (1–4) along with appropriate boundary conditions. A flame sheet exists at locations where $\beta_1 = Y_f^I/(\alpha Y_{ox}^I + Y_f^I)$. The solution method will be discussed in the next section. The remainder of the discussion here will focus on the overall characteristics of the model.

It is apparent from Eqs. (1–4) that, given a fixed set of boundary conditions, the solution field is dependent upon only three parameters: Re, Ri, and Pe. Of particular concern here is the Richardson number, Ri, which represents the ratio of buoyancy forces to inertial forces. By varying this parameter independently, it is possible to isolate the effects of a varying relative buoyancy force (or gravitational acceleration) on the theoretical jet diffusion flame. If the model here is assumed to be a good approximation to reality, then this isolation of buoyancy effects could also be performed experimentally if Ri could be independently varied in the laboratory. A procedure for accomplishing this will now be discussed.

A simple method for varying Ri while keeping Re, Pe and the boundary conditions fixed is merely to maintain constant mass flows of both fuel and air into the burner while varying the background pressure. Since $\rho_0 U_0$ is fixed and μ_0 is pressure independent, Re will remain constant under this procedure. Both U_0 and D_f vary inversely with pressure, thus maintaining a fixed Pe. However, Ri will vary as the square of the pressure. Since the other thermophysical properties inherent in the model (specific heats, Lewis number) can be assumed independent of pressure, this variation in Ri is the *only* effect of the background pressure changes. Thus, the effective gravitational acceleration will vary as pressure squared, *e.g.*, a background pressure of 2 atmospheres corresponds to 4 g's. This relationship is the basis of this paper and will be investigated both computationally and experimentally. It is reasonable to believe that, at least over a moderate range of pressure changes, this procedure can provide a simple means of varying the relative buoyancy force in these flames without resorting to expensive moving test rigs.

NUMERICAL MODEL

The analytical model consisting of Eqs. (1–4) and appropriate boundary conditions is solved numerically by means of a modified version of the finite difference scheme

employed previously by Davis and Moore (1985) to simulate cold mixing layer dynamics. This scheme employs a variably-spaced staggered mesh in which pressures are defined at cell centers and normal velocities at cell faces. Quadratic upwind differencing is used for convection, and an explicit Leith-type of temporal differencing is employed. At each time step, a Poisson equation for perturbation pressure is solved by a direct method. Variable thermophysical properties are calculated as described by Mitchell (1980), and no turbulence or radiation models are employed. Species binary diffusion is taken as fuel into nitrogen inside the flame and oxygen into nitrogen outside. All relevant variables are specified at the burner inlet ($z = 0$); axisymmetry is enforced along the burner centerline; and zero or constant gradients are employed at very large axial and radial distances (*i.e.*, no shroud). Mesh dimensions are 5000 fuel jet radii axially (145 mesh cells) and 50 radially (84 cells), both attained by employing rapidly expanding mesh cell sizes away from the flame. Run times on the NIST CYBER 205 are typically several hours, with initial solution fields obtained by means of a steady-state flame simulation [Davis and Moore (1987)]. After awhile, flame flickering commences in the unsteady computation without the triggering required in the cold jet case [Davis and Moore (1985)]. The numerical model just described has also been used to study the dynamic structure of propane/air jet diffusion flames, the results of which have compared well with experimental visualizations [Davis *et al.*].

EXPERIMENTAL APPARATUS

The experimental portion of this study was conducted in a high pressure diffusion flame burner (Figure 1) designed for operation at pressures up to twenty atmospheres. The coannular burner employed here consists of a fuel tube of 1.10 cm inner diameter surrounded by a 10.16 cm inner diameter air passage. The air passage is partially filled with glass beads followed by a series of fine mesh screens to provide for flow conditioning of the incoming air. A honeycomb section 2.54 cm in thickness with 0.15 cm square cells is located at the burner exit to provide a uniform exit air flow field. The fuel tube, which extends 0.25 cm above the ceramic honeycomb, is also partially filled with glass beads for flow conditioning.

The burner is housed in a high pressure chamber which consists of two cylindrical sections. The lower section is constructed of 20 cm nominal diameter pipe (8 inch diameter, schedule 40 carbon steel pipe) which is 61 cm in length. This section houses the motorized translational stage which provides for vertical movement of the burner. Electrical connections as well as gas lines for the air and fuel are introduced through a flange located on the bottom of this section. The bottom flange is attached to a ball bearing stage which supports the weight of the entire chamber. Horizontal movement of the chamber can thus be achieved using a small motorized translation stage. Both the horizontal and vertical movements of the burner are controlled by stepper motors which are interfaced to a laboratory personal computer. For the present study only the vertical motion capability was required.

The upper section of the chamber contains four 6.35 cm diameter windows which are 1.27 cm in thickness and are at the same axial height 90° apart. These windows provide access for high speed video recording as well as laser diagnostic measurements. This section is constructed of a 76.2 cm long, 15 cm nominal diameter carbon steel pipe with a wall thickness of 2.19 cm. This thicker wall pipe is required in order to maintain the proper material strength after machining the holes for the windows. The operating pressure for the burner is controlled using manual valves located on a

where D is binary diffusion coefficient and Pe = Peclet number = $U_0 L/D_f$, with D_f taken as the diffusion coefficient of fuel into nitrogen at the burner inlet. The conserved variables are defined as

$$\beta_1 = \frac{\alpha Y_{ox} + Y_f^I - Y_f}{\alpha Y_{ox}^I + Y_f^I},$$

$$\beta_2 = \frac{h - h_{ox}^I + \dfrac{Y_f Q}{\alpha}}{\dfrac{Y_f^I}{\alpha} Q + h_f^I - h_{ox}^I}.$$

Here h is enthalpy; Q is heat release per unit mass of oxygen consumed; $\alpha = \dfrac{\nu_f M_f}{\nu_{ox} M_{ox}}$, where ν is stoichiometric coefficient and M molecular weight; subscripts f and ox refer to fuel and oxidizer (with nitrogen accounted for in the enthalpy); and superscript I refers to burner inlet conditions. The analytical model for the jet diffusion flame under discussion here consists of Eqs. (1–4) along with appropriate boundary conditions. A flame sheet exists at locations where $\beta_1 = Y_f^I/(\alpha Y_{ox}^I + Y_f^I)$. The solution method will be discussed in the next section. The remainder of the discussion here will focus on the overall characteristics of the model.

It is apparent from Eqs. (1–4) that, given a fixed set of boundary conditions, the solution field is dependent upon only three parameters: Re, Ri, and Pe. Of particular concern here is the Richardson number, Ri, which represents the ratio of buoyancy forces to inertial forces. By varying this parameter independently, it is possible to isolate the effects of a varying relative buoyancy force (or gravitational acceleration) on the theoretical jet diffusion flame. If the model here is assumed to be a good approximation to reality, then this isolation of buoyancy effects could also be performed experimentally if Ri could be independently varied in the laboratory. A procedure for accomplishing this will now be discussed.

A simple method for varying Ri while keeping Re, Pe and the boundary conditions fixed is merely to maintain constant mass flows of both fuel and air into the burner while varying the background pressure. Since $\rho_0 U_0$ is fixed and μ_0 is pressure independent, Re will remain constant under this procedure. Both U_0 and D_f vary inversely with pressure, thus maintaining a fixed Pe. However, Ri will vary as the square of the pressure. Since the other thermophysical properties inherent in the model (specific heats, Lewis number) can be assumed independent of pressure, this variation in Ri is the *only* effect of the background pressure changes. Thus, the effective gravitational acceleration will vary as pressure squared, *e.g.*, a background pressure of 2 atmospheres corresponds to 4 g's. This relationship is the basis of this paper and will be investigated both computationally and experimentally. It is reasonable to believe that, at least over a moderate range of pressure changes, this procedure can provide a simple means of varying the relative buoyancy force in these flames without resorting to expensive moving test rigs.

NUMERICAL MODEL

The analytical model consisting of Eqs. (1–4) and appropriate boundary conditions is solved numerically by means of a modified version of the finite difference scheme

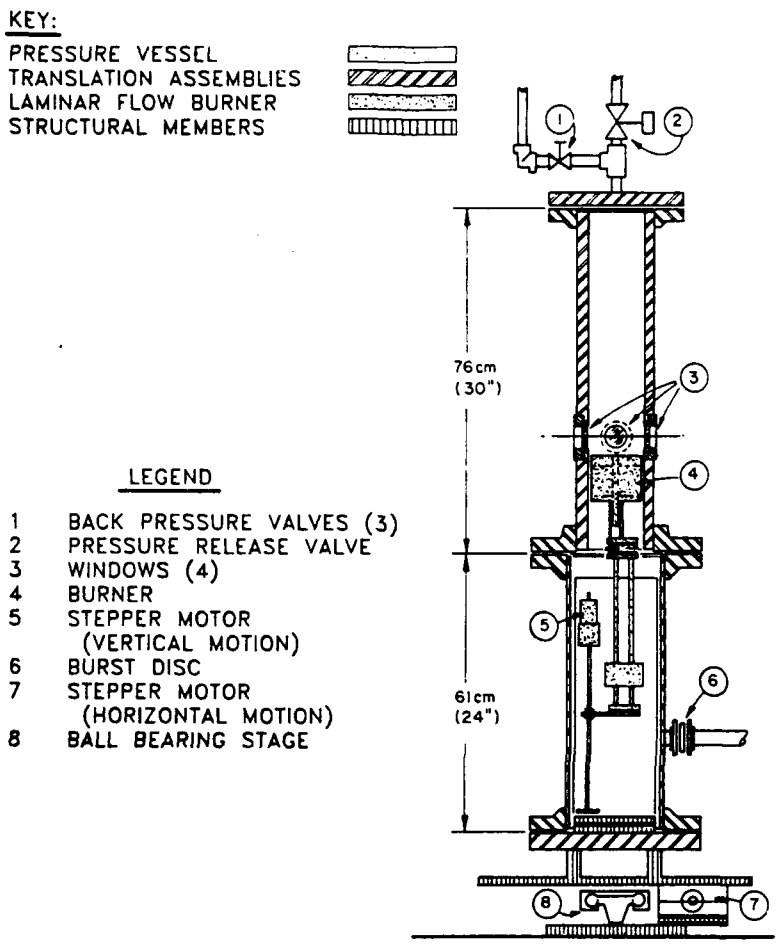

FIGURE 1 Schematic representation of high pressure diffusion flame burner.

flange mounted to the top of the pressure chamber. Steady operating pressures over a range of one to twenty atmospheres have been maintained in this system.

Gas flows are measured using a mass flow metering system. For the fuel flow rates, a mass controller is utilized which maintains the mass fuel flow rate constant regardless of the chamber pressure. The air flow rate is monitored using a mass flow meter and, thus, the air flow has to be manually adjusted to maintain a constant mass flow rate for the air as the chamber pressure is varied.

In the present study methane was burned with air supplied from an in-house compressor capable of providing source pressures of 300 psig and up to 300 SCFM of air to the burner. These capabilities exceed the pressure and flow rate requirements for this study. Prior to introducing the air into the burner it is passed through filters to remove particles and moisture. Methane is supplied from high pressure cylinders with a purity of 99%.

High speed video recording of the flame structure was obtained using a Spin Physics high speed video camera operated at a 500 Hz framing rate. Observations of the flame were made through one of the four windows located in the chamber and provided a

TABLE I
Experimental/Numerical Comparison of Tip-Cutting Heights and Frequencies

Pressure, p_0 (atm)		Tip-Cutting Height, H, (cm)		Frequency, f (Hz)	
Experiment	Computation	Experiment	Computation	Experiment	Computation
1.0	0.50 (Ri = 0.34)	H = 8[1]	H = 10[1]	Steady	Steady
1.5	0.75 (Ri = 0.76)	8	9	18.5	15
2.0	1.20 (Ri = 1.94)	6	7	15	15
3.0	1.41 (Ri = 2.70)	4	6	16	15

[1] H denotes full height of steady flame

5.1 cm open aperture viewing region. The flame structure images were obtained using the soot luminosity of the flame. Since the flame dimensions typically exceeded the 5.1 cm viewing area provided by the window, the burner was raised or lowered to an appropriate region of interest for study. In some cases a series of video sequences were required to characterize the entire flame. The Spin Physics camera also provides the capability to play back the recorded images at slow speeds or a single frame at a time. This capability was used in the analysis of the recorded images which follows.

RESULTS AND DISCUSSION

As a test of the aformentioned procedure for varying the relative buoyancy force in jet diffusion flames, a coordinated series of computations and experiments has been carried out. The selected configuration was a methane/air diffusion flame with fuel and air burner inlet velocities at one atmosphere of 10 and 20 cm/sec, respectively, and a fuel jet radius of 0.55 cm. This flame appears virtually steady at atmospheric pressure while entering into a simple tip-cutting mode at higher pressures. This mode is quite regular in frequency and extremely reproducible in terms of the flame structures which result. The flame is observed to periodically pinch off at a particular axial height, with the cut-off tip being convected upward while the lower region recedes. The lower part of the flame subsequently increases in length and the cycle repeats. When viewed in real time, this periodic tip-cutting appears as a flickering flame. The large-scale features of this flickering phenomenon are highly dependent on pressure level, thus allowing use of simple flame visualizations to make comparisons between experiment and computation. Due to the low flow velocities involved, buoyancy is clearly an important factor in this flame's behavior, while small-scale turbulence is almost certainly not. The low level of soot production minimizes radiative losses, and the Lewis number can reasonably be assumed as unity. Thus, for all these reasons, this flame was deemed to be a suitable candidate for the present study.

Experiments involving this methane/air flame have been carried out at pressures ranging from 1 to 8 atmospheres. In these experiments the mass flow rates of the fuel and air were maintained constant as the chamber operating pressure was increased. Thus, the volumetric flow rates and linear velocities at the burner exit were proportionately reduced. Corresponding computations (with slug flow burner inlet velocity profiles) have been performed by simply varying the gravitational acceleration in the model as the square of this background pressure; *i.e.*, $Ri \propto p_0^2$, where Ri = 1.35 for p_0 = 1 atm. The results are summarized in Table I, with the evolution in flame structure as a function of p_0 (or Ri) shown in Figure 2. This figure compares

recorded images of the experimental flame at four pressures with computed flame sheets (solid squares) and their surrounding vortex structures visualized via nondimensional isovorticity contours. Note that the (nondimensional) scales in the experimental and computational visualizations shown here have not been matched and that the computational visualizations extend lower than the experimental ones. It can be seen from Figure 2 and Table I that the experimental and computational evolutions of flame structure with increasing pressure are strikingly similar. The computational evolution, however, occurs at lower pressures, a subject which will be discussed subsequently. The particular computational pressures chosen for these comparisons were selected so as to match the experimental flame visualizations as closely as possible, with phase angles arbitrarily picked. The flame structure seen at low pressure (1 atm experimentally; 0.5 atm computationally) in Figure 2a is essentially steady, although there is slight tip wavering in both cases. Some weak outer vortices can be seen near the flame tip in the computational visualization. At the higher pressures (1.5 atm experimentally; 0.75 atm computationally) of Figure 2b, tip-cutting has begun in both cases. The tip-cutting height, H_t, and frequency, f, are indicated in Table I for both the experimental and computational cases. The external vortex structures have strengthened and moved downward as compared with Figure 2a. This is due to the increased buoyancy-induced velocity gradients at this pressure, with the effective gravitational acceleration here being greater than that for Figure 2a by a factor of 2.25. At the next higher pressure (2 atm experimentally; 1.2 atm computationally), the cut-off tip has assumed a basically triangular shape with a cusped region flaring out from its base. Both the experimental and computational tip-cutting heights have decreased from Figure 2b, with the outer vortices also moving down commensurately. The experimental frequency, but not the computational one, has dropped slightly. The situation at even higher pressure (3 atm experimentally; 1.41 atm computationally) is illustrated in Figure 2d. The base of the cut-off tip has straightened out to produce a highly triangular shape. The tip-cutting heights have dropped again, the frequencies are about the same, and the outer vortex structures are somewhat lower. It is clear from both Table I and Figure 2 that the experimental evolution of flame structure with increasing pressure compares well with the evolution computed via Richardson number increases, thus tending to confirm the basic validity of the buoyancy-isolation procedure at issue here.

Although comparisons between numerical and experimental results have been made for a pressure range of one to three atmospheres, high speed video recordings have been obtained for pressures as high as eight atmospheres. Comparisons are limited to the lower range of pressures because three-dimensional effects become significant at pressures near and above four atmospheres, thus rendering comparisons with the axisymmetric model of little value. This loss of axisymmetry in the experimental flame is most evident in the evolution of the upper section of the flame after a "tip-cutting" event has occurred. Under all pressure conditions where flickering is observed, the luminous cut-off region is observed to disappear with time. This is due to the oxidation of the soot particles which are responsible for the observed luminosity. For the pressure range of one to three atmospheres, this process is observed to proceed in a regular, symmetric manner with the lowest regions of the cut-off tip oxidizing first. As the pressure is raised to four atmospheres and above, the rapid oxidation process is observed to favor one side of the cut-off tip and to proceed diametrically upward and across this upper flame structure. At pressures between five and six atmospheres, the upper flame structure is actually split into two or four sections depending on the chamber pressure. In each case, these observations are highly reproducible from cycle to cycle and clearly demonstrate the strengthening of

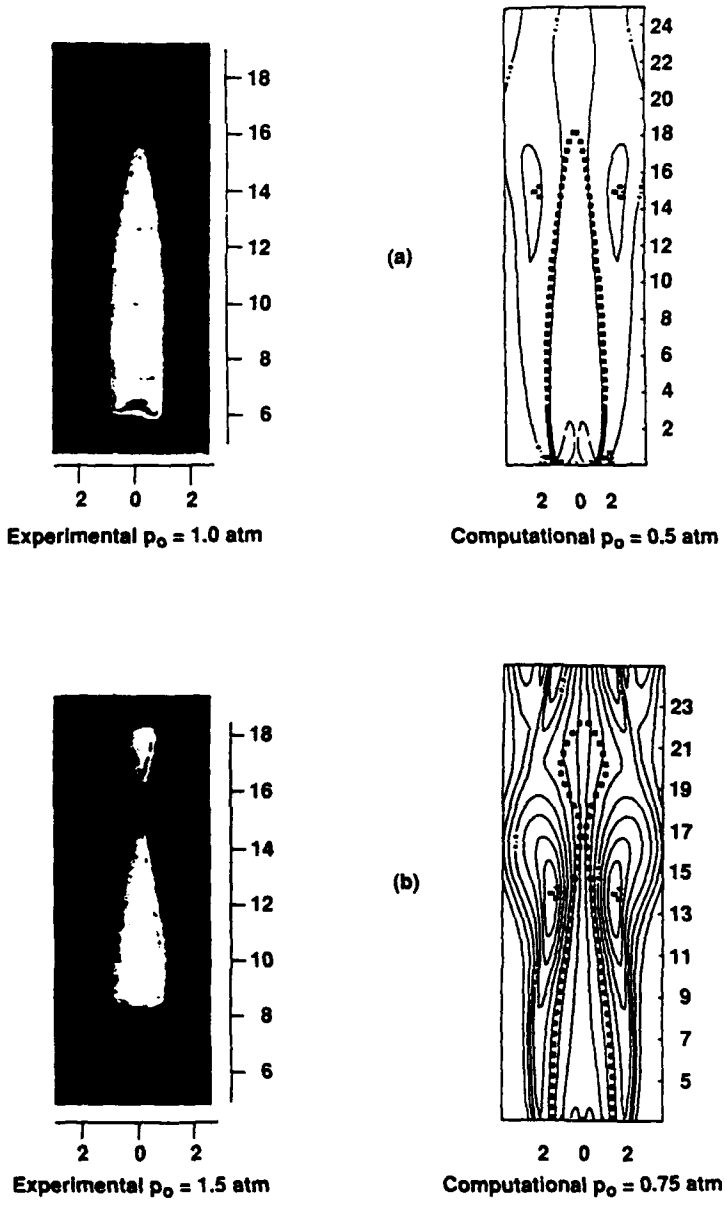

FIGURE 2 Comparisons between experimentally recorded images and computational flames (solid squares with surrounding isovorticity contours) at various values of background pressure. Length scales are in terms of fuel jet radii.

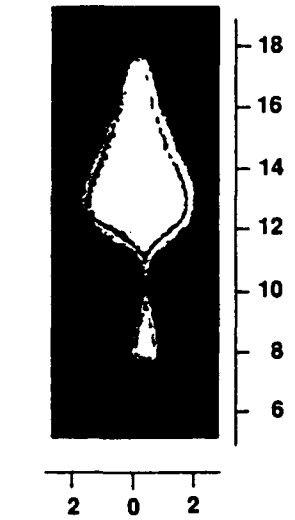

Experimental p_o = 2.0 atm

(c)

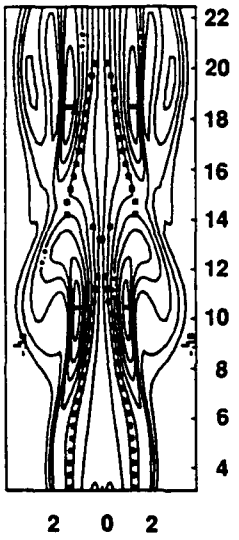

Computational p_o = 1.2 atm

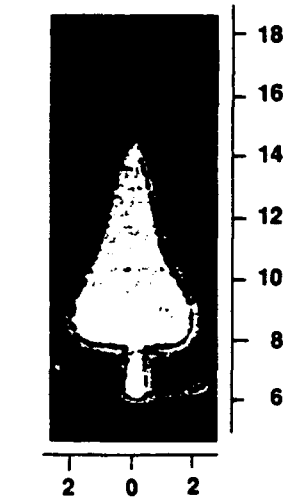

Experimental p_o = 3.0 atm

(d)

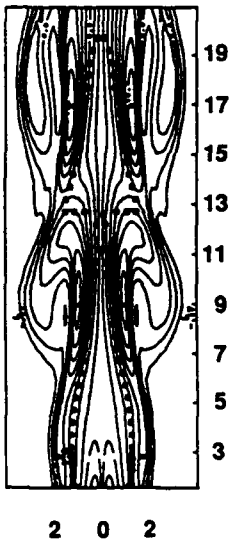

Computational p_o = 1.41 atm

azimuthal instabilities with rising pressure. This increasing instability, however, is precisely the type of behaviour that would be expected as Ri increases, as found by Subbarao (1989) in experimental studies of buoyant helium jets. It is also noted that the addition of full three-dimensionality to the model employed here would in no way affect the conclusions previously reached concerning the relationship between background pressure variations and the relative buoyancy force.

Finally, the lower pressures (or effective gravitational accelerations) found in the computational evolution in Figure 2 require some explanation. This is probably due to the use of the flame sheet approximation and the lack of any radiation in the model, thus resulting in higher temperatures computationally than experimentally. This, in turn, should lead to higher velocities and sharper gradients in the computed flame than in the experimental one, thus rendering the former more unstable. Thus it should require less effective gravitational acceleration to trigger a particular stage of the structural evolution process computationally than experimentally. Therefore, comparisons between computational and experimental results at the same pressure would not be particularly meaningful. This can be seen by comparing the computational visualization in Figure 2d with the experimental visualization in Figure 2b, which are both at approximately the same pressure. There is clearly little similarity between these two visualizations, yet a great deal of similarity is observed when comparisons are made at appropriate differential pressures.

CONCLUSIONS

A simple procedure has been described for isolating buoyancy effects in jet diffusion flame experiments. All that is necessary is that background pressure be varied while maintaining constant mass flows of fuel and oxidizer into the burner. A theoretical model for these flames indicates that this procedure isolates Richardson number (or relative buoyancy force) as the only variable parameter, which is equivalent to varying the gravitational acceleration. A joint series of experiments and computations involving a pressurized low speed methane/air diffusion flame has provided strong evidence to support the theory.

It is clear that much work needs to be done in order to clarify the important role that buoyancy plays in jet diffusion flame dynamics. The results presented here only open to door to future studies, which can now be performed with reasonable effort and cost-effectiveness. Future research is also needed in order to determine the limits of usefulness of the buoyancy-isolation procedure described here. Clearly use of this procedure to attain very small effective gravitational accelerations appears unreasonable, as chemical kinetics could certainly not be ignored at the low pressures required. Additionally, enhanced soot production at low g [Bahadori *et al.* (1990)] would not be simulated by this pressure variation technique. However, relaxation of the requirement that Lewis number be unity appears feasible since the Prandtl and Schmidt numbers can both be considered as independent of pressure. Finally, since the basic model described here is not dependent on a particular geometry, other types of diffusion flames in different burner configurations could also be considered as candidates for buoyancy-isolation experiments. Thus, the possibilities for future research efforts in the area of buoyancy effects in diffusion flames appear rather substantial.

ACKNOWLEDGEMENT

Two of the authors (RJS and JRN) wish to gratefully acknowledge the sponsorship of the Air Force Office of Scientific Research, Air Force Systems Command, USAF, under grant number AF 87-0145.

REFERENCES

Altenkirch, R. A., Eichhorn, R., Hsu, N. N., Brancic, A. B., and Cevallos, N. E. (1976). Characteristics of laminar gas jet diffusion flames under the influence of elevated gravity. *Sixteenth Symposium (International) on Combustion*. The Combustion Institute, p. 1165.

Bahadori, M. Y., Edelman, R. B., Stocker, D. P., and Olson, S. L. (1990). Ignition and behavior of laminar gas-jet diffusion flames in microgravity. *AIAA Jour.*, **28**, 236.

Buckmaster, J., and Peters, N. (1986). The infinite candle and its stability—a paradigm for flickering diffusion flames. *Twenty-First Symposium (International) on Combustion*. The Combustion Institute, p. 1829.

Chen, L.-D., Seaba, J. P., Roquemore, W. M., and Goss, L. P. (1988). Buoyant diffusion flames. *Twenty-Second Symposium (International) on Combustion*. The Combustion Institute, p. 677.

Davis, R. W. and Moore, E. F. (1985). A numerical study of vortex merging in mixing layers. *Phys. Fluids*, **28**, 1626.

Davis, R. W. and Moore, E. F. (1987). Numerical modeling of steady laminar diffusion flames. Paper No. 15 presented at the Twentieth Fall Technical Meeting of the Eastern Section of the Combustion Institute, National Bureau of Standards, Gaithersburg, MD, November 2–5, 1987.

Davis, R. W., Moore, E. F., Chen, L.-D., Roquemore, W. M., Vilimpoc, V., and Goss, L. P. Preliminary results of a numerical/experimental study of the dynamic structure of a buoyant jet diffusion flame. *Comb. and Flame*, to appear.

Eickhoff, H. and Winandy, A. (1985). Visualization of vortex formation in jet diffusion flames. *Comb. and Flame*, **60**, 99.

Flower, W. L. (1988). An investigation of soot formation in axisymmetric turbulent diffusion flames at elevated pressure. *Twenty-Second Symposium (International) on Combustion*. The Combustion Institute, p. 425.

Mitchell, R. E. (1980). A theoretical model of chemically reacting recirculating flows. Report No. SAND79-8236, Sandia National Laboratories, Livermore, CA.

Rehm, R. G. and Baum, H. R. (1978). The equations of motion for thermally driven, buoyant flows. *Jour. of Research of the Nat. Bur. Stds.*, **83**, 297.

Roquemore, W. M., Chen, L.-D., Goss, L. P., and Lynn, W. F. (1989). The structure of jet diffusion flames. In Borghi, R. and Murthy, S. N. B. (eds.), *Turbulent Reactive Flows, Lecture Notes in Engineering*, Springer-Verlag, Berlin, Vol. 40, p. 49.

Strawa, A. W. and Cantwell, B. J. Investigation of an excited jet diffusion flame at elevated pressure. Submitted to *J. Fluid. Mech.*

Subbarao, E. R. (1989). The effects of Reynolds number and Richardson number on the structure of a vertical co-flowing buoyant jet. AIAA Paper No. 89-1800.

Takahashi, F., Mizomoto, M., and Ikai, S. (1988). Structure of the stabilizing region of a laminar jet diffusion flame. *J. Heat Trans.*, **110**, 182.

Yule, A. J., Chigier, N. A., Ralph, S., Boulderstone, R., and Ventura, J. (1981). Combustion-transition interaction in a jet flame. *AIAA Jour.*, **19**, 752.